Universitat Autònoma de Barcelona

Development of bimodal waveguide interferometric sensors for environmental monitoring

Blanca Chocarro Ruiz

Universitat Autònoma
de Barcelona

Doctorat en Biotecnologia
Departament de Genètica i de Microbiologia - Facultat de Biociències

Development of bimodal waveguide interferometric sensors for environmental monitoring

Doctoral Thesis – 2019

Blanca Chocarro Ruiz
Author

Prof. Laura M. Lechuga
Prof. Daniel Maspoch
Directors

Prof. Antonio Villaverde
Tutor

CSIC
Consejo Superior de Investigaciones Científicas

ICN2
Institut Català de Nanociència i Nanotecnologia
Excelencia Severo Ochoa

A mi madre

Abstract

This Doctoral Thesis is devoted to the development of novel nanophotonic sensors as alternative solutions for the existing environmental monitoring tools currently employed. In particular, we propose the use of a novel interferometric sensor, the bimodal waveguide interferometer device (BiMW), for the selective, sensitive, rapid and direct analysis of pollutants present in the marine and the air environments.

For the detection of pollutants in different media, air and water, two strategies have been followed. The first approach was the development of a biosensor device based in a competitive immunoassay for the detection of traces of a pesticide directly in seawater. To achieve this objective, we started with an in-depth study of different biofunctionalization strategies because the surface chemistry needs to be optimized to maximize the stability, reproducibility and sensitivity of the competitive immunoassay. Another crucial step for the development of the pesticide biosensor was the optimization of the immunoassay conditions. Our final immunosensor overcomes some of the constraints of the current analytical techniques and offers an advanced analytical tool for the real-time and on-site monitoring of water pollution control.

The second strategy proposes the integration of Metal-Organic Frameworks (MOFs) as receptors to develop a chemical sensor for the detection of small molecules such as gases. First, the type of MOF and the integration in thin films were evaluated and optimized. Then, the developed MOF-BiMW gas sensor was assessed in terms of sensitivity, selectivity, reproducibility and stability. Results show that this new sensor overcomes some of the drawbacks of the current methodologies for gas sensing.

This work has opened the path of a new research line for the real implementation of advanced environmental monitoring sensing tools.

Resumen

La presente Tesis Doctoral está dedicada al desarrollo de novedosos sensores nanofotónicos como soluciones alternativas a las herramientas existentes de monitoreo medioambiental. En concreto, proponemos el uso de un novedoso sensor interferométrico, el dispositivo de guías de onda bimodales (BiMW), para el análisis selectivo, sensible, rápido y directo de contaminantes presentes en ambientes marinos y el aire.

Para la detección de contaminantes en diferentes medios, agua y aire, se han seguido dos estrategias. La primera fue el desarrollo de un dispositivo biosensor basado en un inmunoensayo competitivo para la detección de bajas concentraciones de un pesticida directamente en agua de mar. Para lograr este objetivo, empezamos con un estudio en profundidad de diferentes estrategias de biofuncionalización porque la química de superficie debe optimizarse para maximizar la estabilidad, reproducibilidad y sensibilidad del inmunoensayo competitivo. Otro aspecto crucial para el desarrollo del biosensor fue la optimización de las condiciones del inmunoensayo. Nuestro inmunosensor final supera alguna de las técnicas analíticas actuales y ofrece una herramienta analítica avanzada para el control en tiempo real e *in-situ* de la contaminación del agua.

La segunda estrategia propone la integración de redes metal-orgánicas porosas (MOFs) como receptores para desarrollar un sensor químico capaz de detectar pequeñas moléculas como los gases. Primero, se evaluó el tipo de MOF y se optimizó la integración en láminas delgadas. Luego, se evaluó el sensor MOF-BiMW de gases en términos de sensibilidad, selectividad, reproducibilidad y estabilidad. Los resultados demuestras que este nuevo sensor supera algunos de los inconvenientes de las metodologías actuales para la detección de gases.

Este trabajo ha abierto el camino para una nueva línea de investigación basada en la implementación de herramientas avanzadas para el control medioambiental

Agradecimientos

En primer lloc donar les gràcies a l'Institut Català de Nanociència i Nanotecnologia i la Universitat Autònoma de Barcelona per tenir l'oportunitat i un lloc idoni on fer la Tesi.

Quiero agradecer también a Laura Lechuga y Daniel Maspoch por la oportunidad de realizar el doctorado en sus grupos de investigación y su guía y ayuda durante estos años.

Dar también las gracias a todos los miembros de NanoB2A y NanoUp, a Jesuuús, Marta Ruiz, Patri, Jess, Miquel, Daniel, M. Carmen, Ceren, Jordi, Laura, Luis Carlos, Nuria, Berto, Santos, Joel, Rebe, María, Alejandro, Cris, Roger, Marta Sanmartí, Thais, Raquel, Rosa, Inhar, Mary, Sonia, Arnau, Vicent, Javier T, Jorge, Gerard y Marta Arenas. Muchas gracias en especial a Sonia por su incalculable ayuda y también a Javier Pérez y Adrián. Pero sobretodo agradecer a Clau su valiosa amistad y consejos que desde el principio me hicieron costado. En este tramo final ¡muchas gracias a Oli! Sin ellas no habría sido posible.

Thanks a lot to my UCLA labmates: Ani, Jérémie, Mustafa and Zach and also my flatties Helena, Johny, Jose and Greg.

Me siento muy afortunada por tener los amigos que tengo, gracias valentes: Helena, Clara, Carla, Paolita y Martas. A mis amigos desde mi más tierna infancia Aleix, Oli, Joan, Vero y Marta. Los muchos viajes y recuerdos con Enric y Marta, mis compis de inglés hace ya más de diez años. Gracias también a mis compis de equipo jotaemme. No quiero dejar de agradecer a mis amigas de la uni Valeria, Silvia y Núria por formar parte de mi vida. Un gracias infinito a Alba, Núria, Tere y Júlia por todos y cada uno de vuestros consejos y momentos.

Por último, esta tesis se la quiero dedicar a mi familia. A mi padre, mi yaya, mi madrina, a Jesús, Alfonsita, mis tíos y primos. Pero en especial a mi madre y mi primi! Os quiero mucho.

Table of contents

Abstract ..... *i*

Resumen ..... *iii*

Agradecimientos ..... *v*

1. Introduction *1*

1.1. Environmental pollution **1**

1.1.1. Origin and classification 1

1.1.1.1. Water pollution 2

1.1.1.2. Air pollution 3

1.1.1.3. Soil pollution 4

1.1.1.4. Others 4

1.1.2. Environmental impacts 4

1.2. Environmental monitoring **6**

1.2.1. Water pollution monitoring 6

1.2.1.1. Chromatographic methods 7

1.2.1.2. Immunoassays 8

1.2.2. Air pollution monitoring 10

1.3. Chemical sensors and biosensors **13**

1.3.1. Classification 15

1.3.1.1. Electrical and electrochemical sensors 15

1.3.1.2. Mechanical sensors 16

1.3.1.3. Optical sensors 17

1.3.2. Integrated optics sensors 19

1.3.2.1. Grating sensors 20

1.3.2.2. Microring resonator sensors 21

1.3.2.3. Photonic crystal sensors 24

1.3.2.4. Interferometric waveguide sensors 25

1.3.2.5. Comparison and future perspectives 28

2. Motivation and objectives *33*

3. Bimodal waveguide interferometer sensor *37*

3.1. Working principle **37**

3.2. Design and fabrication **40**

3.3. Experimental set-up **42**

3.3.1. Optical system 42

3.3.2. Fluid delivery system 43

3.4. Sensor chip 44
3.4.1. End-faced polishing 44
3.4.2. Sensor chip cleaning 45
3.4.3. Sensitivity evaluation 45

4. Analysis of Irgarol 1051 in seawater with a bimodal waveguide interferometer immunosensor 51

4.1. Introduction 51
4.1.1. The target analyte: Irgarol 1051 51
4.1.2. The biorecognition layer 54
4.1.3. Immunosensors 55
4.1.4. Immobilization of biorecognition elements 61

4.2. Materials and methods 65
4.2.1. Reagents and materials 65
4.2.2. Surface functionalization 66
4.2.3. Biosensor immunoassay 70

4.3. Comparison of the different evaluated sensor surfaces 70

4.4. Optimization of the sensor surface functionalization 73

4.5. Immunoassay optimization 76

4.6. Analytical performance of the BiMW immunosensor 78

4.7. Analyses of spiked seawater samples 81

4.8. Conclusions 83

5. Carbon dioxide detection combining metal-organic frameworks as receptors with a bimodal waveguide interferometer sensor 87

5.1. Introduction 87
5.1.1. The target analyte: carbon dioxide 87
5.1.2. Metal-Organic Frameworks (MOFs) 88
5.1.2.1. MOFs as sensors receptors 89
5.1.2.2. MOF films 92

5.2. Materials and methods 94
5.2.1. Reagents and materials 94
5.2.2. Synthesis of nanoZIF-8 (size = 32 ± 5 nm) 94
5.2.3. Synthesis of ZIF-8 (size = 53 ± 8 nm) 95
5.2.4. Synthesis of ZIF-8 (size = 70 ± 12 nm) 95
5.2.5. NanoZIF-8 film formation and optimization 96
5.2.6. PDMS film formation 96
5.2.7. Mixed matrix membrane of nanoZIF-8/PDMS film 96

5.2.8. Characterization 97
5.3. Fabrication and optical characterization of MOF films 97
5.4. Design of the experimental gas sensor set-up 101
5.5. Integration of the nanoZIF-8 films onto the transducer 103
5.6. Analytical performance of the MOF-BiMW gas sensor 107
5.7. Conclusions 116
General conclusions ***119***
Annex ***125***
List of publications ***131***
Abbreviations and acronyms ***133***
List of figures ***137***
List of tables ***145***
Bibliography ***147***

Chapter 1

Introduction

This chapter provides a general introduction about the environmental pollution and its impact. An overview about environmental monitoring is also described, mainly focusing in water and air quality control and the existing analytical tools for such analysis, pointing out their advantages and limitations. Finally, the chemical sensor and biosensor technologies, in general, and the description of silicon photonics based sensors, in particular, are described.

1. Introduction

1.1. Environmental pollution

The natural environment encompasses the physical surroundings, both biotic and abiotic, happening without man-made changes. The anthropogenic disturbances are caused because humans are the only species with advanced material-technological cultures that affect the natural environment.[1] Human activity directly or indirectly results in the introduction of contaminants in the natural environment. A contaminant or pollutant is an unwanted biological, chemical, physical or radiological substance, that once introduced in the natural environment, causes an adverse change.[2] This phenomena, called environmental pollution, has been a crucial concern and has been identified as the origin of the global climate change.[3] However, despite the profound concern at worldwide level and the strong investment in remediation actions, the slow, but steady degradation of water, soil and air quality continues.

1.1.1. Origin and classification

Environmental pollution happens from natural sources since ancient times, but it is, since the last century, that an unprecedented impact has occurred from man-made causes.[4] It is commonly misinterpreted the pollution solely from anthropogenic sources but natural cause of contamination also exists; for instance, from volcanoes and fires.[5] Contaminants can experiment many different routes once they are released in the natural environment (see Figure 1.1). An example can be a harmful particle suspended in the air that deposits in a river and ends up permanently adsorbed in a sediment.[6] When classifying the different types of environmental pollution, it is mainly based on one of these environments: water, air and soil.

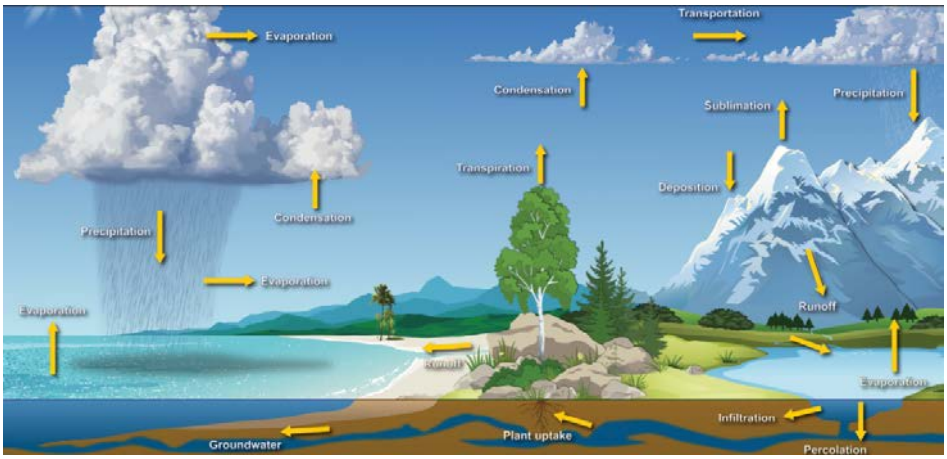

Figure 1.1. Scheme of different routes of pollutant transportation. (source: NOAA)

1.1.1.1. Water pollution

Water is one of the most important natural resources for human life and has a key role in crucial processes such as climate regulation. Pollution results when contaminants are introduced into water bodies such as oceans, rivers, lakes, aquifers or groundwater.[7] Every year large quantities of waste and pollutants are dumped in the water bodies, derived mainly from anthropogenic actions related to industrial, tourism and urban activities.[8] Those water pollutants include domestic wastes, food-processing wastes, volatile organic compounds (VOCs), heavy metals, pesticides and pollutants from livestock operations and chemical waste, among many others. The discharges of these contaminants together with the intensive exploitation of the water resources have caused the continuous degradation of the aquatic ecosystems both in terms of chemical composition and loss of biodiversity.[9]

Pathogens are another major group of pollutants as they cause waterborne diseases from contaminated water, largely related to wastewater from the domestic sector. Besides, water is a common source for the distribution of pollutants to humans and to the rest of the biota. Examples are nutrient pollution (e.g. nitrogen, phosphates, etc.) increasing the growth of toxic algae that affects other aquatic animals, and pesticides affecting the photosynthesis of plants.[10]

1.1.1.2. Air pollution

Air pollution is defined as the presence of substances in the atmosphere, resulting either from human activity or natural processes, present in sufficient concentration, for a sufficient time and under circumstances, such as to interfere with comfort, health and welfare of persons or the environment.[11] The most common contaminant gases emitted to the atmosphere include carbon dioxide, carbon monoxide, sulfur oxides, nitrogen oxides, ozone, methane and chlorofluorocarbons, among many others. Other well-known air pollutants are VOCs or particulate matter (PM, fine particles of solid or liquid suspended in a gas). Despite air pollution is primary associated with man-made activities, many of the major air pollutants are also emitted by nature. Some of the most important anthropogenic sources are (Figure 1.2): (1) industries of manufacturing sectors, oil refineries and fuel production; (2) land transport; (3) small combustion sources from residential and commercial energy use; (4) fossil fuel power stations; (5) biomass burning in agriculture and forest management; and (6) agriculture, especially ammonia emissions from fertilizers and animals.[12]

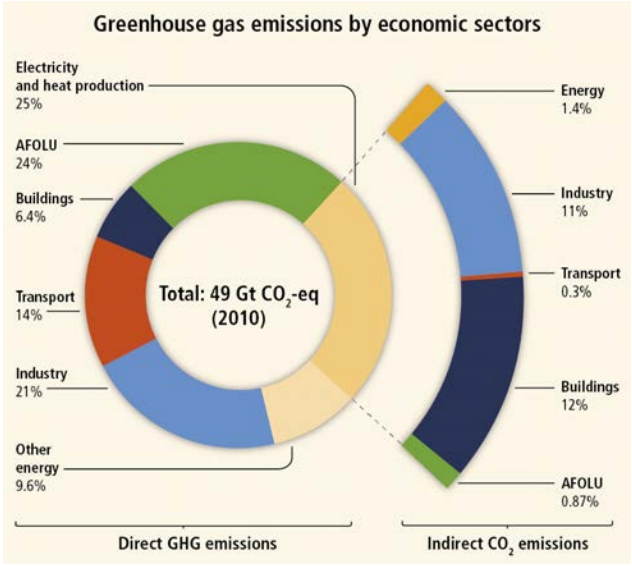

Figure 1.2. Total anthropogenic greenhouse gas (GHG) emissions (gigaton of CO_2 - equivalent per year, $GtCO_2$ - equivalents/year) from economic sectors in 2010.[13]

1.1.1.3. Soil pollution

Another common type of contamination is the land pollution. The soil can be directly contaminated; for instance, when using pesticides; or after the transport and deposition of pollutants coming from the air and the rain. The most significant pollutants include hydrocarbons, heavy metals, pesticides and solvents. Common sources of pollution are fossil fuels from industry and transport, or the domestic sector that produces municipal solid waste that directly ends in landfills or are incinerated. In humans, the effects are not only directly related to health problems but also to food production; altering plant metabolism, reducing crop yields or up the food chain when animals eat plants that have absorbed soil contaminants.[14]

1.1.1.4. Others

Despite air, water and land pollution are the major types of environmental contamination, there are other significant ones. The alarming increasing rate of noise pollution is currently a key issue. Sources of outdoor noise are transport, industry and neighbors and it can affect human health and animal welfare.[15] Finally, other important forms of contamination are radioactive and thermal pollution.

1.1.2. Environmental impacts

There are many impacts in the human health related to pollution (Figure 1.3). The presence of pollutants can have acute and chronic effects on humans depending on the toxicity, concentration and exposure time to the contaminant. The primary threat to death and disease globally is air pollution. Major health risks include lung cancer, acute respiratory infections in children, chronic respiratory and heart diseases and stroke.[16] In developing countries, a primary health risk is water pollution owing to the contamination of drinking water by untreated sewage, being diarrhea the most widely known disease.[17]

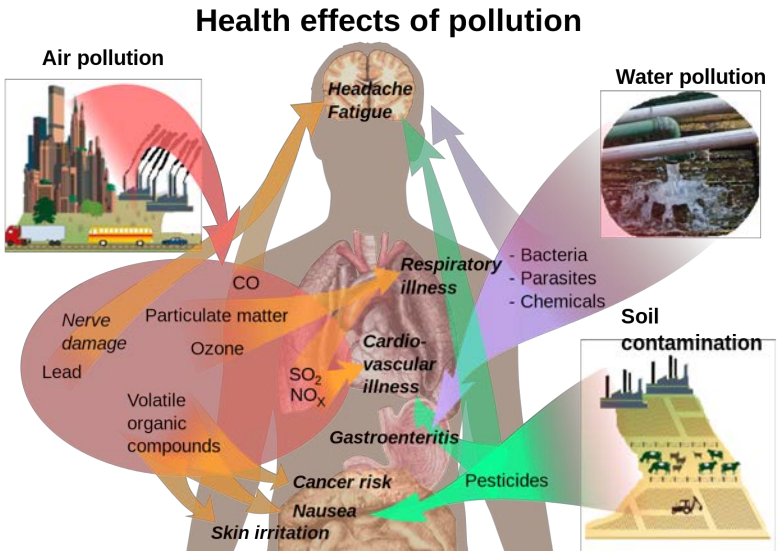

Figure 1.3. Overview of the main health effects on humans related to pollution. (Source: Häggström, Mikael (2014))

A major environmental impact is global warming caused by the emission of greenhouse gases. Water vapor, carbon dioxide, methane, nitrous oxide and ozone are the primary greenhouse gases. Their continuous emissions are causing significant modifications in the last decades that were unprecedented in the last few millennia. Some of these effects include increased temperatures in the atmosphere and oceans, more often and longer heat waves, extreme precipitation events, decrease in the snow and ice levels with the arctic ice decline and retreat of glaciers, acidification of the oceans and rise of the global seal level. Moreover, the biota is heavily affected by the extinction of species and the reduction of the ecosystem diversity.[13]

Another well know threat is the ozone depletion, caused by a steady lowering of the stratospheric ozone levels that prevents most harmful ultraviolet light (UV light) to reach the Earth surface.[18] However, ozone is considered a greenhouse gas when is present at abnormally high concentrations in the troposphere (the lowest layer on Earth's atmosphere). The tropospheric ozone is a major constituent in the formation of smog that affects human health and the photosynthesis of plants due to the sunlight reduction.[19]

Other major concerns are eutrophication, invasive species, acid rain caused by sulfur dioxide and nitrogen oxides, and biomagnification, among others.

1.2. Environmental monitoring

Environmental monitoring encompasses the processes and activities to evaluate the quality of the natural environment. The field of environmental monitoring has experienced a substantial progress in the last century, although the on-site control of contaminants is still an elusive problem. In addition, the growing number of pollutant sources is accompanied by an increasing need of having efficient early warning systems. Real-time and on-site monitoring of the pollution is vital to manage environmental degradation and to protect the natural environment quality for the future of the world. The conventional analytical techniques, based on chromatographic and spectroscopic technologies, remain the preferred analytical methods for environmental control due to its accuracy and sensitivity. However, these methods are limited to centralized laboratories, require expensive instrumentation, are time consuming and need trained personnel. To overcome the high costs and low speed of those analysis, chemical sensors and biosensors devices emerged as promising alternative tools several years ago.[20] They can provide the demanded portable analytical tools and early warning systems because they are fast, specific, sensitive, reusable and enable permanent and unattended operation in the field.[21] The available analytical instruments and methods for water and air pollution monitoring will be described in more detail.

1.2.1. Water pollution monitoring

Most of the harmful contaminants are present in extremely low concentrations and, therefore, their monitoring is a crucial step towards sustainability of the water quality and the use of the aquatic ecosystems.[22] Conventional analytical methodologies are very sensitive and selective tools to control the water quality but they only operate at laboratory settings, with the associate problems of samples transportation without degradation. Bringing the monitoring tools

directly to the contaminated resource can result in cost and time savings, allowing tracing water pollutants evolution in real time and dramatically reducing the response time in case of pollution peaks episodes.

1.2.1.1. Chromatographic methods

Chromatographic techniques are conventional analytical tools for the determination of most of the pollutants. These techniques usually require pre-treatment of the matrix sample to separate the target analyte from other components of the matrix according to their physical and chemical properties. Initially, this step was done using liquid-liquid extraction (LLE) but nowadays solid-phase extraction (SPE) has gained presence as the most common sample preparation process. In the SPE method, the analyte in the liquid sample (mobile phase) is separated passing through a solid (stationary phase), being the target analyte or the impurities the ones which are retained in the stationary phase. Solid-phase microextraction (SPME) is a more recent technique that involves the use of a fiber coated with an extracting phase that can be reused; this coating material can be solid (sorbent) or liquid (polymer). The main chromatographic techniques are:

- *Gas chromatography (GC):* is a common analytical tool for the detection of analytes that can vaporize without decomposition. The mobile phase is a carrier gas (usually the inert gas helium) and the stationary phase is a microscopic layer of liquid or polymer in an inert solid support inside a column of glass or metal. Each gas compound that is eluted has different retention times inside the column determining the separation of the analytes. Common selective detectors are the flame ionization detector (FID) and the thermal conductivity detector (TCD). However, one of the most effective and sensitive is the mass spectrometer (MS), called GC-MS or in tandem, GC-MS/MS.

- *Liquid chromatography (LC and HPLC):* in this technique, the stationary phase is a solid and the mobile phase is a liquid. High-performance liquid chromatography (HPLC) is one of the most

common analytical tools applicable to a wide range of pollutants (Figure 1.4). In this case, the mobile phase is a pressurized liquid solvent that is pumped inside the column. Common detectors are UV/Vis, photodiode array (PDA) or MS and MS/MS.

- *Thin-layer chromatography (TLC):* is a low-cost technique that allows the simultaneous evaluation of numerous samples but with low resolution. It is used to separate non-volatile mixtures.

Figure 1.4. Photo of a high-performance liquid chromatography. (Source: Controltecnica Instrumentación Científica, S.L.)

The chromatographic methods are the most widespread employed analytical techniques owing to their high sensitivity and selectivity. However, they have several drawbacks, since they are expensive, need of sophisticated equipment run by trained personnel and are time consuming due to the many steps involved (extraction, cleanup and preconcentration steps). Some of these disadvantages can be overcome with the use of immunoassays techniques.

1.2.1.2. Immunoassays

An immunoassay is a biochemical test based on antibodies (Ab) for the detection and quantification of a target antigen (Ag). In most of the cases, a detectable label conjugated or linked to the Ab or to an Ag analogue is needed to produce a measurable signal. The most

common immunochemical method uses enzymes as labels and are named enzyme-linked immunosorbent assays (ELISAs) or enzyme immunoassays (EIAs). Other types of assays, based on the label employed, are: radioimmunoassay (RIA) when using radioactive isotopes; chemiluminescence immunoassays (CLIA) when the label emits detectable light in response of an electronic current; and fluorescent immunoassay (FIA) or fluorescence polarization immunoassay (PFIA) based on fluorogenic labels.

Labeled Immunoassays can be homogeneous when the interaction of Ab-Ag takes place in the solution or heterogeneous when the interaction happens in the interface of a solid support and the sample matrix to separate the analyte from the solution. They can also be classified depending on the detection strategy (see Figure 1.5):

- *Competitive immunoassay:* in the *direct* format, the sample containing the antigens is first mixed with a fixed concentration of labeled antigens and then, they compete for the binding sites of the antibodies immobilized on a solid support. In the *indirect* format, the antigens are immobilized on the solid support, and the sample with the analytes is first mixed with a fixed concentration of the antibodies. In this case, the fixed Ag interact with the free unbound Ab that did not associate with the Ag in the sample. This first Ab can be directly labeled, or a secondary labeled Ab can be added to interact with the first unlabeled Ab. With both the direct and the indirect immunoassay, the obtained signal is inversely proportional to the analyte concentration in the sample.

- *Non-competitive immunoassay:* in this assay, also named sandwich immunoassay, the Ab is immobilized on the solid support and the sample containing the Ag is added, taking place the recognition between the Ab and the Ag. After, an excess of labeled Ab that interacts with a different epitope of the antigen is added to evaluate the amount of Ag/Ab pairs. In this case, the signal response is directly proportional to the Ag concentration. However, this immunoassay is limited to antigens with more than one binding site and, therefore, most of the small pollutants cannot

be evaluated with this technique, as they do not have more binding sites.

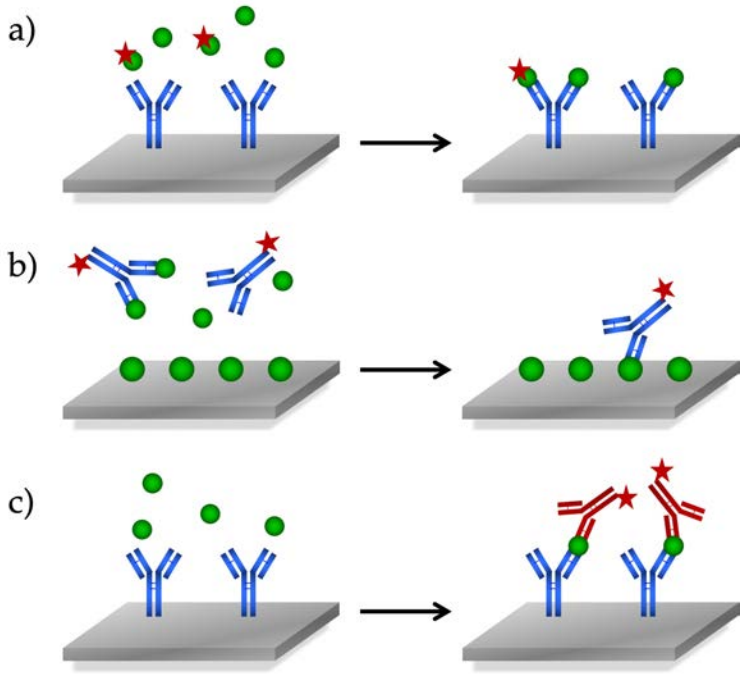

Figure 1.5. Main formats of labeled immunoassays: (a) competitive direct detection, (b) competitive indirect detection and (c) non-competitive detection.

The immunochemical techniques are low-cost and easy to use but, on the other hand, are time consuming due to the steps involved, are not reusable and can be affected by the pH and other interferent analytes present in the sample. An important step in these types of analyses is, therefore, the study of the cross-reactivity and the matrix effect.

1.2.2. Air pollution monitoring

The air quality monitoring implies great challenges owing to the inherent complexity of the atmosphere, the broad range of existing pollutants and the contaminant sources, both stationary (e.g. industries and disposal sites) and mobile. Historically, monitoring of

air pollution uses stationary, complex and expensive equipment, limiting the collection and analysis of data for an adequate planning and for implementing corrective actions.[23] Therefore, it not only requires close cooperation between government, industry and researchers for an effective integration of the multiple data sources but also analytical tools which are portable, robust, low-cost and highly reliable are very demanded.

The analytical instrumentation for air pollution monitoring employs a broad range of techniques based on spectroscopic and chromatographic methods depending on the target contaminant. These include chemiluminescent analyzers to measure NO_x, gas-liquid column chromatography with flame ionization detector for detecting volatile organic hydrocarbons, UV fluorescence spectrometer for SO_2 detection, or nondispersive infrared (IR) photometer for CO and UV photometer for O_3 detection, among others.[24] The commercially available gas sensors are (Figure 1.6):

- *Electrochemical or electrical sensors:* based on an electrochemical cell or a metal oxide semiconductor for the detection of NO_2, O_3, CO and VOCs, among others. The semiconductor metal oxide group is one of the most investigated electrical sensors because of their suitability as portable devices, affording enough sensitivity. They are low-cost and of short response time. However, their main drawback is their low selectivity. On the other hand, electrochemical gas sensors are more selective but they have less sensitivity, with longer response-time and lower durability.[25,26]

- *Optical sensors:* these sensors measure the absorption of light in the visible range for gases such as CO_2 or O_2, infrared wavelengths for CO_2 and employ chemiluminescence for NO_2 detection. A main group are the non-dispersive IR absorption sensors due to their sensitivity and selectivity, but their main disadvantages are the long response-time, and the high cost.[27]

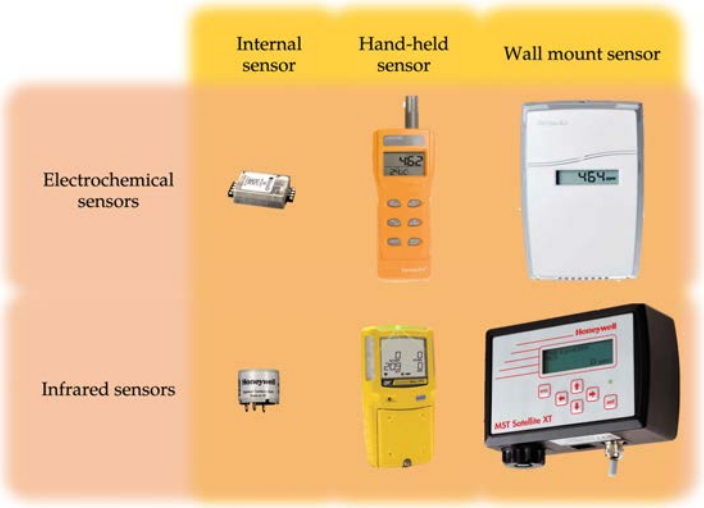

Figure 1.6. Photographs of different types of electrochemical gas sensors commercialized by Honeywell and infrared sensors commercialized by Senseair.

A growing research field during the last three decades are the electronic noses (e-noses). These instruments, inspired by the natural olfactory system, are based on an array of partially selective receptors to selectively and quantitatively detect VOCs.[28] The detection of these VOCs is based in different sensor technologies such as metal oxides, conducting polymers, quartz crystal microbalances (QCMs) and surface acoustic waves (SAW).[29] Depending on the sensor technology, they present some advantage and limitations. The main advantage of the metal oxide sensors are the high sensitivities, short response and fast recovery time.[30] However, they present some drawbacks such as poor selectivity and high power consumption.[31] On the other hand, the strengths of conducting polymers are the large variety of commercially available conducting polymers for a wide range of analytes, the capability to operate at room temperature and the short recovery times.[32,33] However, the main disadvantages include sensitivity to humidity and temperature changes, drift over time, costs, poor reproducibility between batches and limited lifetime.[34,35] In the case of QCM sensors, the main advantages are the selectivity, short response time and miniaturization capabilities.[30,35] Nevertheless, QCM sensor have low sensitivities and reproducibility, are expensive and are prone to drift.[31,34] Finally, SAW sensors have a

wide variety of sensitive coatings, high sensitivity and fast response time, but the main disadvantage is the low reproducibility.[30,34,35]

1.3. Chemical sensors and biosensors

A **chemical sensor** is a device that combines a molecular recognition element with a transducer, to convert a specific chemical interaction into a measurable signal. Materials used as recognition elements vary from metals and metal oxides, inorganic crystalline and amorphous materials and organic polymers to other composite materials. On the other hand, the International Union of Pure and Applied Chemistry (IUPAC) defines a **biosensor** as a device that uses specific biochemical reactions mediated by isolated enzymes, immunosystems, tissues, organelles or whole cells to detect chemical and biological compounds usually by electrical, mechanical or optical signals.[36] Although chemical sensors and biosensors are clearly differentiable according to their definition, some general considerations and the classification based on the transducer scheme can be defined for both of them (Figure 1.7).

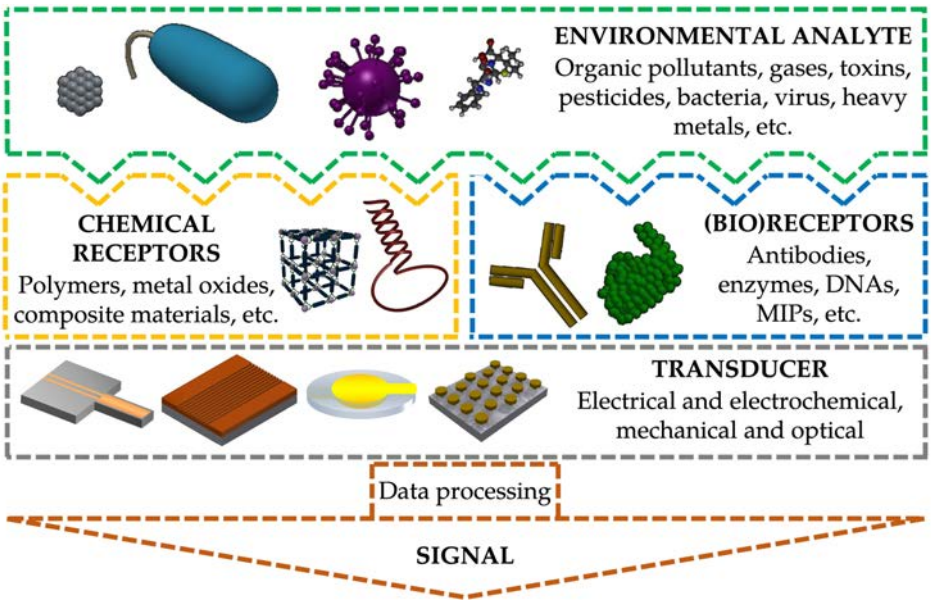

Figure 1.7. Schematic representation of a chemical sensor (left) and a biosensor (right). Chemical sensors and biosensors share the same transducer schemes but are clearly differentiable in the recognition element.

The chemical sensors and biosensors devices can detect a specific chemical compound in a quantitative or semi-quantitative manner because of the physicochemical changes detected by the transducer when the target analyte interacts with the receptor. As it is defined, the composition of a chemical sensor and biosensor contains two basic components in direct spatial contact: the receptor, providing the desired selectivity; and the transducer, able to process a signal from the interaction of the analyte with the recognition element. This integration in a single device avoids some of the drawbacks of conventional analytical techniques. Moreover, an ideal chemical (bio)sensor should possess the following characteristics:[37]

- *High sensitivity* to detect the minimum amount of the analyte molecule since many pollutants are detrimental when present at very low concentrations. The sensitivity is a fundamental parameter to define the performance of a sensor and is related to the magnitude of the transducer response caused by a change in the analyte concentration. The resolution, on the other hand, corresponds to the smallest variation that can be accurately detected and depends on the noise of the employed system (e.g. light or electrical source variations, thermal noise, read-out noise, etc.). The resolution is usually estimated as three times the standard deviation of the total system noise. The combination of the sensitivity and the resolution defines the **Limit of Detection (LOD),** which is the minimum amount of the analyte that can be accurately quantified.

- *High selectivity* of the receptor to be able to only detect the target analyte even when it is present in a complex matrix.

- *High reproducibility* and *accuracy* between sensor devices to detect the same concentration using different sensors and as identical as possible to the real value contained in the sample; and *high repeatability* to measure the same concentration during consecutive measurements employing the same sensor device and sample.

- *High stability* under different ambient conditions and storage.

- *Fast response time* for real-time analysis or even continuous monitoring, ideally using untreated samples.

- *Wide dynamic range* (DR) for the evaluation of analyte concentrations; thus, the sensor is capable to detect a broad range of concentrations of the target analyte.

- *Reusable* for consecutive measurements with the same sensor.

- *Low-cost* of the sensor fabrication technology in order to facilitate a mass production for potential commercial devices.

Other important characteristics include *miniaturization* for portable devices allowing on-site monitoring, *multiplexing* to simultaneously detect different analytes in the same sample with one sensor and *user-friendly* avoiding trained personnel.[21]

1.3.1. Classification

Chemical sensors and biosensors are broadly classified regarding the type of transducer. The main types are based on electrical and electrochemical, mechanical and optical principles.

1.3.1.1. Electrical and electrochemical sensors

Nowadays, electrochemical sensors are, together with the optical sensors, the most employed ones. They measure electrochemical changes such as current or voltage changes. Representative devices include *amperometric* sensors, which detect the change in the current at a constant or varying potential. Amperometric transducers are commonly used as biosensors, being the glucose sensor the first successful commercial biosensor, and still nowadays, the flagship in the commercial market.[38] *Potentiometric* sensors measure the potential or change accumulation of an indicator electrode (ion-selective electrode) against a reference electrode. They possess several advantages such as simplicity, wide dynamic range and low power consumption. Another major group are *impedimetric*

sensors, which quantify the change in the resistance, and the subgroup of *conductimetric* devices that evaluate the altered conductive properties of a medium between electrodes.[39–41]

Electrical devices are based on metal oxide semiconductors, organic semiconductor and electrolytic conductors. The first ones are mostly employed for gas detection based on the reversible redox processes of the analyte.[42,43] These semiconducting metal oxide gas sensors constitute one of the major research fields. These sensors can work under atmospheric conditions, are low-cost, user-friendly and can detect a large number of gases. A major drawback is the effect of the environmental humidity that can cause a decrease in the sensor sensitivity when the water molecules react with the oxide surface. Furthermore, a prolonged exposure of the sensor to humid environments progressively deteriorates the sensor surface, requiring very high temperatures for recovering. Another important factor is the temperature because an increase enhances the response but after a certain maximum, the sensor response drastically decreases when increasing the temperature.[44]

1.3.1.2. Mechanical sensors

The mechanical sensors have proven to be more versatile, in comparison to the electrochemical devices, since they can detect a wider range of analytes without the constraint of their dissociation or redox properties. The transducer evaluates the mass change when the analyte accumulates onto a chemically modified sensor surface. The main mechanical sensors include piezoelectric sensors, such as Quartz Crystal Microbalance (QCM), which measures the frequency changes of a quartz oscillator plate, and Surface Acoustic Waves (SAW) devices. Those type of devices have been applied both to liquid and gas samples, although SAW are more employed. QCM suffer from some drawbacks as the density and viscosity of the liquid samples drop the sensor signal and, therefore, the sensitivity. But in the case of gas sensors, specially QCM, have proven to be a competitive technology due to its multiplexing and miniaturization capability and temperature stability.[45,46]

1.3.1.3. Optical sensors

Optical transducers are based on the evaluation of the change in electromagnetic light properties such as intensity, phase, wavelength or polarization.[47,48] This evaluation results in a wide family of sensors based in different phenomena including transmission, absorption, reflection, luminescence, fluorescence, Raman spectroscopy and plasmon resonance, among others. The most employed optical sensors rely in the evanescent wave working principle.

The **evanescent wave sensors** measure refractive index (RI) changes. These sensors exploit the confinement of the electromagnetic waves in a dielectric and/or metal structure generating a propagating or localized electromagnetic mode. Part of the confined light propagates to the external medium generating the evanescent wave (EW) (Figure 1.8). RI changes in the external medium induce a local change in the optical properties of the excited electromagnetic mode *via* this EW; in particular, a change in the effective refractive index (N_{eff}) (a measure of the phase delay per unit length between vacuum and a guiding structure). When the surface of the guiding structure has immobilized a receptor layer, the exposure of the functionalized surface to the complementary analyte and the subsequent (bio)chemical interaction between them induces a local refractive index change. Its amplitude can be correlated to the concentration of the analyte and to the affinity constant of the interaction, yielding a quantitative value of the interaction.[49] Since the evanescent wave penetrates to the external medium up to hundreds of nanometers and decays exponentially, only changes occurring close to the sensor surface will be sensed and, therefore, background from the surrounding media will hardly affect.

The evanescent wave sensors offer significant advantages as they can operate under a label-free scheme, avoiding the complicated labelling procedures related for example to fluorescence sensors, making the overall detection process shorter and cost effective. Labels can also affect the interaction between the receptor and the analyte and their performance can be reduced when analyzing a complex

matrix. In addition, photonic sensors offer other advantages, as immunity to electromagnetic interferences, high sensitivity, wide bandwidth, and more importantly, the capacity of miniaturization and portability due to the scalable technologies employed for their fabrication.[49]

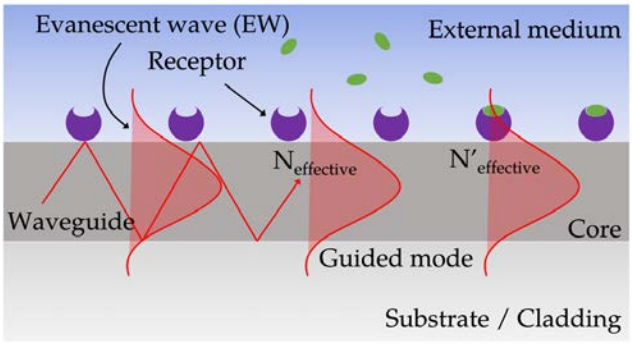

Figure 1.8. Scheme to illustrate the principle of the evanescent wave sensing.

The most well-known evanescent wave configuration is the Surface Plasmon Resonance (SPR) sensor based on the variation of the reflectivity on a metallic layer (generally a thin gold layer of 45 nm) in close contact with the external media.[50,51] The chemical functionalization of the metallic surface film *via* self-assembled monolayers (SAMs) allows the selective and sensitive detection of analytes with limits of detection in the pico-nanomolar range. The SPR sensor has been widely developed and commercialize and is one of the sensing techniques more widely reported in the literature. But the SPR sensor is difficult to miniaturize and to be converted in a portable tool and has a limited number of channels to perform simultaneous measurements.

In the nanoplasmonic field, the interaction of light waves with metal nanostructures (as gold nanostructures), smaller than the incident wavelength, generates a resonance phenomenon called Localized Surface Plasmon Resonance (LSPR). This phenomenon has been widely exploited for sensing during the last years. Although the LSPR sensors do not significantly increase the sensitivity as compared

to the SPR sensors, they are considered as the next generation of SPR sensing platforms. This is due because LSPR has a strong potential for integration and miniaturization, as well as, multiplexed capabilities.[52,53]

During the last years, the field of optical sensors has been fueled with more competitive and exceptionally highly sensitive nanophotonic transducers. These transducers are mainly based on compact waveguide structures contained on chips: the so-called integrated optics sensors or silicon photonics based sensors.

1.3.2. Integrated optics sensors

An optical *waveguide* is a structure typically made of a dielectric material that guides electromagnetic waves with minimal loss of energy by total internal reflection (TIR) through a high refractive index material (n_1), the core, and surrounded by lower refractive index materials (n_2 and n_3), the claddings (Figure 1.9). Light propagates in the form of guided modes, which are defined by the propagation velocity and the field distribution that depend on the waveguide structure (dimensions of the core, d, and the refractive index of the core and the claddings materials, n_1, n_2 and n_3) and the working wavelength (λ). Waveguides that support only one mode of propagation are called single-mode, while the ones supporting several ones are named multi-mode. Any refractive index change occurring in close contact to the sensor surface, when the core is exposed to the external medium, will modify the effective refractive index via the EW that characterizes each of the guided modes.

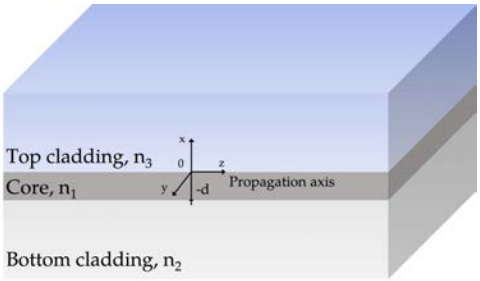

Figure 1.9. Scheme of an asymmetric slab waveguide configuration.

Depending on the light polarization which is travelling inside the waveguide, there are two types of modes: transverse electric (TE) and transverse magnetic (TM) modes (Figure 1.10). For TE modes, the electric field exhibits only a component perpendicular to the incidence plane (Ex, Ez = 0 and Ey ≠ 0), whereas in the case of TM polarization, the modes are characterized by an electric field vector parallel to the incident plane (Ex, Ez ≠ 0 and Ey = 0).

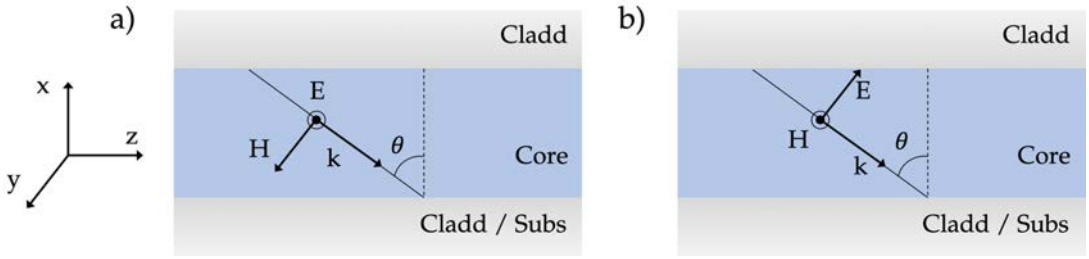

Figure 1.10. Propagation of polarized electromagnetic radiation: (a) TE and (b) TM polarizations.

The main detection schemes employed to configure a sensor device to monitor the effective refractive index change will be described in the following.

1.3.2.1. Grating sensors

A grating is a system of periodic or corrugated structures, which allows the excitation of a light guided mode in a waveguide. When a light beam with a specific angle of incidence is applied on a grating, the in-coupling condition is reached, and the light is propagated through the waveguide. The in-coupling angle is very sensitive to any perturbation in the surface of the waveguide due to the interaction through the evanescent field. Therefore, a grating structure can be employed as an evanescent wave sensor by monitoring the change occurring in the light in-coupling angle due to a change in the refractive index.

The company Microvacuum Ltd. (Hungary) commercializes sensor devices based on this technology, evaluating the in-coupling angle of a polarized laser light. The system is named optical waveguide light-mode spectroscopy system (OWLS) (see Figure 1.11).[54]

Figure 1.11. Photograph of the OWLS sensor device commercialized by Microvacuum Ltd.

Early work showed the performance of an OWLS immunosensor for the detection of the herbicide trifluralin, listed by the European Union as an endocrine disrupter. This biosensor improves the LOD (1 fg mL^{-1}) in six orders of magnitude as compared to the ELISA test.[55] Later investigations were focused on the sensing of mycotoxins,[56,57] showing similar or improved sensitivities than the standard ELISA test. Also, sensing of bacteria in water, using antibodies as biorecognition elements.[58,59] More recently, Maquieira *et al.* have developed an immunosensor for the detection of the pesticide atrazine with a LOD of 1.1 ng mL^{-1}.[60] In this work, the biomolecular receptors are patterned onto the solid surface forming a grating structure, called biograting.

1.3.2.2. Microring resonator sensors

In a microcavity resonator (RR), the light of a specific wavelength is coupled into a circular waveguide through the use of an external waveguide coupler (see Figure 1.12). The confined light in the microcavity is propagated in the form of whispering gallery

modes. Any perturbation on the waveguide microcavity surface taking places in the evanescent area induces a shift in the coupled light wavelength making this structure an excellent candidate for sensing applications.[61]

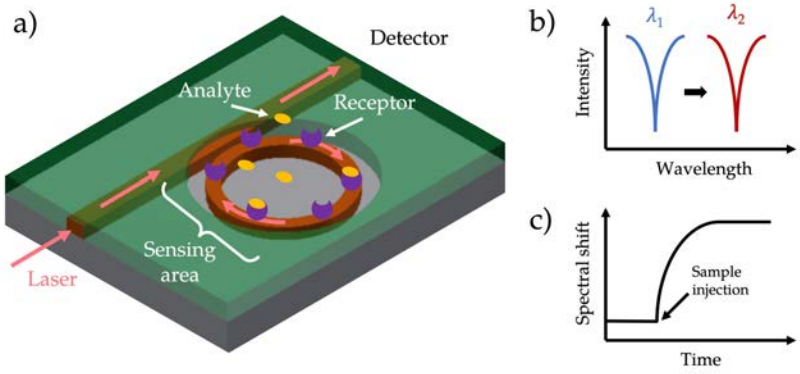

Figure 1.12. (a) Scheme of the working principle of a microring resonator sensor, (b) the resonant mode shifts in response to local RI changes induced by the binding event of the analytes with the receptors, and (c) signal obtained by monitoring the spectral shift in real time.

The quality factor (Q) of the microring, which is proportional to the number of times that the light circulates within the microcavity, influences notably the sensor sensitivity and, therefore, high Q factors are the preferred ones.[62] This has been confirmed by the single molecule detection of influenza A virions in air[63] or single nucleic acid interactions[64] employing high Q-factors microring biosensors. Moreover, these sensors are fabricated with standard microelectronics technology and can be miniaturized even in a high multiplexed array format for multiple analysis.[49]

Most of the RR sensors developed for sensing in liquid media are using biological receptors and have been applied for heavy metals,[65,66] pesticides,[67,68] bacteria[69] and virus[70,71] detection, among others. Genalyte (US) is a company commercializing this type of technology, with a multiplexed detection product, named Maverick®,

able to process an assay in 15 min and with a capacity up to 32 parallel sensors.[72]

Using this RR technology, Bog *et al.* developed a functionalization approach using a polymer (polydimethylsiloxane, PDMS) stamp patterned by polymer pen lithography.[67] The microring transducer was functionalized with 2,4-dinitrophenol, a hazardous pollutant used as pesticide. This novel functionalization approach allows multiplexing analysis, showing how to individually functionalize each sensor cavity on a densely packed chip. Another RR biosensor for pesticide detection was developed by Yang *et al.* for the detection of the organophosphorus pesticide parathion-methyl. This sensor exhibited an enhanced analysis times compared to standard techniques, achieving a LOD (10 pg mL^{-1}) in line with the admissible levels.[68]

Chemical RR sensors have been widely developed for gas and vapors detection. Some examples include a porous ZnO coating for ethanol vapor detection, estimating a theoretical LOD of 25 ppm.[73] But more ubiquitous are polymers and sol-gels as the sensing layer. A microring resonator was fabricated with an organic–inorganic hybrid sol–gel material as the receptor layer for ethanol vapor detection, measuring down to 31 ppm.[74] Other examples include a sol-gel polymer for moisture monitoring, but only measures down to 30 % relative humidity (RH).[75] In all these examples, however, the selectivity was not evaluated. Another research evaluated different polymers for the potential development of a multiplexed vapor sensor.[76] The selected polymers were the moderately polar methyl phenol polysiloxane or the highly polar polyethylene glycol (PEG) 400. The evaluated vapors were ethanol and hexane to represent polar and nonpolar analytes, respectively. Methyl phenol polysiloxane showed similar sensitivity to both vapors, but when the microring resonator sensor was coated with the polar PEG-400, the sensor achieved a LOD of 200 ppm for ethanol vapor. All these results demonstrate the great potential that the RR sensors offers for the detection of a wide range of hazards and its suitability using different receptors.

1.3.2.3. Photonic crystal sensors

A photonic crystal (PhC) is a structure composed by different refractive index materials disposed as periodic nanostructures. This periodicity affects the propagation of electromagnetic waves and generates a photonic bandgap, i.e. range of wavelengths that are not propagated. If a defect is introduced in the nanostructure, the photonic bandgap is disturbed, and then the PhC can be employed as a sensor.

PhC chemical sensors have been applied for a wide range of applications in environmental monitoring including detection of heavy metals in water or gases and vapors.[77,78] An early work showed a humidity sensor using polyacrylamide hydrogel as the sensitive layer into colloidal crystal structures measuring a RH only down to 20 %.[79] Jiang *et al.* reports a PhC sensor using tetraphenylethene polymer as receptor to selectively detect tetrahydrofuran (THF) or acetone vapors.[80] The sensor can be regenerated with air for at least 10 cycles and is evaluated with a concentration of THF down to 400 ppm or 600 ppm of acetone vapor. To potentially overcome the lack of selectivity for single gas sensing, Ozin *et al.* developed a novel class of photonic nose (see Figure 1.13).[81] This platform, as explained before, is an array-based sensing technology that utilizes different sensors with partial selectivity. It was based on the use of functional 1D photonic crystals comprised of multilayers of alternating refractive index, also known as Bragg stacks, and generating an array of nine 3 mm × 3 mm squares. The combinatorial arrays of surface-modified nanoparticle metal oxide porous Bragg stacks were evaluated, as a proof-of-concept, using water-saturated nitrogen gas.

Recently PhCs have emerged as a promising label-free class of biosensors.[82] While still at an early stage, some articles already reported the potential of these nanophotonic sensors for environmental monitoring. One of the first works reported a PhC biosensor for the detection of the organophosphorus pesticide parathion in water. The bioreceptor was the enzyme acetylcholinesterase and the biosensor was able to detect femtomolar concentrations of the pesticide.[83]

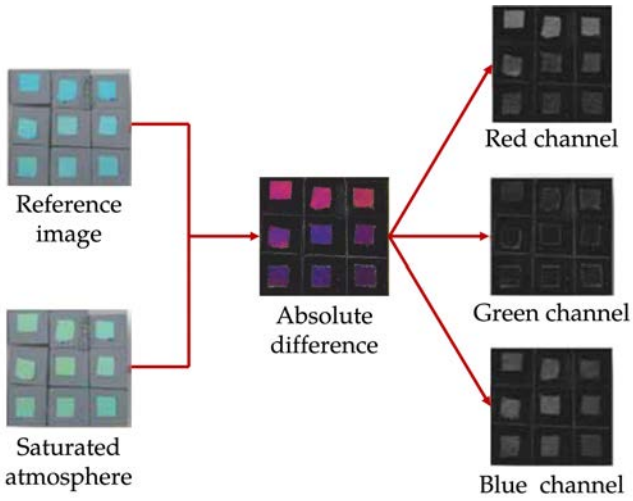

Figure 1.13. Schematic illustration of the basic steps in the color imagery analysis to monitor color changes in the PhC Bragg stacks array.[81]

1.3.2.4. Interferometric waveguide sensors

The working principle of an interferometric sensor relies in the creation of an interference pattern, generated by the superposition of two or more light waves in a waveguide.[84] In a common interferometric device, the incoming light beam is split, after a Y-junction, in two beams of equal intensity that travel through different optical paths (arms) defined in the waveguides. For sensing applications, one of the arms is used as a reference while the other acts as a sensing one. The most common interferometric waveguide sensors are the *Mach–Zehnder Interferometer* (MZI) and the *Young Interferometer* (YI). In a MZI, the two waveguide arms are recombined through a second Y-junction before arriving at a detector, which collects the interferometric signal (see Figure 1.14). In a YI, reference and sensing arms are not recombined before the output. They are out-coupled individually and the exiting light from both arms is projected into a screen generating the interference pattern off-chip. In those configurations, the MZI and the YI, the arms are single-mode waveguides to avoid complex signals from different evanescent field interactions with the external medium. The sensing arm has a portion of the core waveguide exposed to the external medium named the

sensor area. A bulk refractive index change or a molecular interaction in the sensor area causes a variation of the effective refractive index of the light traveling inside the waveguide, which is detected by the evanescent field. This induce a phase difference when both light waves interfere. This phase variation is proportional to the interaction length of the evanescent field with the sample and, therefore, longer paths in the sensor area increase the sensitivity. The resulting interference output is a sinusoidal signal with a visibility factor (amplitude) and number of fringes proportional to the concentration of the analyte inducing the phase change.

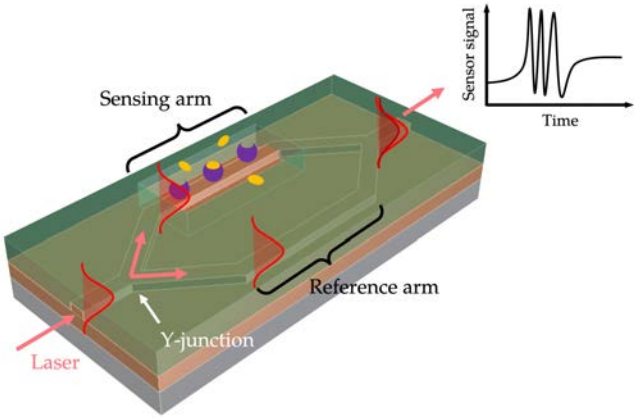

Figure 1.14. Scheme of an interferometer based on a Mach-Zehnder configuration and its interferometric output.

Due to the periodicity of the output signal, the interferometric transducers present the drawbacks of phase ambiguity, sensitivity fading and misinterpretation of the signal. The reference arm, on the other hand, can compensate refractive index changes caused by fluctuations, for example, temperature variations. Interferometric devices are generally fabricated using standard microelectronics technology which allows the fabrication of compact sensors arrays in a miniaturized format.[49]

Some examples of MZI chemical sensors for environmental monitoring include the detection of heavy metals using poly(vinyl

alcohol) hydrogel as the sensing layer.[85] An early example was a vapor sensor using a polysiloxane as the receptor layer for the detection of tetrachloroethylene vapor with a LOD of 100 ppm.[86] Lee *et al.* developed a gas sensor with a palladium coating as the sensing layer for the evaluation of 4 % of hydrogen.[87] Later, a MZI sensor using graphene as the sensing layer was developed for ammonia detection down to 40 ppm.[88] More recently, Zhu and co-workers developed an ammonia gas sensor using poly(acrylic acid), poly(allyamine hydrochloride) and single-walled carbon nanotubes, evaluating down to 1 ppm ammonia gas.[89] In all those examples, however, the selectivity was not evaluated.

In the biosensor field, the MZI is the most common interferometric configuration and it has been widely applied for the analysis of pollutants of environmental relevance. Early work showed an immunosensor for the detection of the pesticide simazine but, although the LOD is 0.1 ppb, it was still not suitable for the analysis of drinking water.[90] In parallel, another study developed an immunosensor for the detection of atrazine at concentrations around the EU limit at that time (100 ng L^{-1}).[91] Recent studies report MZI immunosensors for the detection of bacteria[92] and mycotoxins.[93] For the detection of the mycotoxin aflatoxin M1, the company LioniX International (Netherlands)[94] has developed a proof-of-concept device using an asymmetric MZI (aMZI) inmunosensor.[95] With this aMZI, we have recently developed an immunosensor for the detection of the biocide Irgarol 1051 and the antibiotic Tetracycline showing LODs in the range of few ng mL^{-1} (Figure 1.15). This immunosensor platform is fully integrated to be allocated in stand-alone buoys for the on-site analysis of harmful organic ocean pollutants. Finally, another company, Optiqua Technologies (Netherlands),[96] has developed a MZI, the MiniLab™ system, for water quality monitoring.[97]

A few years ago our Group also introduced a new interferometric version, with a common path waveguide, called Bimodal Waveguide Interferometer (BiMW).[98] In this device, the two beams that propagate in the separate arms of the MZI are substituted by a single waveguide with two light modes of different order

propagating along a straight waveguide. This novel device overcome the need of Y-junction fabrication and renders in a more compact device with a smaller footprint and the possibility to fabricate more devices in the same wafer area.[49]

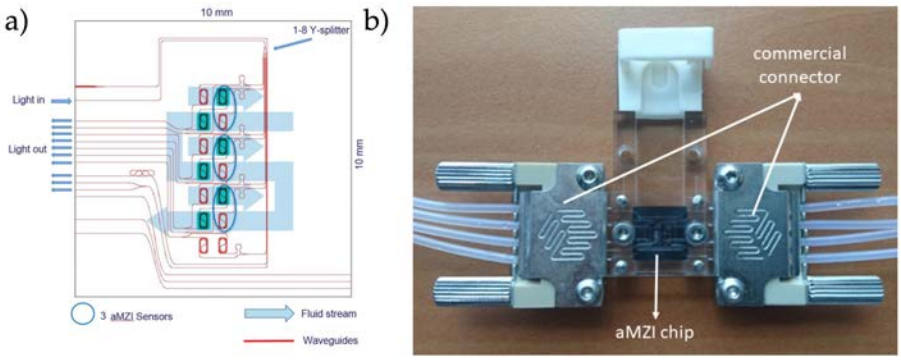

Figure 1.15. (a) Overview of the aMZI sensor chip layout and flow paths over the different sensors, designed by LioniX International. The three Mach-Zehnders sensors are encircled. (b) Photo of the aMZI chip assembled into a 4-channel microfluidic cell.

1.3.2.5. Comparison and future perspectives

Nanophotonic sensors based on evanescent wave detection can offer label-free, real-time, sensitive, selective, multiplex, rapid, and inexpensive analyses. All the technologies discussed above have advantages and disadvantages, and depending on the specific application, one can be more suitable than another. The main differences between all of them rely in terms of sensitivity and their ability for integration in compact portable platforms. Sensitivity for label-free detection in real samples is a must and therefore, the most suitable sensors, which have shown the highest levels of sensitivity, are the interferometric transducers. On the other hand, grating couplers and microcavity sensors exhibit an intermediate level of sensitivity and the photonic crystal sensors have shown a limited sensitivity for a direct and one-step label-free detection. Table 1.1 include a detailed comparison of the sensitivities of the different sensor technologies based on evanescent wave sensing.

Table 1.1. Comparison of the limit of detection of the different EW-based sensors.

Device configuration	Refractive index detection limit (RIU)	Mass detection limit (pg mm^{-2})
SPR	$10^{-5} – 10^{-7}$	1 – 5
LSPR	$10^{-5} – 10^{-7}$	0.5 – 5
Grating couplers	10^{-6}	0.3 – 5
Microring resonators	$10^{-5} – 10^{-7}$	0.3 – 3
Photonic crystals	10^{-4} - 10^{-5}	0.5 – 7.5
Interferometers	$10^{-7} – 10^{-8}$	0.02 – 1

Another important factor to select the most appropriate technology is the fabrication process. For grating couplers sensors is usually less complex and cheaper, while the fabrication of interferometric, microcavity and photonic crystal sensors is more complex, requiring many steps. A major drawback of the microring resonators is the difficulty for the coupling of light and the readout systems. However, they have, together with the interferometric systems, the additional advantage of providing microchip arrays with multiplex sensors of identical performances. Although photonic crystals based sensors are the most limited in terms of sensitivity, during the last few years, they have shown its capabilities for multiplexing and miniaturization in compact platforms as laboratory proof-of-concept prototypes. Due to the fast growing of mobile technologies as tablets and smartphones, potentially in the future a nanophotonic sensor can be integrated within these gadgets. Thus, such tools for portable analysis and early warning systems in environmental monitoring could be distributed around the world, helping to control the serious problem of the environmental pollution.

Chapter 2

Motivation and objectives

2. Motivation and objectives

The field of environmental monitoring has experienced a substantial progress in the last years but still the on-site control of contaminants is an elusive problem. In addition, the growing number of pollutant sources is accompanied by an increasing need of having innovative monitoring tools and efficient early warning systems. Real-time and on-site monitoring of the pollution is vital to manage environmental degradation and protect their quality for the future of our world.

Several years ago, biosensors devices emerged as promising environmental monitoring tools, but their level of miniaturization and their fully operation outside the laboratory prevented their use on-site. In the last period, nanophotonic sensors based on evanescent wave sensing have materialized as an outstanding choice for portable devices thanks to their capability, among others, of miniaturization, multiplexing, label-free detection and integration in lab-on-a-chip platforms.

The BiMW interferometer employed in this Thesis is a novel nanophotonic sensor device that has already been successfully applied as a biosensor for biomedical applications.[99] However, BiMW sensors have not been applied yet for environmental monitoring. Moreover, in this Thesis, it is postulated that the high sensitivity of these sensors suggests that, besides their archetypical use for biosensing applications, BiMW transducers show potential to be adapted as a chemical sensor for detecting small molecules such as gases.

The main goal of this Thesis is the development of novel interferometric chemical sensors and biosensors in views of improving current analytical techniques in the field of environmental monitoring. To achieve this goal, and as a proof-of-concept, two target analytes were selected: the pesticide Irgarol 1051 and the gas CO_2. The first analyte is commonly found in the marine environment; thus, the performance of the BiMW sensor operating in a complex matrix such as seawater and using antibodies as the receptors can be evaluated. In

the second part of the Thesis, the BiMW transducer was planned to be used, for the first time, for the evaluation of gases instead of fluid media. In this new scenario, the applicability of the BiMW sensor wanted to be extended by developing a chemical sensor integrating, for the first time, metal-organic frameworks (MOFs) as receptors. For this, different partial objectives were designed:

1. Development of an interferometric biosensor for the evaluation of a pesticide in the marine environment

    - Assessment and optimization of biofunctionalization strategies to immobilize the (bio)receptor in the transducer surface to enhance the analytical performance in terms of sensitivity, selectivity, stability and reproducibility.

    - Analytical characterization and optimization of the biosensor.

    - Application of the biosensor for the analysis of seawater samples to validate the accuracy and reliability of the proposed biosensor.

2. Development of a novel chemical sensor device combining nanoscale MOFs as receptors with the interferometric transducer for gas pollution control.

    - Selection, synthesis and structural characterization of MOFs.

    - Design of an experimental gas sensor set-up.

    - Analytical characterization and optimization of the MOFs-sensor device.

Chapter 3

Bimodal waveguide interferometer sensor

The first part of this chapter describes in detail the working principle of the BiMW transducer, followed by the device design and fabrication. Then, the experimental set-up is detailed, and finally, the methodology employed for the sensor chip preparation and bulk sensitivity evaluation are explained.

3. Bimodal waveguide interferometer sensor

3.1. Working principle

The transducer employed in this Thesis is the Bimodal Waveguide Interferometer commented in the Introduction. In this transducer (see Figure 3.1 for details), the interference pattern at the output is generated by the superposition of only two light modes traveling in the same waveguide, rendering in a more compact and miniaturized device.[98] The sensor is designed in such a way that a single mode is generated after the light is coupled in a straight rib waveguide. After passing through a step-junction, two transversal modes (fundamental and first order, respectively) with the same polarization, are excited. The BiMW sensor can work with the TE and the TM modes. However, although TE is less sensitive, this one is the chosen mode avoiding the noise caused by back-reflections. On the top cladding of the bimodal waveguide is defined an open sensing window in order to have access to the waveguide core surface. Since the fundamental and the first order modes have different evanescent field profiles, any change occurring in the refractive index over the sensing area differently affect the effective refractive index (N) of the fundamental (TE_{00}) and the first order (TE_{10}) modes, producing a phase change ($\Delta\phi$) (eq. 1):

$$\Delta\Phi = \frac{2\pi}{\lambda} L_{SA}(\Delta N_{TE10} - \Delta N_{TE00}) \qquad (1)$$

where L_{SA} is the length of the sensing area, and λ is the working wavelength. The first order mode has a longer penetration depth of the evanescent field and is the main responsible for sensing the surface refractive index changes, while the fundamental mode can be considered as a virtual reference. The phase variation ($\Delta\phi$) of the interference pattern caused by this shift generates a modification of the light output intensity distribution, which can be captured by a two-section photodetector with an upper and lower section, to generate I_{up} and I_{down} currents, respectively. The quantification of the sensor response can be evaluated by the change on this distribution,

calculated by the normalized signal (S_R), according to the expression of eq. 2:

$$S_R = \frac{I_{up}-I_{down}}{I_{up}+I_{down}} \alpha V \cos\left[\Delta\Phi(t)\right] \qquad (2)$$

where V is the signal visibility (amplitude) of the S_R when completing a whole cycle and defined as (eq. 3):

$$V = \frac{S_{R,max}-S_{R,min}}{2} \qquad (3)$$

Each measurement of the sensor signal response (%) is represented in π rad phase variation, corresponding to a half oscillation or fringe of the interferometric sensor.

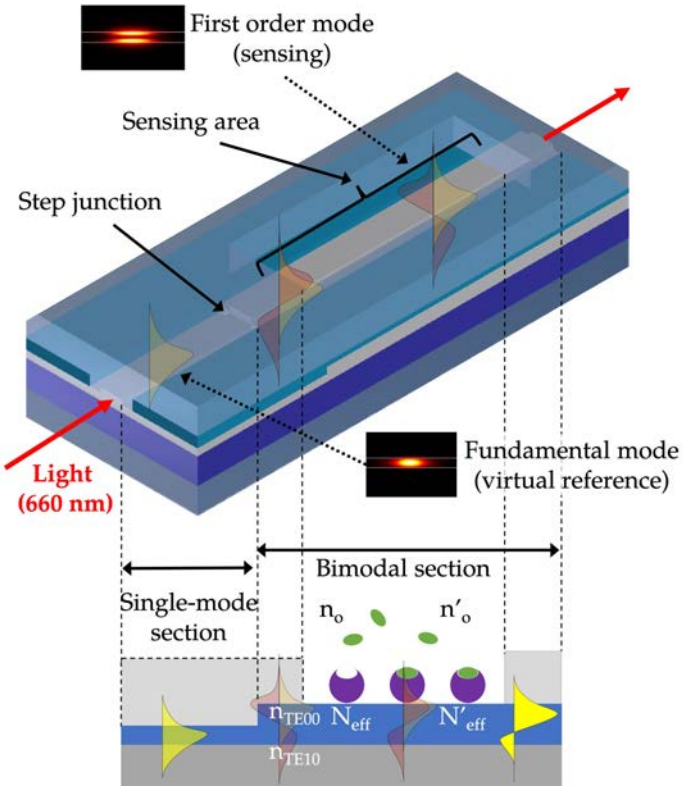

Figure 3.1. Scheme of the sensing principle of a BiMW sensor. Light is coupled in the single mode waveguide and after a modal splitter, two modes are excited, propagating until the sensor output.

Figure 3.2 is a typical sensor signal of the BiMW interferometer. It shows a bulk variation in the refractive index of the external medium in contact with the sensing area. The signal starts with a constant level, corresponding to water, and varies when another liquid (HCl in this example) reaches the sensing area (HCl ON). Then, the signal stabilizes when only HCl is in contact with the sensing area, changing again when the refractive index varies from HCl to water (HCl OFF), recovering the initial value of the base line. The phase shift induced by the refractive index variation in the sensing area is determined by counting the number of half oscillations or fringes and represented in π rad phase variation.

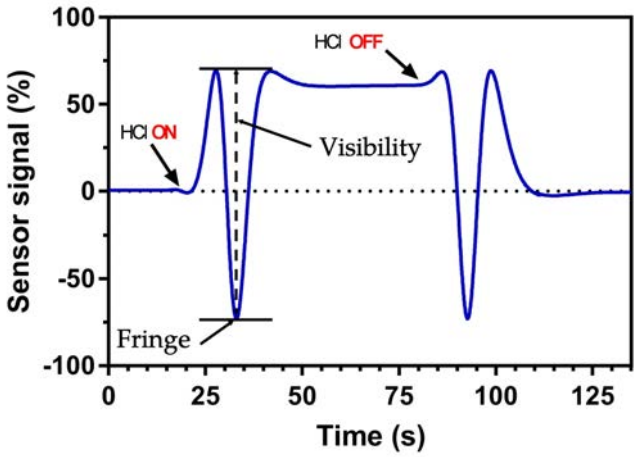

Figure 3.2. Example of the evaluation with a BiMW interferometric sensor of a change in the bulk refractive index. The S_R corresponds to the detection of a refractive index change $\Delta n = 7{,}2 \cdot 10^{-4}$ RIU.

Since the interference signal (S_R) is normalized to the total intensity propagating across the device, the phase variation is independent of the input light intensity variations and the output signal is not sensitive to fluctuations in the coupling efficiency. In this way, some of the misinterpretations of the signal that affect other interferometric configurations, as the MZI sensors, are solved. On the other hand, the sensor has been designed to work in the visible range avoiding water interferences from the IR absorption.

3.2. Design and fabrication

The BiMW interferometer sensors were previously designed in our group and are fabricated at the ICTS Clean Room facilities of the Microelectronic National Center (IMB-CNM-CSIC) in Barcelona. The fabrication process is based in a standard microelectronic technology including photolithography and etching processes over a silicon wafer substrate.

The chosen material of the waveguide core is silicon nitride (Si_3N_4) because of its high refractive index (n_{core}=2.00), high density and chemical inertness to ion species, oxygen or moisture permeation.[100] The core is confined by an upper and lower cladding made of silicon oxide (SiO_2) with a smaller refractive index of n_{cladd}=1.46 to ensure guiding the light through the core with minimal loss of energy. In a section of the bi-mode rib waveguide, the cladding is etched to generate the sensing area (L_{SA} = 15 mm) were the core is exposed to the external medium. Since the BiMW sensor operates with TE polarized light of a λ = 660 nm coupled into the rib waveguide by end-fire coupling method, both materials are ideal owing to their transparency for a broad spectral range (~ 200 – 2000 nm). Also, the majority of biomolecules are non-absorbent in the visible, avoiding any damage or light absorption making Si_3N_4 one of the best candidates for integrated optics waveguides-based sensors in the visible spectra.

The fabrication process starts thermally growing 2 μm thick layer of silicon dioxide onto a p-doped silicon wafer. After, a 0.34 μm thick core layer of silicon nitride is deposited by low pressure chemical vapor deposition (LPCVD). A segment of this layer is then reduced down to 0.15 μm with hot phosphoric acid by a wet etching process to generate the single mode section of the rib waveguide. Then, the rib structure is defined by buffer hydrofluoric acid (BHF) etching until reaching the final dimensions of 3 μm width and 1.5 nm height. A 100 nm thick layer of poly-crystalline silicon is employed as an absorbing material to eliminate light scattering and deposited over

200 nm of thermally grown silicon dioxide. The waveguides are then opened by etching of the poly-silicon. Later, a 1.5 µm of a top cladding layer of silicon oxide is deposited via plasma enhanced chemical vapor deposition (PECVD) and the sensor area (15 mm x 50 µm) is opened by etching the silicon oxide layer. Finally, and to protect the chips during the dicing process, the wafer is covered with a photoresist. A schematic representation of the BiMW fabrication process is shown in Figure 3.3.

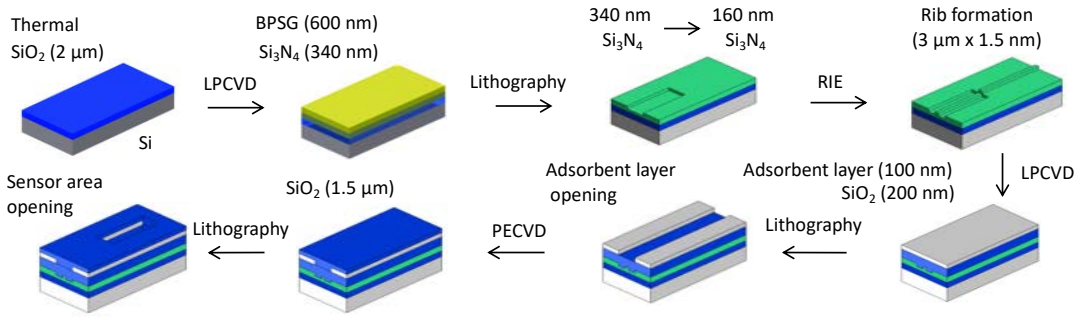

Figure 3.3. Scheme of the different steps for the fabrication of the BiMW sensors at Clean Room facilities.

The resulting wafer has a total of 12 BiMW chips, each of them containing 20 BiMW sensors, 6 BiMW references (without sensor area) and 6 single-mode waveguides, all of them separated by 250 µm from center-to-center (Figure 3.4). This wafer-level fabrication not only increase the precision and reproducibility of the fabrication process, but also reduces time and costs. The final dimensions for each chip are 3 cm x 1 cm and the dimensions for the rib waveguide are 3 µm width by 1.5 nm height. The first section of the waveguide has a thickness of 150 nm to only confine the fundamental mode. After the step junction, the thickness abruptly increases to 340 nm to split the confined light into the fundamental and the first order modes. The simplicity of the BiMW design, based on a common path waveguide, makes the BiMW sensor attractive for mass production since there is no need to use light splitters, such as the Y-type dividers or more

complex structures difficult to manufacture, as in the case of the conventional MZI or YI.[49]

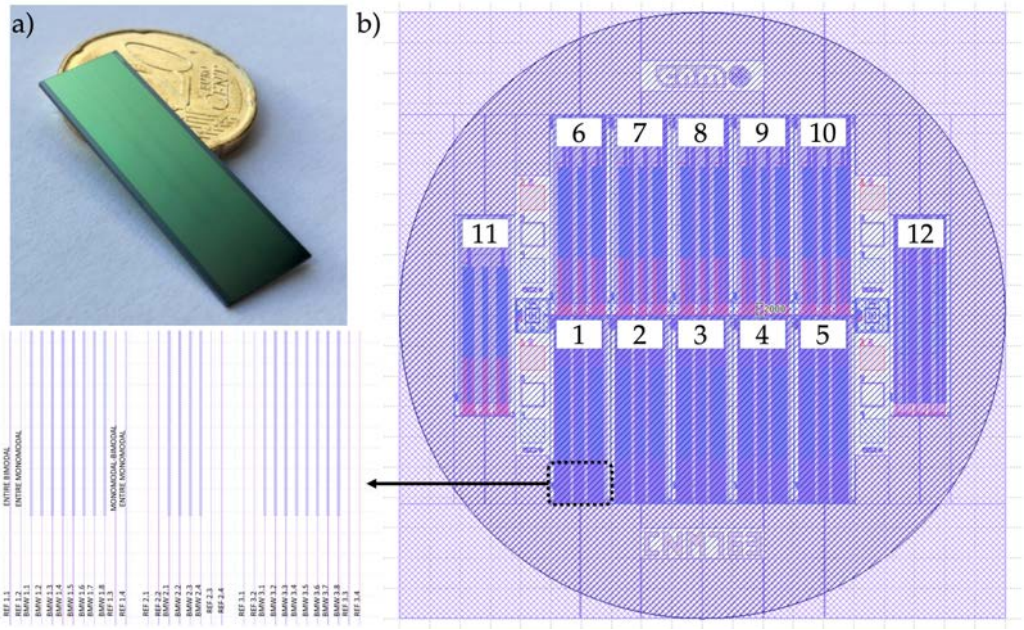

Figure 3.4. (a) Photograph of the BiMW chip containing 20 sensors. (b) BiMW wafer mask layout with 12 chips containing 240 sensors in total.

3.3. Experimental set-up

For the evaluation of the BiMW sensor, a dedicated experimental set-up needs to be assembled. A photograph of the BiMW sensor set-up is shown in Figure 3.5.

3.3.1. Optical system

As light source, we selected a TE polarized light of a λ = 660 nm and P=120 mW diode laser (ML101J27, Mitsubishi). The light is coupled into the BiMW sensor, by end-fire coupling method, using a lenses system composed by a collimated lens (C240TME-D, Thorlabs), a polarization-dependent isolator (IO-3D-660-VLP, Thorlabs) and a coupling objective 40x (Achro, Leica). The optical isolator is

introduced along the optical path to solve the existence of back-reflections into the cavity that results in undesired amplitude and phase noise at the device output. For collecting the light at the end of the device, a four quadrants photodetector (S4349, Hamamatsu) is employed. Signal acquisition is performed in real time using a home-made LabVIEW software (National Instruments, USA).

The sensor chip is placed on a custom-made holder with a 3-axis translation platform for the proper alignment of the input beam by end-fire. The sensor holder incorporates a Peltier element, which is connected to a temperature controller, providing temperature stabilization with an accuracy of 0.01 degrees. For the inspection of the correct light in-coupling, a digital camera (AM4113T, Dino-Lite, The Netherlands) is placed above.

3.3.2. Fluid delivery system

For the evaluation of liquid samples, a dedicated flow cell is employed. The flow cell is designed and fabricated by soft-lithography using PDMS (SYLGARD 184 Silicone Elastomer Kit, Dow Corning, USA), an inexpensive and durable elastomer. We decided to fabricate a five-channel PDMS flow cell (channel of 18.5 mm long, 1.25 mm wide and 0.5 mm high) to measure with different sensors of the same chip. It is generated from a poly(methyl methacrylate) (PMMA) topographic master. The high hydrophobicity of the resulting PDMS channels is reduced by the polymer PEG 200 (Sigma-Aldrich, Spain) applied after an ozone plasma treatment of the sensor chip in order to expose functional groups on the polymer surface.

The flow cell is then interfaced with the BiMW sensor to confine the liquid samples through the sensing window during experiments. A constant flow is delivered to the fluidic channels using polytetrafluoroethylene (PTFE) tubing, a syringe pump (NE300, New Era) and an injection valve (150 µL sample loop, V-451, Idex), which allows the injection of different solutions (e.g. sample, regeneration buffer) while maintaining a constant flow over the sensing area.

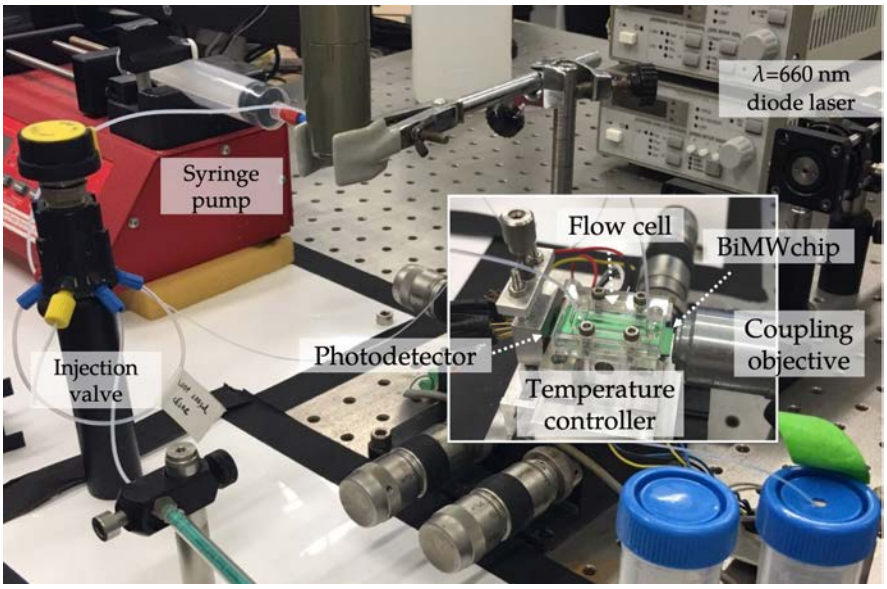

Figure 3.5. Photograph of the experimental BiMW sensor set-up.

3.4. Sensor chip

The BiMW sensor chips had to be optically polished and perfectly cleaned before their experimental evaluation. Then, the bulk sensitivity of each BiMW sensor in a chip was evaluated prior to the (bio)functionalization of the sensor surface.

3.4.1. End-faced polishing

A polishing step is required in order to obtain an optical quality faced of the waveguide sensor, with the aim of minimizing scattering during the end-fire coupling. The sensor chips were manually polished by employing a lapping machine Logitech CL50 (see Figure 3.6). The sensor chips were positioned perfectly vertical over the rotating polishing platform by using a micrometric positioner and allocated using wax to avoid any damage. Adhesive abrasive papers with decreasing grain size were used, starting from a roughness of 9 μm and then 0.3 μm until the sensor chip end-faced was considered optically flat. A water flow was used during the whole process, to wash out particles and debris that could compromise the surface quality.

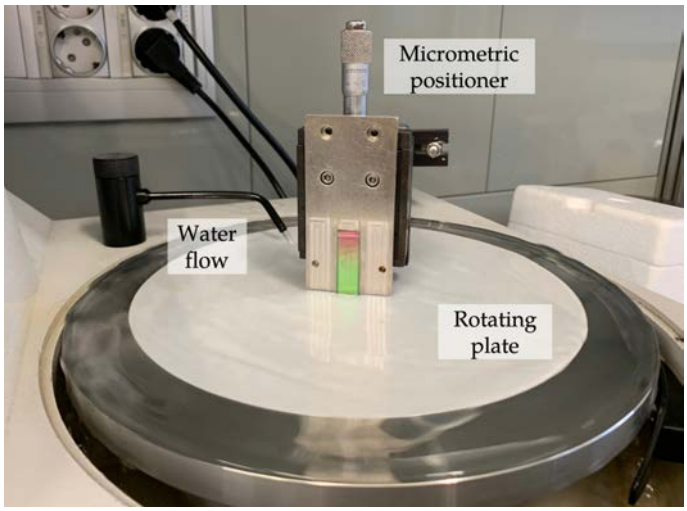

Figure 3.6. Lapping machine with the rotating plate, the micrometric positioner with the sensor chip vertically aligned and the water flow.

3.4.2. Sensor chip cleaning

To remove the protective photoresist and the residues generated during the polishing process, the sensor chips were cleaned by sequentially rinse with acetone (99.5 %, Panreac, Spain), ethanol (96 %, Panreac, Spain) and water (Millipore, USA), followed by sonication in methanol/hydrochloric acid 1:1 (v/v) (MeOH, 99.5 %, Panreac, Spain; and HCl, 37 %, Panreac, Spain) for 10 min, then rinsed with water and dried with a stream of pure nitrogen.

3.4.3. Sensitivity evaluation

To evaluate the bulk sensitivity of the BiMW sensor, it is required to perform a calibration curve. Each sensor chip had to be individually evaluated by injecting successive solutions with different refractive indexes. First, five different concentrations of HCl (0.025 M, 0.05 M, 0.075 M, 0.1 M and 0.25 M) were evaluated with an ABBE Refractometer (Optic Ivymen System, Spain) to determine the refractive index of each sample. The HCl solutions were chosen because they do not affect the sensor surface (i.e. modifying it by oxidation nor produce any deposition by residues). Then, the different HCl solutions were injected to measure the phase variation

(Δϕ) caused by the refractive index change from water to the solution of HCl (Table 3.1). This phase variation was evaluated *versus* the refractive index change (Δn) (Figure 3.7).

Table 3.1. Refractive index change induced by a set of HCl solutions and corresponding phase changes evaluated on a BiMW sensor.

HCl concentrations (M)	Δn (RIU)	Δϕ (π rad)
0.025	$1.2 \cdot 10^{-4}$	0,95
0.05	$4.4 \cdot 10^{-4}$	1,79
0.075	$7,2 \cdot 10^{-4}$	2,70
0.1	$1 \cdot 10^{-3}$	3,82
0.25	$2.4 \cdot 10^{-3}$	8,98

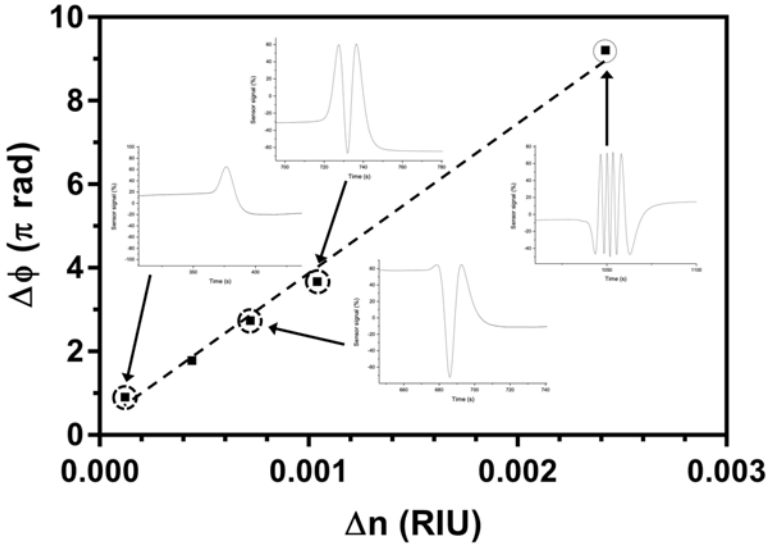

Figure 3.7. Calibration curve of a BiMW sensor. The phase change was evaluated as a function of the refractive index variation due to the injection of HCl concentrations. Inset: output signals for different HCl concentrations. The evaluated concentrations of HCl were: 0.025 M, 0.05 M, 0.075 M, 0.1 M and 0.25 M.

The LOD (Δn_{min}) can be calculated using eq. 4. The phase resolution ($\Delta\phi_{min}$) was evaluated from the measured S_R resolution ($\Delta S_{R,min}$) and this is estimated as three times the standard deviation of the baseline noise, σ_{SR}. The resulting equation is:

$$\Delta n_{min} = \frac{\Delta\phi_{min}}{S_{bulk}} = \frac{\Delta S_{R,min}}{S_{bulk}} \frac{\pi}{2V} = \frac{3 \cdot \sigma_{S_R}}{S_{bulk}} \frac{\pi}{2V} \qquad (4)$$

For the measurements shown in Figure 3.7, we had an experimental sensitivity of S_{bulk} = 3549.6 π rad/RIU (R^2 = 0.997), V = 64,2 % and noise of the system σ = 0.04 %. The BiMW interferometric configuration shows an excellent LOD of $2.7 \cdot 10^{-7}$ refractive index units (RIU), which is in the same range than other classical interferometric waveguide devices.

Chapter 4

Analysis of Irgarol 1051 in seawater with a bimodal waveguide interferometer immunosensor

This chapter focuses in the development of a BiMW immunosensor for the detection of the pesticide Irgarol 1051 in seawater. Special attention has been focused on the selection of the optimal surface biofunctionalization strategy for the sensor surface. Additionally, diverse parameters affecting the biosensor performance have been optimized. Finally, the developed immunosensor has been successfully applied for the sensitive detection of Irgarol 1051 directly in seawater samples.

4. Analysis of Irgarol 1051 in seawater with a bimodal waveguide interferometer immunosensor

4.1. Introduction

4.1.1. The target analyte: Irgarol 1051

An herbicide is a chemical substance that inhibits or interrupts the growth and development of unwanted plants. There is a wide variety of herbicides but one of the most employed families are the triazines. These herbicides are organic chemical compounds with a common structure based on nitrogen-containing heterocycles. They can be classified as symmetric (s-triazines) and non-symmetric based on the nitrogen distribution in the heterocyclic aromatic ring (Figure 4.1).[101] The persistence in the environment of the s-triazines varies between 4 and 12 months but they can last up to 2 years.[102]

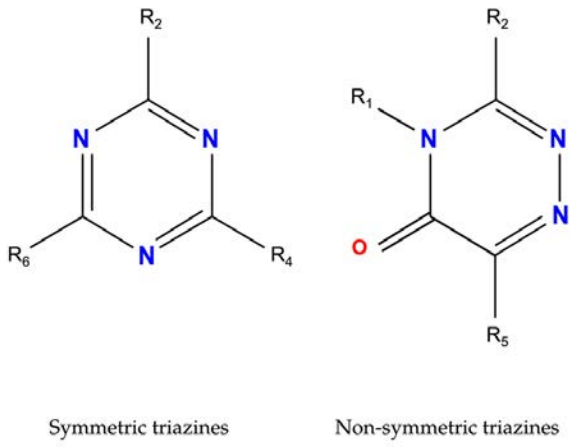

Figure 4.1. General structure of the triazine herbicides.

One class of the s-triazines is the methylmercaptotriazines with an SCH_3 substituent. Among this class of herbicides, Irgarol 1051 (molecular weight of 253 Da), also known as cybutryne, is a common booster biocide added to antifouling paints for marine vessels (Figure 4.2).

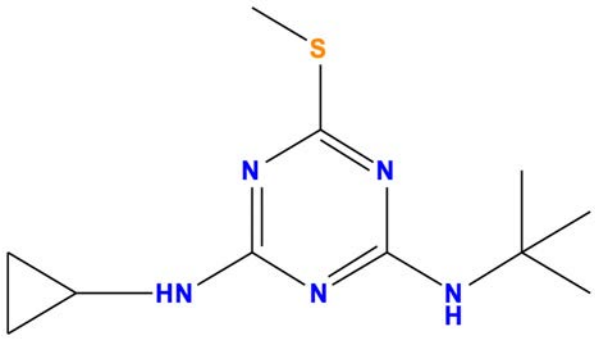

Figure 4.2. Chemical structure of Irgarol 1051.

This algaecide is used in the formulation of antifouling paints because the copper based antifoulants have to be supplemented with organic booster biocides in order to prevent the adhesion and growth of algae.[103] Irgarol 1051 is a photosynthetic inhibitor interfering with the Hill reaction and, therefore, on the electron transport of the photosystem II by binding to the D1 protein of chloroplasts (Figure 4.3).[104] It is slowly released from the paint and because of that, together with its persistence in surface waters and aquatic ecosystems, causes major concerns in the damage of the marine biodiversity. As a result of its spread use is the most frequently detected antifouling biocide worldwide,[105] being found in both aquatic ecosystems and coastal waters.[106,107] Depending on the analytical method employed, the reported concentrations varies from non-detectable up to low part per billion.[105] High frequency of Irgarol 1051 can be found in ports, marinas and fishery harbors and usually higher levels are reported in early summer, probably related to the seasonal boating activity.[108] Because of that, the European Water Framework Directive (WFD) 2013/39/EC included Irgarol 1051 as a priority pollutant in the field of water policy, setting 16 ng L^{-1} as the environmental quality standard (EQS) expressed as maximum allowable concentration.[109]

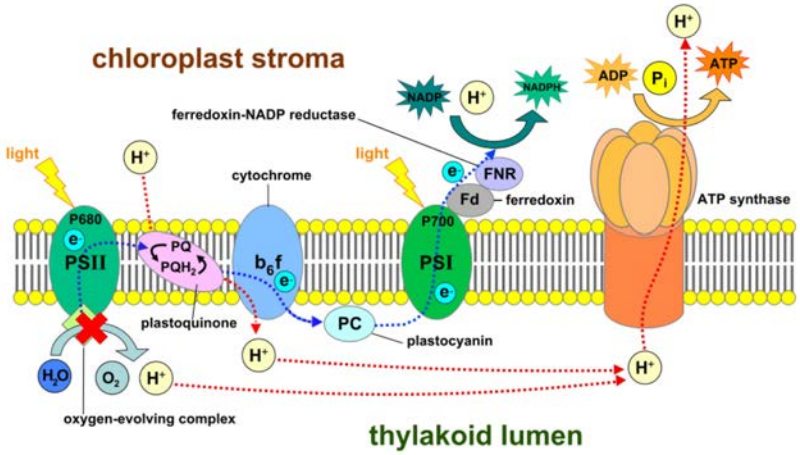

Figure 4.3. Irgarol 1051 inhibits the Hill reaction of the photosystem II at the thylakoid membrane (Source: Somepics)

There are very few described biosensors for Irgarol 1051 detection. For example, a marine green microalgae was genetically modified for luminescence monitoring, with a detection of a 50 % effective concentration (EC_{50}) of Irgarol, after 2 days, of 760 ng L^{-1}.[110] Another recent example is an amperometric immunosensor based on an indirect competitive assay.[111] The chosen detection format requires a secondary conjugated antibody with the consequent need to employ more reagents and an extra assay step as compared to a label-free scheme. The LOD of 38 ng L^{-1} achieved was low enough for some reported levels in seawater,[105] but not as good as the one achieved by standard chromatographic methods and not achieving the value of maximum allowable concentration (16 ng L^{-1}) set by the EU (Table 4.1).

Table 4.1. Chromatographic techniques reported for the measurement of Irgarol 1051 in seawater.

Technique	LOD	Ref
GC – MS	4 ng L^{-1}	112
HPLC – APCI – MS	5 ng L^{-1}	113
LC – MS/MS	0.1 ng L^{-1}	114
HPLC – MS/MS	0.004 ng L^{-1}	115

4.1.2. The biorecognition layer

A key feature during biosensor development is the chosen bioreceptor layer that will affect the final specificity, affinity, response time and lifetime of the biosensor.[116] The chosen biorecognition molecules have to fulfill the following characteristics: high specificity and affinity for the target analyte, form a stable complex with the analyte but dissociate without degrading, the interaction has to be detectable by the optical transducer, and the affinity and specificity cannot be overly altered once it is immobilized on the sensor surface.[117] The most common bioreceptors that can be employed in biosensors are:

- *Enzymes*: are macromolecular biological catalysts. The main advantages are the stable source of material and the possibility to enhance their performance through genetic engineering.[118] But some limitations still exists for choosing this type of receptor for the detection of pollutants: the few contaminants that can be catalyzed by an enzyme, the low specificity for a single type of pollutant, and the limiting conditions (e.g. pH, temperature, solvent).[119]

- *Antibodies*: are proteins generated by the immune system in order to neutralize antigens. The main advantage is the high affinity and specificity between the antigen and the antibody.[120] The main drawbacks are that antibodies denature and degrade under harsh working conditions and production of monoclonal antibodies can be difficult and expensive.[121] Taking into account the main advantages, antibodies were the selected biorecognition elements for the developed biosensor.

- *DNAs*: they are polynucleotides strands very selective and stable for the detection of complementary DNA strands. For pathogen detection, they have some drawbacks as it is required many pre-treatment steps for the cell disruption, making the overall sensing process longer and with many steps involved.[122]

- *Aptamers:* an aptamer is a single oligonucleotide strand forming a 3D structure produced *in vitro* using the systematic evolution of ligands by exponential enrichment (SELEX) process.[123,124] The main advantage is that they are more stable than other bioreceptors, such as antibodies, but obtaining aptamers for any type of analyte is still challenging.[121]

- *Molecular imprinted polymers (MIPs)*: are a novel class of recognition elements biomimicking the antibodies. MIPs are artificial polymers which cavities are chemically modulated to detect the target analyte with high affinity. Some advantages are that they could improve the selectivity and work under fairly harsh conditions. However, few articles report the use of MIPs owing to the difficulty to obtain the desired characteristics for the MIP receptor.[125,126]

4.1.3. Immunosensors

Antibodies, also known as Immunoglobulins (Ig), are glycoproteins synthesized by B cells of the adaptive immune system and used to specifically recognize and neutralize foreign agents (the antigens). A monomeric Ab has an Y-shape structure with a molecular weight (MW) of around 150 kDa and an estimated height of 15 nm (Figure 4.4).[127] Each monomer has two light chains (L) and two heavy chains (H) linked by disulfide bonds. Both types of chains contain the variable and the constant regions. The variable region, the Fab (Fragment antigen-binding) region, at the extremes of the Y arms is different in each type of Ab and is the responsible to recognize and bind to the Ag. This specific recognition sites in the Ab are called paratope and the epitope is the recognized region in the Ag. The constant region is the base of the Y, called the Fc (Fragment crystallizable) region, and is the responsible to interact with the cell surface receptors of the immune system. Depending on the heavy chain structure, there are five classes of Igs or isotypes in mammalian cells: IgA, IgD, IgG, IgE and IgM. The majority of the Abs in the immune system are the monomers IgGs and also the most widely used in analytical immunochemistry.

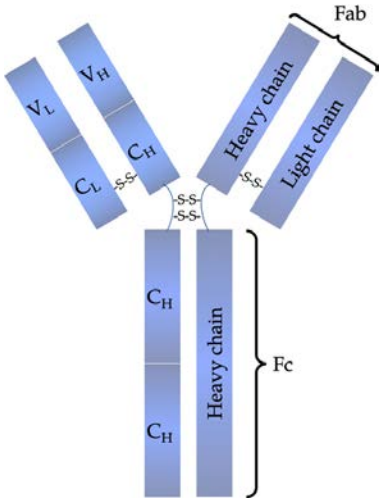

Figure 4.4. Basic structure of an antibody.

The affinity of the antibody for an antigen is based on the combination of physical forces, van der Waals and hydrophobic interactions and hydrogen bonds. On the other hand, the specificity depends on the affinity between the antigen and the binding sites of the antibody. This affinity can cause cross-reactivity with other analytes depending on the affinity degree for more than one antigen.

The synthesis of antibodies is generated in biotech laboratories when an animal repeatedly exposed to the Ag produces a large number of antibodies with different epitope affinities and specificities, known as *polyclonal antibodies* (PAb). Usually, pollutants, like Irgarol 1051, are low molecular weight analytes (MW < 5 kDa) not capable to generate an immune response. They need to be first covalently attached to a macromolecule, generally an inert protein, and later injected to an animal (see Figure 4.5). To generate these conjugates, it is usually required to previously synthesize an analogue derived from the analyte, called hapten, with a functional group capable to covalently attach to the protein. This hapten is designed to have a very similar structure, symmetry, electronic distribution and hydrophobic characteristics to the pollutant because this part has to be the one recognized by the antibody. The polyclonal antibodies are easy to obtain, directly from the immunized serum of the animal, but

a limited amount is produced for the same animal and the properties may vary between animals.

For the Irgarol biosensor, we have employed the hapten *4e*, an Irgarol 1051 chemical derivative with a carboxylic group (4-[N-4-(cyclopropylamino)-6-(methylthio)[1,3,5]triazin-2-yl]aminobutyric acid), the *4e*-conalbumin conjugate (*4e*-cona) and the anti-Irgarol antibody (As87). All of them have been previously described and synthesized at the Nanobiotechnology for Diagnostics Group (Nb4D), IQAC-CSIC (Spain).[128,129]

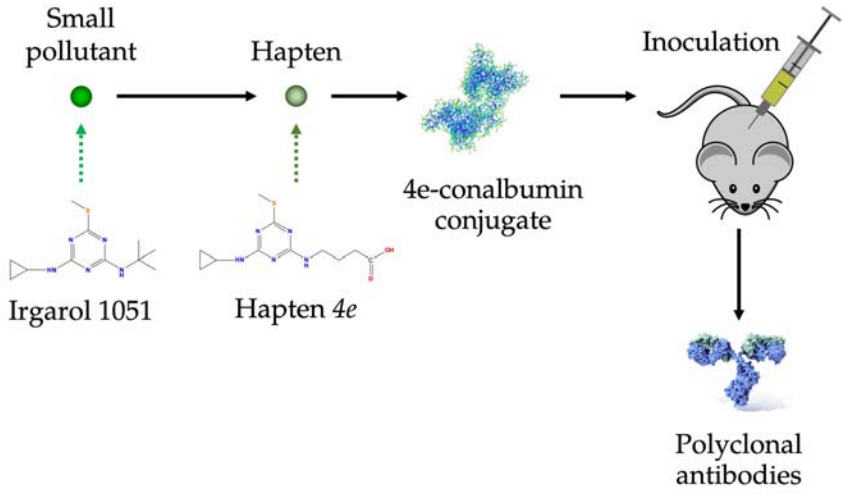

Figure 4.5. Scheme of the basic steps involved in the production of polyclonal antibodies against low molecular weight pollutants. This example represents the production of the anti-Irgarol antibodies synthesized at the Nanobiotechnology for Diagnostics Group (Nb4D), IQAC-CSIC (Spain).

Monoclonal antibodies (MAbs), on the other hand, are produced by the fusion of B cells with tumor cells (myelomas) producing immortal cell lines, known as hybridomas. MAbs are specific for a single epitope and are obtained from a single cell clone. This highly stable immortal cell line can produce an unlimited number of antibodies but require sophisticated material and equipment and trained personnel.

There are different **label-free immunoassays** formats for biosensors. In these immunoassays, the incorporation of labels in the immunoreagents is not required making the assay cheaper and simpler. The classification of the label-free immunoassays differs from the labeled ones, explained in the introduction, and is as follows (Figure 4.6):

- *Non-competitive immunoassay:* the antibody is immobilized onto the sensor surface and the analyte is then directly detected, giving a response proportional to the antigen concentration. Regeneration can be performed for few cycles because the antibody activity is affected by the harsh regeneration conditions. For pathogens or virus, the direct immunoassay is the chosen detection format.

- *Sandwich immunoassay:* is a non-competitive assay were the antibody is also immobilized onto the sensor surface and then allowed to interact with the analyte in the sample. After the biomolecular interaction Ab-Ag has taken place, an excess of a secondary antibody is added to interact with a different epitope present in the antigen. With this format, the sensitivity and selectivity are improved but only large antigens with two different epitopes are suitable for this type of detection.

- *Competitive immunoassay:* is the most popular immunoassay format for label-free detection in environmental monitoring. This is because most of the pollutants are low molecular weight (<5 kDa) and cannot be directly detected. This assay format consists in the immobilization of a conjugate or an analogue of the target analyte onto the sensor surface. The analyte is then mixed with a fixed concentration of antibody and then added to the sensor surface. The unbound antibody is the detected signal, giving a response inversely proportional to the analyte concentration. The main advantage of this assay format is the capacity to perform many cycles because the regenerations weakly affect the stability of the sensor surface.

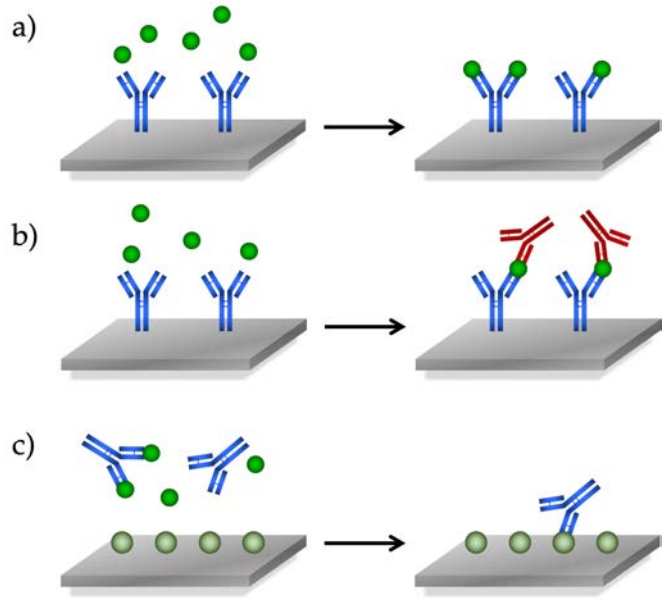

Figure 4.6. Main formats of immunoassays in label-free biosensors: (a) non-competitive immunoassay, (b) sandwich immunoassay and (c) competitive immunoassay.

In order to be able to perform label-free biosensing evaluation of the low molecular weight Irgarol 1051 pollutant, a competitive immunoassay format was selected (Figure 4.7). This assay format was expected to show better signal-to-noise ratio than a non-competitive assay as the detected molecule is the high molecular weight antibodies (~ 150 kDa) in comparison with the pollutant Irgarol 1051 (253 Da). The chosen immunoassay is not only more appropriate in terms of sensitivity, but it also provides a higher stability and higher reusability. After each measurement, the antibody-analyte interaction could be dissociated by a regeneration solution and then, the (bio)surface could be reused for different cycles. Surfaces functionalized with target molecule derivatives as receptor are more suitable to resist many regeneration cycles than those functionalized with antibodies, which easily denatures and lose their biological activity. The chosen antibody was previously developed and proved to be effective for Irgarol 1051 detection in seawater samples with an ELISA.[128,129] In these previous ELISA immunoassays, it was also

corroborated the inherent affinity and selectivity of the polyclonal antibodies produced against Irgarol 1051.

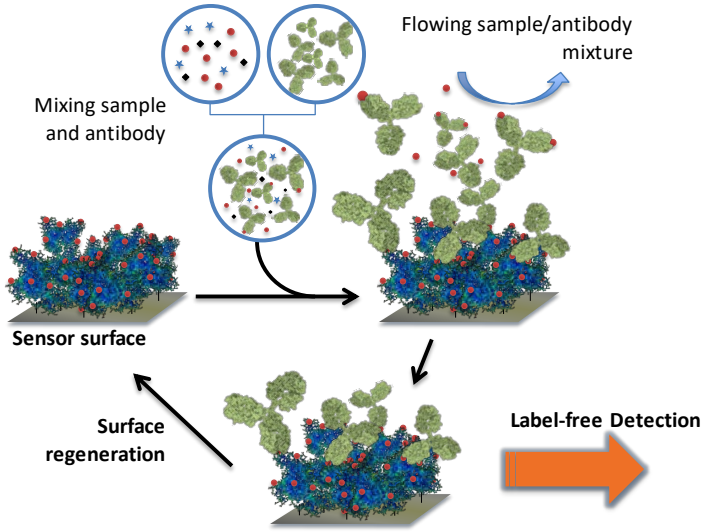

Figure 4.7. Steps of a competitive immunoassay format for label-free detection.

In a competitive immunoassay, the calibration curve is represented with the sensor signal response versus the analyte concentration in a logarithmic scale (Figure 4.8). In the case of the BiMW sensor, the sensor signal obtained for each sample evaluation was expressed in phase variation of the sensor considering that a complete oscillation or fringe of the interferometer corresponds to a 2π rad phase variation. For a clearer representation of the data, the sensor response was normalized following eq. 5:

$$Normalized\ response = \frac{(B - B_\infty)}{(B_0 - B_\infty)} \qquad (5)$$

where B represents the phase variation for the analyzed sample, B_∞ the phase variation of the background obtained for a sample present in an excess of Irgarol 1051 and B_0 is the phase variation for a sample free of Irgarol 1051. Calibration curves were plotted as normalized signal *vs.* Irgarol 1051 concentration, in logarithmic scale. Finally,

results were fitted to a four-parameter logistic equation (sigmoidal) (eq. 6):

$$Normalized\ signal = \frac{A_{max} - A_{min}}{1 + \left(\frac{[Analyte]}{IC_{50}}\right)^{b}} + A_{min} \qquad (6)$$

where A_{max} is the asymptotic maximum, A_{min} is the asymptotic minimum, b represents the curve slope at the inflection point and half maximal inhibitory concentration (IC_{50}) is the concentration of Irgarol 1051 at the inflection point (concentration giving 50 % inhibition of A_{max}). The LOD was calculated as the Irgarol 1051 concentration for which antibody binding to the immobilized hapten was inhibited by 10 %. The dynamic range of the assay was evaluated as the Irgarol 1051 concentration that produced a normalized signal between 20 % and 80 % of B_0.

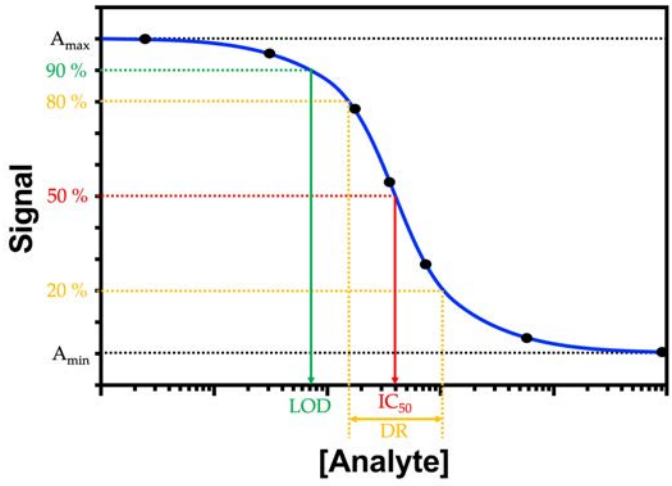

Figure 4.8. Representation of a dose-response inhibition fitting curve.

4.1.4. Immobilization of biorecognition elements

The level of specificity, selectivity and accuracy that can be achieved with the photonic sensor technology for environmental

applications is not only related to the bioreceptor employed but also to the functionalization protocol, rather than to the transducer itself. Key factors are: (i) functionalization protocols which preserve the activity and the functionality of the bioreceptor once attached to the sensor surface; (ii) allows high packing density of the biorecognition element while avoiding steric hindrance during the biointeraction; and (iii) ensures antifouling properties of the bioreactor layer for detecting directly in real matrices.

The main procedures for surface biofunctionalization are (see Figure 4.9):

- *Physical adsorption*: is the simplest strategy were the biomolecule is directly adsorbed onto the sensor surface via intermolecular forces like van der Waals, hydrophobic and electrostatic interactions. This technique is widely employed in solid-based assays like ELISA with the advantage of not requiring any additional step. The main drawbacks are caused by the weak physical interactions that are very sensitive to experimental condition changes and poor reproducibility and stability.[130] For example, flow-through assays or changes in the pH or buffer can easily desorb the attached biomolecule. Also, the uncontrolled orientation of the bioreceptor may cause loss of affinity for the analyte, unfolding or denaturation.

- *Biochemical affinity*: is a site-specific functionalization when using bioreceptors like antibodies that require an oriented immobilization to avoid the modification of the binding sites. It is based in strong interactions like the one between biotin and avidin (or streptavidin) or using cofactors or site-directed affinity proteins. The main drawbacks of this methodology is the need to modify the native molecules, some stability problems and the need of an extra step for the biomolecule conjugation.[131,132]

- *Physical entrapment*: is a single step procedure for the incorporation of the biomolecules in a uniform polymer matrix. With this methodology, there is no need to include specific charges to the

biomolecular and/or the transducer surface. The most employed polymers are polyaniline, polythiophene, polypyrrole and dextran-based polymers. The main advantages are a better preservation of the biomolecules and, theoretically, a larger number of available binding sites. But on the other side, this approach suffers of diffusion and mass transport problems of the analyte towards the bioreceptor.[133]

- *Covalent immobilization*: this strategy implies an irreversible binding of the biomolecules onto the transducer surface by covalent bonds.[134,135] It is usually the best approach in terms of longevity of the bioreceptor layer, reproducibility, immobilization yield, interaction efficiency and sensitivity. This functionalization also avoids changes in the structure of the biomolecule placing it away from the surface. For the covalent linkage of the bioreceptors on the surface, a previous chemical activation to generate functional groups onto the transducer is required. These additional steps and the overall complexity of the procedure are the main drawbacks. The most common covalent functionalization protocols are based on the modification of the surface with amine or thiol groups.

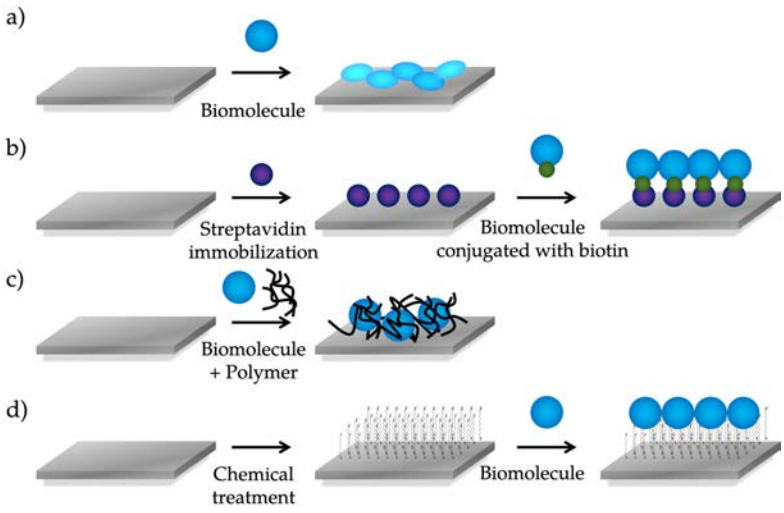

Figure 4.9. Main procedures for surface biofunctionalization: (a) physical adsorption, (b) biochemical affinity, (c) physical entrapment, and (d) covalent immobilization.

In summary, the accomplishment of a highly sensitive and reliable biosensor stands heavily on an optimum biofunctionalization strategy to achieve high affinity, sensitivity, stability and antifouling properties.

In the case of silicon based materials, like the silicon nitride material of the BiMW interferometer, most of the biofunctionalizations are covalent immobilizations. They are done with organosilanes because of the stability and the rapid covalent linkage.[136] The alkylsilane monolayers form from the reaction of a silane with the hydroxyl groups of the oxidized Si_3N_4 surfaces. This procedure is called silanization and most common organosilanes used for biofunctionalization are 3-aminopropyltriethoxy silane (APTES, with an amino-ended surface),[137,138] carboxyethylsilanetriol sodium salt (CTES, with a carboxylic acid-ended surface),[139] 3-glycidyloxypropyltrimethoxysilane (GOPTS, with an epoxy-ended surface)[140,141] isocyanatepropyltriethoxysilane (ICPTS, with a isocyanate-ended surface),[142,143] and (3- mercaptopropyl) trimethoxysilane (MPTMS, with a thiol-ended surface).[144] All of them have a length of around three carbons to maintain the receptors as close as possible to the sensor surface. In EW-based sensors, this is crucial since the evanescent field exponentially decays as it penetrates in the outer medium.

The alkylsilanes have a dual behavior with an organic and an inorganic part. The first are the functional tail groups (R_n-) that introduce the specific terminal groups to subsequently immobilize the (bio)recognition elements. The inorganic part provides the anchorage to the sensor surface, reacting with the hydroxyl-terminated silicon surfaces. This reaction involves two steps (Figure 4.10). In the first step, the alkylsilanols stablish hydrogen bonds with the free hydroxyl groups or with adsorbed water molecules on the surface. In the second step, the condensation and release of water molecules generates the covalent bonds. Water has a catalytic effect. Therefore, a close control of the water concentration is critical to ensure reproducibility. The final bond leads to the formation of thermally and relatively chemically stable siloxane bonds (Si-O-Si).

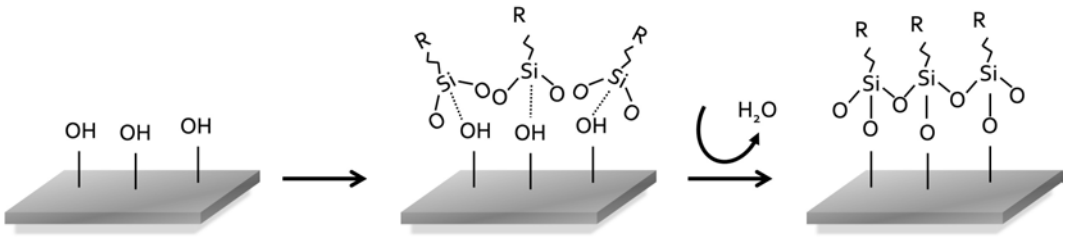

Figure 4.10. Scheme of the reaction of organosilanes with the silicon surface.

The choice of the type of silane and the reaction conditions are crucial for a careful control of the density of the bioreceptors immobilized in the sensor surface. This will directly affect the analytical performance of the biosensor. In addition, the biofunctionalization protocol should avoid as much as possible the non-specific adsorptions from a complex matrix as the seawater. For that reason, we have evaluated six different functionalization protocols based on chemical silanization and subsequent covalent attachment of the receptor.

4.2. Materials and methods

4.2.1. Reagents and materials

Acetone (99.5 %, Panreac, Spain), ethanol (96 %, Panreac, Spain), ethanol absolute (99.5 %, Panreac, Spain), hydrochloric acid (HCl, 37 %, Panreac, Spain), methanol (MeOH, 99.5 %, Panreac, Spain), nitric acid (HNO_3, 65 %, Panreac, Spain), anhydrous toluene (99.8 %, Sigma-Aldrich, Spain), CTES (ABCR, Germany), mPEGSilane-COOH (silane-PEG-COOH, 600 MW, Interchim, France), APTES (Sigma-Aldrich, Spain), *p*-phenylenediisothiocyanate (PDITC, Sigma-Aldrich, Spain), dimethylformamide (DMF, Sigma-Aldrich, Spain), N,N-diisopropylethylamine (DIPEA, Sigma-Aldrich, Spain), N-(3-dimethylaminopropyl)-N'-ethylcarbodiimide hydrochloride (EDC, Sigma-Aldrich, Spain), N-hydroxysulfosuccinimide sodium salt (sulfo-NHS, Sigma-Aldrich, Spain), carboxymethyl-dextran sodium salt (CM-dextran, Sigma-Aldrich, Spain) and amino dextran (amine-dextran; 10 kDa, 5 moles

amine/mole; Molecular Probes, USA) were used as received without further purification.

The chemicals for phosphate-buffered saline (PBS; aqueous solution of 10 mM Na_2HPO_4, 1.8 mM KH_2PO_4, 2.7 mM KCl and137 mM NaCl, pH adjusted to 7.4), MES buffer (solution of 0.1 M 2-(N-morpholino)ethanesulfonic acid (MES) and 0.5 M NaCl in water, pH 5.5), ethanolamine hydrochloride (1 M, pH 8.5) and acetate buffer (AB; 50 mM CH_3COONa at pH 5.5) were purchased from Sigma-Aldrich (Spain).

Stock solutions of Irgarol 1051 (1 mg mL^{-1}) were prepared in DMF and stored at 4 °C. All solutions were filtered through 0.2 µm nylon membranes (VWR international, USA). Milli-Q water from Millipore (USA) was always employed.

4.2.2. Surface functionalization

Since the chosen immunochemical format is a competitive configuration, we decided to covalently immobilize on a previously silanized sensor surface an haptenized protein (competitor bioconjugate) or the hapten *4e*. The bioconjugate *4e*-cona is a protein conalbumin with many derivatives *4e* covalently attached in order to increase the number of binding sites. The hapten *4e* is an Irgarol 1051 chemical derivative with a carboxylic group that can be covalently attached to the sensor surface. To evaluate the most suitable biofunctionalization procedure, several silanization protocols were employed (Figure 4.11).

Prior to functionalization, the sensor chips were cleaned as previously explained. Cleaned sensor chips were then oxidized using oxygen plasma (40 kHz and 100 W, 45 scm, Femto oxygen plasma, Electronic Diener, USA) for 5 min. The pre-treated chips were subsequently immersed in a 15 % HNO_3 solution at 75 ˚C for 25 min, rinsed generously with deionized water, dried carefully under nitrogen flow and immediately functionalized.

- **Surface biofunctionalization with *4e*-cona conjugate**

- *Covalent immobilization of 4e-cona on CTES-treated surfaces (Surface I)*

The functionalization protocol using CTES has been previously described.[139] Briefly, the sensor chip was immersed in an aqueous solution of 0.5 % CTES for 1 h, cleaned with water and dried using a nitrogen stream. Finally, the sensor chip was cured in an oven for 1h at 110 ˚C.

The PDMS fluidic system was then placed over the silanized sensor surface. A 50 μg mL^{-1} *4e*-cona solution, containing 0.2 M EDC/0.05 M sulfo-NHS in MES buffer, was injected and left to react overnight at room temperature (RT). After, the excess of *4e*-cona was removed by pumping water through the channels at a constant flow rate of 25 μL min^{-1} for 1h. Finally, a blocking of the sensor surface to avoid non-specific adsorptions was done using ethanolamine (1M, pH 8.5) and employing PBS as running buffer at a flow rate of 25 μL min^{-1}.

- *Covalent immobilization of 4e-cona on carboxyl PEG-modified surfaces (Surface II)*

Once the sensor surface was thoroughly cleaned and oxidized, 100 μL of 2.5 % silane-PEG-COOH solution in ethanol-water 95:5 (v/v) was added onto the oxidized chip, covered with a cover slip and left 2 h at 4 ˚C. After incubation, the silanized sensor surface was sequentially rinsed with ethanol and deionized water and dried with N_2. Then, it was autoclaved for 90 min at 120 ˚C. Finally, *4e*-cona was covalently immobilized on the sensor chip following the protocol described for Surface I.

- *Covalent immobilization of 4e-cona on APTES-treated surfaces using PDITC cross-linker (Surface III)*

The hydroxylated sensor chip was treated under nitrogen with 18 % (v/v) APTES and 5.5 % (v/v) acetate buffer (50 mM, pH 5.5) in

ethanol absolute for 10 min under gentle shaking, rinsed with ethanol and dried with a nitrogen stream. The silanized sensor chip was then cured in an oven for 2 h at 120 ˚C. The amine groups were activated with 20 mM PDITC in 10 % of pyridine and DMF in dark for 2 h. After incubation, the sensor chip was washed with DMF and ethanol; and dried with a stream of nitrogen. Finally, *4e*-cona was covalently immobilized on the sensor chip according to the procedure described above for Surface I.

- *Covalent immobilization of 4e-cona on CM-dextran-modified surfaces (Surface IV)*

The sensor chip was silanized with APTES following the protocol described above for surface III. For the immobilization of CM-dextran, the PDMS fluidic system was placed over the silanized sensor surface. A solution of 0.2 M EDC/0.05 M sulfo-NHS in MES buffer with a concentration of 1mg mL^{-1} CM-dextran was injected and left to react 80 min at RT. After, the sensor chip was washed pumping water through the channels at a flow rate of 25 µL min^{-1} for 1h. Finally, *4e*-cona was covalently immobilized on the sensor chip according to the procedure described for Surface I.

- **Surface biofunctionalization with Irgarol derivative *4e***

- *Covalent immobilization on amine-dextran-modified surfaces silanized with CTES (Surface V)*

The sensor chip was first silanized with CTES following the above-mentioned protocol. Then, the PDMS fluidic system was placed over the silanized sensor surface. A solution of 0.2 M EDC/0.05 M sulfo-NHS in MES buffer with a concentration of 1 mg mL^{-1} amine-dextran was injected into each channel and left to react 80 min at RT. After, the sensor chip was washed pumping water through the channels at a constant flow rate of 25 µL min^{-1} for 1h. To immobilize the hapten *4e*, a solution of 0.2 M EDC/0.05 M sulfo-NHS in MES buffer containing 50 µg mL^{-1} of hapten *4e* was pre-incubated

during 30 min under agitation and then, injected into each sensor channel to react overnight at RT with the silane. Finally, the reagent excess was removed pumping water through the channels at a constant flow rate of 25 µL min^{-1} for 1h. Finally, to avoid non-specific adsorptions, the sensor surface was blocked by using ethanolamine (1M, pH 8.5) and employing PBS as running buffer at a flow rate of 25 µL min^{-1}.

- *Direct immobilization on APTES-treated surfaces (Surface VI)*

The sensor chip was silanized with APTES following the procedure described for surface III. The sensor chip was then placed in the experimental set-up with the PDMS fluidic system, and the immobilization was done for each sensor channel individually. Then, hapten *4e* was covalently immobilized on the surface of the sensor chip according to the procedure described for Surface V.

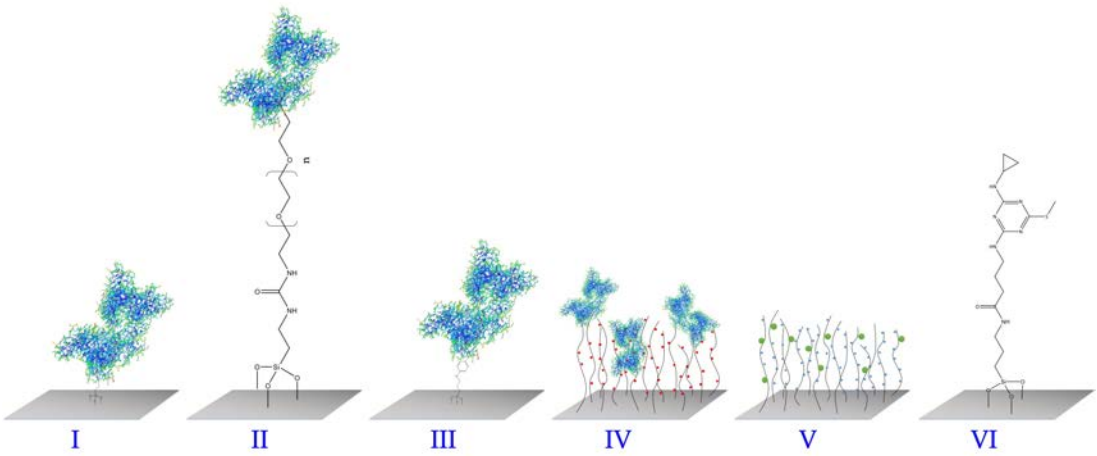

Figure 4.11. Evaluated sensor surfaces: (I) Covalent immobilization of *4e*-cona via CTES; (II) covalent immobilization of *4e*-cona via silane-PEG-COOH; (III) covalent immobilization of *4e*-cona via APTES and the cross-linker PDITC; (IV) covalently cross-linked *4e*-cona via CM-dextran; (V) covalently cross-linked hapten *4e* via amine-dextran; and (VI) covalent immobilization of hapten *4e* via APTES.

4.2.3. Biosensor immunoassay

All the Irgarol 1051 samples were prepared in PBS buffer or seawater. PBS was employed as running buffer at a constant flow rate of 20 µL min^{-1}. Each Irgarol 1051 solution (200 µL) was prepared mixing 2 µL of a fresh stock dilution of 1:20 (v/v) antisera As87 with 198 µL of PBS to reach a final antibody dilution of 1:2000 (v/v). 150 µL of the antibody-sample mixture was injected into the flow cell. During this step, the free antibodies interacted with the hapten immobilized onto the sensor surface. Finally, the sensor surface was regenerated by flowing 50 mM NaOH solution at 25 µL min^{-1} for 2 min. The biosensor response for samples of different concentrations of Irgarol 1051 was evaluated from low to high concentrations and vice versa.

4.3. Comparison of the different evaluated sensor surfaces

Considering that the substrate functionalization is a critical step in biosensor fabrication, the six different functionalization protocols based on wet chemistry methods of silanization and subsequent covalent receptor immobilization were studied in detail. The first step to evaluate a sensor surface in a competitive immunoassay is the effect of the antibody concentration. We evaluated from 1:500 (v/v) to 1:5000 (v/v) anti-Irgarol 1051 serum dilutions for the six surfaces in the BiMW sensor. They were tested in absence of Irgarol 1051 (B_0) and in presence of 100 µg L^{-1} of Irgarol 1051 in the sample (B). For all the surfaces the optimized antisera dilution, in terms of sensitivity (B/B_0 ratio), was a dilution factor of 1:1000 (v/v) except for sensor surface V, which was a dilution factor of 1:1500 (v/v) and for surface VI, which was a dilution of 1:2000 (v/v). Results are summarized in Figure 4.12.

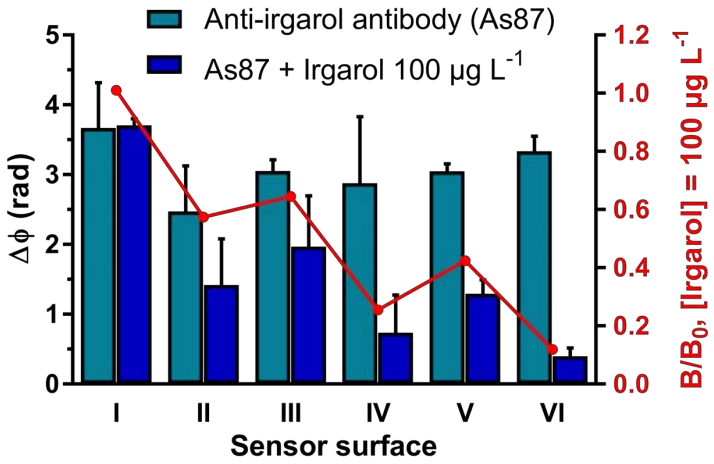

Figure 4.12. Comparison of the different sensor surfaces responses in terms of absolute signal ($\Delta\phi$) and sensitivity (B/B_0 ratio). For sensor surface details, see Figure 4.11. The employed anti-Irgarol 1051 serum for all the sensor surfaces was 1:1000 (v/v) except for sensor surface V, which has a dilution factor of 1:1500 (v/v) and surface VI that has a dilution 1:2000 (v/v).

All the evaluated sensor surfaces produced a response in the presence of a fixed As87 anti-Irgarol serum dilution in PBS in the absence of Irgarol 1051. The highest absolute signal ($\Delta\phi$) was observed for the sensor surface I ($\Delta\phi$ = 3.7 rad), resulting from the covalent immobilization of conjugate *4e*-cona on the BiMW chip previously silanized with CTES. The main advantage of this organosilane is the stability in water avoiding organic solvent handling. Moreover, CTES permits the immobilization of biomolecules inside the fluidic cell (*in-situ*) and the carboxylic group is stable during long periods, once attached on the sensor surface. The main drawbacks are the low surface density of biomolecules and the low stability after the regeneration process. In our experiments, no signal inhibition was observed when As87 anti-irgarol serum (dilution 1:1000, v/v) was first mixed with 100 µg L^{-1} Irgarol 1051 in the sample. This could be caused by a low functionalization yield that leads to a low density of receptors immobilized on the sensor surface. The low receptor coverage potentially leads to the non-specific binding of other

proteins present in the anti-Irgarol 1051 serum falsely increasing the sensor response.

In light of these results, the sensor surface II was functionalized with silane-PEG-COOH prior to the covalent immobilization of the conjugate *4e*-cona. PEGylation is reported to greatly suppress the non-specific binding of charged molecules to the modified surface.[145] The sensor response in terms of absolute signal for As87 anti-irgarol serum (dilution 1:1000, v/v) and in absence of Irgarol 1051 is lower than for surface I. This could be caused by the reduction of the non-specific binding of serum proteins that could show a false increase in the sensor response. As expected, the addition of 100 μg L^{-1} Irgarol 1051 in the sample led to a signal inhibition but relatively low. Because of that, sensor surface III was functionalized with APTES in combination with PDITC previous to immobilize the conjugate *4e*-cona. The cross-linker PDITC has the potential to form well-organized assemblies driven by π-π stacking, also leading to a reduction of non-specific binding of matrix compounds to the functionalized sensor surface.[146] With this functionalization, a small signal inhibition was observed when evaluating the sensor response in the presence of Irgarol 1051. But no improvements were observed compared to surface II.

In order to enhance the number of binding sites and act as a blocking layer itself, CM-dextran (sensor surface IV) and amine-dextran (sensor surface V) were employed. A dextran layer potentially provides a pseudo-3D hydrophilic layer favorable to most antigen-antibody interactions and increases the surface capacity for receptor immobilization in comparison with the previous flat surfaces. The sensor surface IV with *4e*-cona onto CM-dextran-modified surfaces shows a high sensor response in presence of the As87 anti-Irgarol antiserum and in absence of Irgarol 1051 (B_0). Also, the presence of Irgarol 1051 (100 μg L^{-1}) in the sample shows a signal inhibition. The sensitivity (B/B_0 ratio) is significantly better than the previous sensor surfaces with also *4e*-cona immobilized. This improvement is consistent with the formation of a pseudo-3D layer with a higher receptor immobilization capacity. Sensor surface V

together with sensor surface VI use the hapten receptor *4e* as an alternative to cona-*4e* conjugate. As expected, the sensor surface V, CTES-modified surface with an amine-dextran network, shows considerable performance in terms of sensitivity and similar to the sensor surface IV with CM-dextran. In the case of sensor surface VI, hapten *4e* was covalently immobilized onto an APTES-modified surface. This sensor surface shows the best results in terms of sensitivity (B/B_0 ratio) but also the highest absolute signal ($\Delta\phi$) (except from the unspecific response of surface I). Sensor surface VI shows a signal inhibition of 88 % due to the anti-Irgarol inhibited by the presence of 100 $\mu g\ L^{-1}$ of Irgarol 1051 in the sample (B). This was a surprising result because a similar sensitivity enhancement observed for sensor surface IV compared to sensor surface I was expected for sensor surface V compared to sensor surface VI.

In EW-based sensors only events occurring close to the sensor surface will be measured. This is because, and as previously explained, the intensity of the evanescent field is maximum at the surface and decays exponentially as it penetrates the outer medium. When directly attaching the derivative *4e* to the sensor surface via an APTES moiety with a chain of only 3 carbons, the close contact of the receptor to the waveguide surface will enhance the sensitivity. On the other hand, only events occurring close to the sensor surface will be measured. Thus, antigen-antibody interaction in sensor surface VI would occur closer to the surface than that for surface V, in which a larger size cross-linker molecule (amine-dextran network) have been used, leading to the observed enhanced response.

In view of the obtained results, sensor surface VI was selected as the most appropriate one for further biosensor development.

4.4. Optimization of the sensor surface functionalization

Once selected the sensor surface, different parameters during APTES silanization and the immobilization of hapten *4e* were optimized as shown in Table 4.2.

Table 4.2. Summary of the optimized parameters during APTES silanization and immobilization of hapten 4e. AB: 50 mM Acetate buffer

Step	Parameter	Evaluated range	Optimum value
Silanization	Oxidation treatment	UV/O_3 O_2 plasma	O_2 plasma
	Solvent	Ethanol (0 – 5.5 % AB) Toluene	Ethanol (5.5 % AB)
	Silane concentration (%, *v*/*v*)	1 – 18	18
	Silanization time	10 min to 16 h	10 min
Hapten *4e* immobilization	Carrier solution pH	5.0 – 5.5	5.5
	Pre-incubation time (min)	0 – 30	30
	4e concentration (µg mL^{-1})	50 – 250	50

After the cleaning of the silicon nitride surface, oxidation is a key step to generate active silanol groups onto the surface that facilitate the reaction with the silane. Two activation procedures were evaluated with identical results. The first procedure was with UV/O_3 activation (BioForceNanosciences, USA), and the second one was treating the surface with O_2 plasma. UV/O_3 activation is less aggressive and takes 90 min to achieve a highly hydrophilic surface (water contact angle lower than 5°).[139] Since the surface treated with O_2 plasma takes only 5 min, this latter was chosen as the activation procedure.

There are several advantages when using silanization with APTES such as (bio)receptor stability, high immobilization density, reduced biofouling, leach-proof biomolecule binding, and enhanced analytical performance. We evaluated three different reported silanization protocols. In all the cases, the reactions took place under a nitrogen atmosphere to obtain a compact monolayer. In the first protocol,[147] the activated sensor chip was incubated overnight into a 1 % (v/v) APTES solution in dry toluene and with 0.3 % v/v of DIPEA to catalyze the hydrolysis reaction. To control the extent of polymerization of the silane, there are many optimized organic

silanization protocols using toluene. The problem with APTES is that the surface density closely depends on the solvent viscosity and an aromatic solvent like toluene may not be ideal and is also not eco-friendly.[136] Two other protocols using absolute ethanol as solvent were evaluated. In the second protocol, the hydroxyl-activated sensor chip was transferred to a 1 % (v/v) APTES solution prepared in absolute ethanol for 1 h.[99] In the third protocol,[148] the activated chip was transferred to an 18 % (v/v) APTES solution prepared in absolute ethanol with 5.5 % of acetate buffer for 10 min under mild agitation. The presence of water in the buffer catalyzes for the hydrolysis of the silane under a stable pH. The high concentration of APTES and the mild agitation reduces the reaction time to only 10 min. Longer times may render in the generation of thicker multilayers.

For the evaluation of the optimal silanization protocol, the optimal antibody concentration was first evaluated with different antisera dilutions between 1:500 and 1:5000 (v/v). In all the cases, an antisera dilution of 1:2000 (v/v) showed the best results in terms of absolute signal ($\Delta\phi$) and in terms of sensitivity (B/B_0 ratio). Then, with an antisera dilution of 1:2000 (v/v), a calibration curve was done using standard Irgarol 1051 solutions with concentrations ranging from 0 to 100 μg L^{-1}. All three protocols showed similar results in terms of LOD, IC_{50} and DR, but different sensor surface stability. In the first two protocols, the sensor response was stable only up to 7 – 8 cycles. These results suggest a poorly silanized surface and/or the adsorption of the hapten *4e* instead of covalent immobilization. By contrast, in the last protocol, the resulting chip was stable up to 30 measurements-regeneration cycles. These implies a greater number of silanes covalently bound to the surface and only with a 10 min reaction.

Once optimized the functionalization via APTES, we evaluated the different parameters for the immobilization of the hapten *4e*. First, different concentration of the hapten *4e* during the chip functionalization from 50 up to 250 μg mL^{-1} were tested. Increased concentrations did not lead to a better sensor performance in terms of absolute signal, sensitivity and stability. Therefore, a concentration of

the hapten *4e* of 50 μg mL^{-1} was chosen as the optimum immobilization concentration. Another important parameter was a 30 min pre-incubation time of *4e* with EDC/sulfo-NHS to activate the carboxylic group of the hapten prior to covalently attach to the amine silane.

4.5. Immunoassay optimization

Once optimized the conditions for the sensor surface functionalization, different parameters affecting the immunoassay performance were evaluated. A summary is shown in Table 4.3.

Table 4.3. Optimized immunoassay conditions.

Parameter	Evaluated range	Optimum value
Anti-Irgarol serum concentration, dilution factor (1:x)	500 – 5000	2000
Regeneration: NaOH (mM), 25 μL min^{-1}, 120s	25 – 100	50
Carrier solution	---	PBS (pH 7.4)
Incubation time Ab + Ag (min)	1 – 10	1
Measurement flow rate (μL min^{-1})	15 – 25	20
Total analysis time (min per sample)	---	20

The most critical one, the effect of the antibody concentration, was previously optimized. The best results were obtained for 1:2000 (v/v) being high enough to give a good signal-to-noise ratio, but still a limiting factor to achieve good sensitivity. Higher dilutions presented weaker response in terms of absolute signal ($\Delta\phi$) and lower dilutions were exceedingly high concentrations decreasing the immunoassay sensitivity (Figure 4.13).

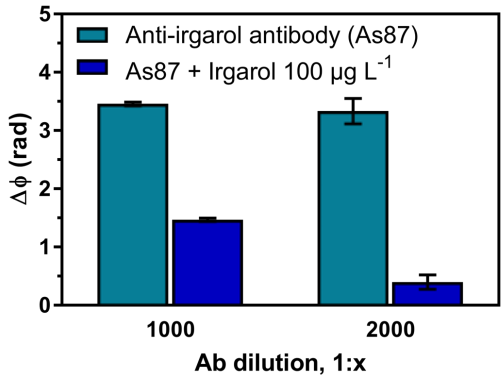

Figure 4.13. Comparison of different anti-Irgarol 1051 serum (As87) dilutions responses in terms of absolute signal ($\Delta\phi$).

In a competitive immunoassay, it is not only important the antibody concentration but also the mixture and incubation time of this antibody with the sample prior to the sensor injection. This allows the appropriate interaction of the antibodies with the Irgarol 1051 present in the sample before they contact the hapten onto the sensor surface. The incubation time was evaluated from 1 up to 10 min. The minimum time was chosen as the optimal, as longer times did not render in better sensitivities.

In order to perform consecutive measurements with the same sensor surface, the regeneration of the surface had to be addressed; that is the removal of the attached antibodies after the detection step without altering the immobilized receptor molecules. Efficient regeneration would provide reusability of the surface, which is particularly important not only to save costs and time, but also to evaluate the stability and robustness of the functionalized surface. To disrupt the biochemical interaction between the antibody and the hapten receptor, a regeneration solution with NaOH was chosen. Other solvents, i.e HCl, did not dissociate the antibody-antigen interaction or destroyed the bioreceptor activity. We evaluated four different concentrations of NaOH with a fixed flow (25 µL min^{-1}) and time (120 s). The effective regeneration of the sensor surface was evaluated with consecutive measurements of antisera dilution 1:2000 (v/v), both without Irgarol and in the presence of a high

concentration of Irgarol 1051 (100 μg L^{-1}). A recovery of the same absolute signal ($\Delta\phi$) indicated an efficient removal of the antibody bound to the sensor surface with minimal surface damage. When regenerating with only 25 mM of NaOH, the absolute signal decreased a 55 ± 10 % in the absence of Irgarol 1051 just after 5 different measurement-regeneration cycles. This was attributed to a non-effective removal of the antibodies bound to the sensor surface. On the other hand, when regenerating with a high concentration of NaOH (100 mM), the performance of the biosensor improved, but the signal still decreased a 20 ± 3 % after 5 cycles in the absence of Irgarol 1051. This decrease is possibly related to the damage of the receptor layer. The optimal value was 50 mM NaOH, where the sensor retains 95 ± 6 % of the initial response after 10 cycles, indicating an efficient regeneration of the sensor surface.

Finally, and since we are working with a fluid delivery system, the effect of the flow rate had to be assessed. The flow rate was analyzed in the range of 15 – 25 μL min^{-1} and evaluated in terms of absolute signal when flowing and antisera dilution 1:2000 (v/v) in the absence of Irgarol 1051. At a flow rate of 20 μL min^{-1}, the absolute signal was 3.3 ± 0.2 rad. When flowing the sample at 25 μL min^{-1}, the sensor signal response decreased 10 ± 2 %, and lower flows did not show better sensitivities. Therefore, the chosen flow rate was 20 μL min^{-1}. With the above-mentioned conditions, the complete measurement-regeneration cycle took around 20 min.

4.6. Analytical performance of the BiMW immunosensor

Using the optimized conditions established before, we obtained a calibration curve using standard Irgarol 1051 solutions, ranging from 0 to 100 μg L^{-1}, in buffer conditions and incubated with a constant concentration of antibody. The normalized calibration curve is depicted in Figure 4.14. The obtained IC_{50} and LOD were 99 ng L^{-1} and 3 ng L^{-1}, respectively. The DR of the immunoassay was from 9 to 1190 ng L^{-1}.

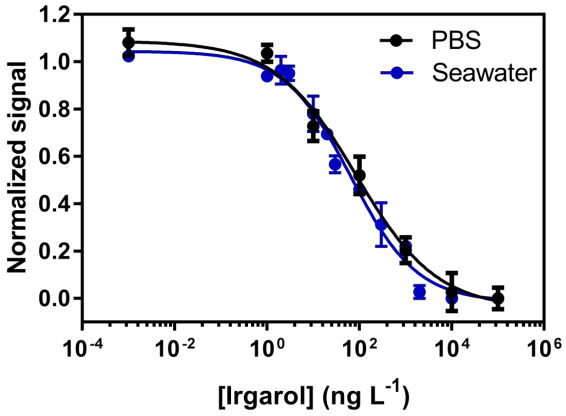

Figure 4.14. Competitive calibration curve obtained in Irgarol 1051 standard solutions in PBS pH 7.4 and in spiked seawater.

The optimized biosensor was stable up to 30 different measurements-regeneration cycles using the same sensor surface (Figure 4.15a). To study the interday reproducibility of the biosensor, a BiMW chip functionalized and stored at RT in air was evaluated in consecutive days using different waveguide sensors. The same sensor response was obtained for consecutive days in terms of absolute signal ($\Delta\phi$) and sensitivity (B/B_0 ratio) confirming the good stability of the sensor surface (Figure 4.15b).

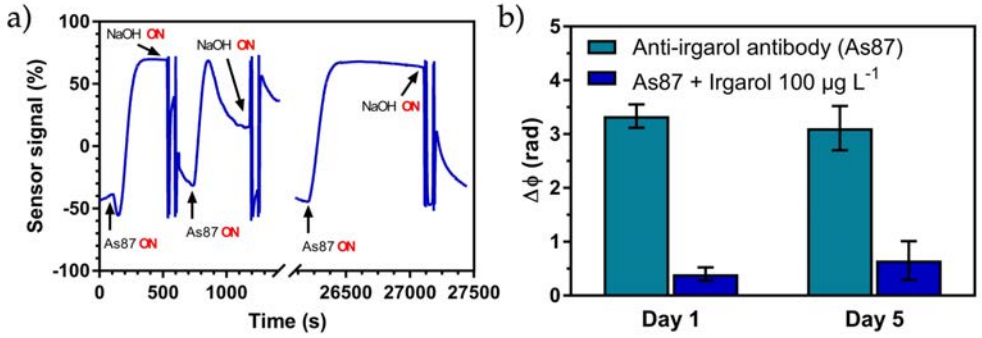

Figure 4.15. (a) Real-time detection of measurement-regeneration cycles 1, 2 and 30 of antisera dilution 1:2000 (v/v) regenerated with 50 mM NaOH. (b) Comparison of day 1 and 5 responses using the same BiMW chip in terms of absolute signal ($\Delta\phi$).

Immunoassays are known to suffer from matrix effects that causes the non-specific binding and denaturation of the antibodies, which results in false positives responses.[149] Thus, the first step for the analysis of Irgarol 1051 in seawater was to measure the sensor response to the flow of seawater alone. The seawater sample had been previously checked and contained undetectable levels of Irgarol 1051. The sensor response to the flow of seawater alone showed the same phase change at the entrance and at the exit, a stable baseline when only flowing seawater and the recovery of the base line (Figure 4.16). This confirmed that the functionalized surface was resistant to non-specific adsorptions showing no background signal due to any matrix effect. On the other hand, the stability of the antibody As87 in seawater was demonstrated in a previous immunoassay, where the salinity did not significantly affected the performance.[128] Moreover, the immunocomplex stability was previously confirmed with an ELISA assay for a wide pH range,[129] including the pH of seawater that is usually in the range of 7.5 – 8.4.[150]

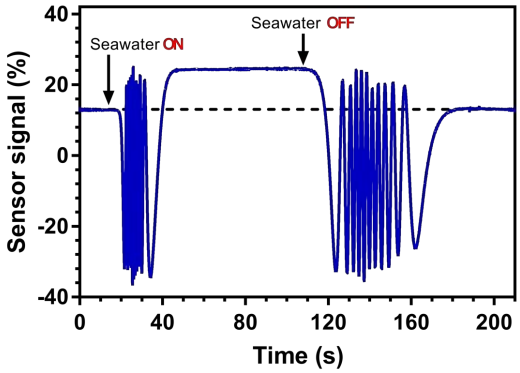

Figure 4.16. Sensor signal response to the flow of seawater.

A competitive calibration curve was obtained with spiked seawater samples ranging from 0 to 100 μg L^{-1} and with the previously optimized conditions. The calibration inhibition curve is represented in Figure 4.14. The IC_{50} and LOD were 66 and 3 ng L^{-1}, respectively, and the DR was from 9 to 478 ng L^{-1}. Remarkably, the LOD was even

as good as some of the reported by chromatographic methods.[112,113,151] The only affected parameter was the reduced DR in sweater due to some matrix effect. Since the absolute signal and sensitivity remained stable, Irgarol 1051 could be directly detected in seawater and no sample pre-treatment was needed. Moreover, the optimized BiMW biosensor was also stable up to 30 different measurements-regeneration cycles with seawater samples (Figure 4.17).

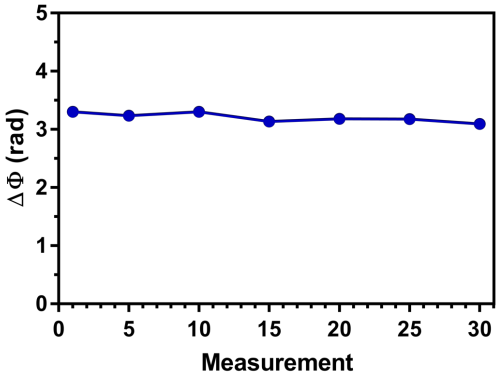

Figure 4.17. Sensor response for 30 consecutive measurement-regeneration cycles with seawater samples of antisera dilution 1:2000 (v/v) regenerated with 50 mM NaOH.

4.7. Analyses of spiked seawater samples

To evaluate the robustness and trueness of the biosensor, several blind spiked seawater samples were analyzed both, with the BiMW biosensor and by a confirmatory method, based on chromatography and mass spectrometry.

For the preparation and fortification of the samples, pristine seawater was taken in the north of the Catalan coast using Pyrex borosilicate glass bottles and filtered with nylon filters (0.45 μm mesh size, Whatman). Aliquots were spiked with different concentrations of Irgarol 1051 in the facilities of the Institute IDAEA-CSIC (Barcelona, Spain). The concentrations of Irgarol 1051 in the blind

samples were unknown during the analysis with the BiMW biosensor.

For the confirmatory method, samples were extracted using a method reported by Gros et al.,[152] with some modifications. Briefly, 500 mL of seawater were acidified with formic acid to pH 2.0 and extracted by SPE using Oasis® HLB cartridges (Waters). After the loading, the cartridges were washed with 5.0 mL ultrapure water, previously adjusted at pH = 2 with formic acid, and eluted with 5.0 mL of methanol. The extracts were evaporated to 100 μL, under a gentle flow of nitrogen, and 900 μL of methanol were added to each vial. The extracts were analyzed by high-performance liquid chromatography coupled to high resolution mass spectrometry with electrospray ionization (HPLC-ESI-HRMS). The chromatographic separation was achieved by reverse-phase chromatography with a C18 column. For each run, 20 μL of extract were injected. The electrospray ionization source worked in positive mode, with the source temperature set at 300 ˚C and a spray voltage of 2.500 kV. Acquisition was carried out in full scan mode with a resolution of 70.000 (full width at half maximum, measured at m/z = 200).

In order to prevent cross contamination and the presence of interferences, all bottles and glass material employed in the analysis were first rinsed with ultrapure water and methanol and heated at 400 ˚C overnight. The samples were stored at - 20 ˚C until their analysis.

Five seawater samples were spiked with 100 μg L^{-1} (far above the sensor limit of linearity), 1.0 μg L^{-1}, 500 ng L^{-1}, 200 ng L^{-1} and 25 ng L^{-1} of Irgarol 1051, respectively. The chromatographic method confirmed, within an error margin of < 10 %, the trueness and stability of the spiked concentrations. This discarded potential losses of Irgarol 1051 due to degradation, sorption or any other miscellaneous factor. Then, the fortified samples were labelled as blind samples and analyzed by the BiMW immunosensor in duplicate after some days.

Overall, a good agreement was obtained between the BiMW immunosensor and the confirmatory method (Table 4.4). The most contaminated sample (#1, $c_{nominal}$ = 100 μg L^{-1}) offered a sensor response far above the limit of linearity (LoL), as expected. All the other samples could be correctly quantified by the biosensor, offering results close to the spiked concentrations.

Table 4.4. Analyses of spiked seawater samples

Sample	$C_{nominal}$ (ng L^{-1})	C_{sensor} (ng L^{-1})	error (%)
#1	10^5	>LoL	N.A.
#2	25	30	16
#3	1000	1177	-18
#4	200	131	34
#5	500	505	-1

LoL: limit of linearity; N.A.: Not Applicable

These results correlated linearly with the concentration of the HPLC-ESI-HRMS analyses, with a Pearson correlation coefficient of r = 0.996 and a p = 0.004, respectively. The slope of the regression line was close to the unit (slope = 1.219 ± 0.081), suggesting a good correspondence between both techniques.

4.8. Conclusions

We have successfully developed a BiMW immunosensor for real-time and label-free detection of Irgarol 1051 directly in seawater. To enhance the analytical features of the assay in terms of sensitivity, stability and reproducibility, special attention has been placed in the assessment and optimization of the functionalization strategy. For that, we have evaluated different silanization protocols and immobilization approaches. The chosen assay is based on a label-free competitive inhibition format with the covalent attachment of an Irgarol 1051 derivative directly to the sensor surface via an aminosilane. This sensor surface is stable up to 30 measure-

regeneration cycles of seawater samples. The developed biosensor shows a LOD and IC_{50} of 3 ng L^{-1} and 66 ng L^{-1} in seawater, respectively, and a DR from 9 to 478 ng L^{-1}. This LOD is well below the 16 ng L^{-1} set by the EU as the maximum allowable concentration. With the optimized immunoassay conditions of the biosensor, the total analysis time takes only 20 min. Finally, and to evaluate the robustness and trueness of the immunosensor, blind seawater samples were analyzed both with the BiMW biosensor and by a confirmatory method based on chromatographic tools. The immunosensor was confirmed to exhibit a satisfactory performance and showed to be a sensitive and straight-forward methodology for the measurement of Irgarol 1051 directly in seawater without any pre-treatment. The current analytical techniques based on chromatographic methods are more time-consuming, less cost-effective and involve the use and waste of significant volumes of environmentally unfriendly organic solvents. The low LOD is as good as some of the reported chromatographic techniques but without the need of clean-up and pre-concentration steps. To our knowledge this is the most sensitive sensor for the detection of Irgarol 1051 directly in seawater that has been presented in the literature.

Chapter 5

Carbon dioxide detection combining metal-organic frameworks as receptors with a bimodal waveguide interferometer sensor

In this chapter, BiMW interferometers were adapted for CO_2 sensing by integrating MOFs as the selective receptor layer onto the Si_3N_4 waveguide sensor surface. This MOF-BiMW sensor was constructed *via* self-assembly of a transparent thin-film of zeolitic imidazolate framework-8 (ZIF-8) nanoparticles onto the waveguides and then adding a protective layer of PDMS. Special attention was given to the development of the gas sensor set-up and to the fine control of the size of the MOF nanoparticles for the construction of high-quality transparent films.

5. Carbon dioxide detection combining metal-organic frameworks as receptors with a bimodal waveguide interferometer sensor

5.1. Introduction

5.1.1. The target analyte: carbon dioxide

Indoor air quality is the air quality that affects the health and quality of life of occupants within and around buildings and structures. Common indoor air pollutants include gases such as CO_2 or CO, VOCs, particulate matter or biological contaminants (e.g. bacteria) that can cause both immediate and long-term health effects. It can be particularly harmful to vulnerable groups with chronic respiratory or cardiovascular diseases. Indoor air quality may have greater impact for many people that outdoor exposure since it has been estimated that humans spend 90 % of their time in both private and public indoor environments.[153]

Carbon dioxide is a known pollutant that affects the performance of humans in workplaces, schools and other indoor areas. High levels of ambient CO_2 can lead to tremors and loss of consciousness (>100000 ppm, 10 %), and even to death (>250000 ppm, 25 %).[154] However, indoors, the pernicious effects of CO_2 begin to appear at much lower levels. For example, CO_2 levels of 2,000 ppm to 5,000 ppm (0.2 % to 0.5 %) lead to headaches, sleepiness, elevated heart rate and diminished concentration, among other negative effects. Organizations such as the Occupational Safety and Health Administration (OSHA), Association Advancing Occupational and Environmental Health (ACGIH) and The National Institute for Occupational Safety and Health (NIOSH) have established CO_2 limits of 0.5 % (8-hour time-weight average), 3 % (short-term exposure) and 4 % (maximum instantaneous limit considered immediately dangerous to life and health).[155] To date, the most common devices on the market for CO_2 detection are non-dispersive infrared and electrochemical sensors. However, they still show some drawbacks including water interferences for the first type of sensors and short

lifespan for the second ones.[156] Therefore, devices for sensing and monitoring indoor CO_2 levels are still urgently needed to ensure the safety of human occupants. Moreover, monitoring of CO_2 is important in many other fields such as food packaging, in which high CO_2 levels (10 % to 80 %) are used to suppress microbial growth.

5.1.2. Metal-Organic Frameworks (MOFs)

Metal-Organic Frameworks (MOFs) are a class of highly porous crystalline solids materials built from metal ions/clusters coordinated to multifunctional organic ligands (Figure 5.1).[157–159] MOFs comprise extended one-, two- or three-dimensional crystalline networks easily synthesized from simple inorganic salts *via* common techniques such as hydro-/solvo-thermal synthesis. The variety of metal coordination geometries and organic ligands translates into a potentially infinite number of structural architectures and compositions. This unique chemical and structural versatility confer them with outstanding porosity[160] as well as tunable pore size and functionality for countless potential applications, including trapping contaminants and/or dangerous gases,[161] catalysis[162] and gas capture and separation.[163,164] Among these research and development areas, sensing is especially prominent, owing to the high porosity of MOFs as well as to their sorption selectivity *via* molecular sieving and chemical specific interactions within the pores.[165]

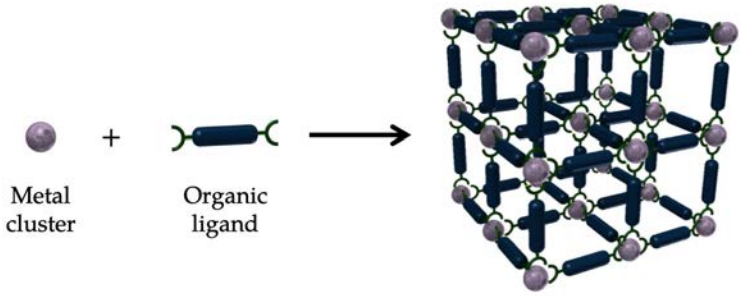

Figure 5.1. Scheme of a Metal-Organic Framework (MOF).

The history of MOFs started more than two decades ago, in 1995, when Yaghi and co-workers reported the hydrothermal

synthesis of an extended network composed of Cu(4,4'-BPY)$_{1.5}$·NO$_3$(H$_2$O)$_{1.25}$ (where BPY is bypiridine).[166] This structure containing large rectangular channels filled with NO_3^- could perform anion exchange with BF_4^- and SO_4^{2-}. These authors demonstrated that channels could be accessible, and the structure was termed Metal-Organic Framework (MOF). Later, in 1999, the same authors synthesized MOF-5, with the formula $Zn_4O(BDC)_3$ (where BDC is benzene-1,4-dicarboxylate).[167] This material was the first 3D robust MOF structure where the guest molecules could be evacuated from the voids demonstrating a Brunauer-Emmett-Teller surface area (S_{BET}) of 2320 $m^2\ g^{-1}$.[168] This surface area outperformed the reported ones for porous materials, including zeolites or carbon-based materials. Nowadays, the highest reported surface area, recently published by Kaskel and co-workers, is for DUT-60, with an experimental S_{BET} of 7839 $m^2\ g^{-1}$ (Figure 5.2).[169]

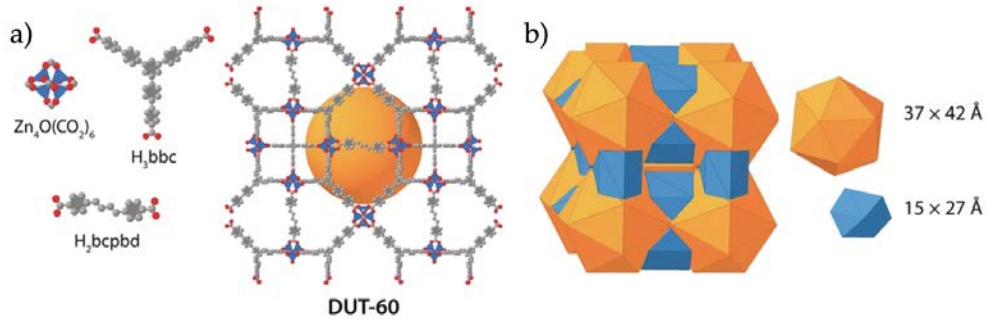

Figure 5.2. DUT-60 framework: (a) Structure of DUT-60 and the metal cluster and organic ligands. (b) The mesopore system of DUT-60 illustrated by orange and blue polygons.[169]

5.1.2.1. MOFs as sensors receptors

There are significant advantages when choosing MOFs over other materials typically used in commercial chemical sensors, such as polymers or semiconductors. The main one is the high surface area to effectively concentrate the adsorbate at higher levels, which can substantially increase the sensitivity of the sensor. Another important characteristic is the selectivity to detect the target molecule *via* size

exclusion from the pore apertures of the MOFs. In 2002, Yaghi and co-workers reported the synthesis of isoreticular MOFs with the topology of MOF-5, the so called IRMOFs (Figure 5.3).[170] Those materials have the same Zn_4O node but substituting the ligand for longer ones, the pore aperture ranged from 3.8 Å up to 28.8 Å. Another source of selectivity is the chemical specific interactions of the target analyte with the internal MOF pore surface. An example is the Zr-DMBD framework (where DMBD is 2,5-dimercapto-1,4-benzenedicarboxylate) with an UiO-66 like topology that has accessible thiol groups from the ligand on the pore surface that effectively adsorb mercury.[171] Another approach is the selective adsorption *via* open metal sites in the MOF that favorably interact with a preferred adsorbent. In 2005, Yaghi and co-workers reported the synthesis of a copper based MOF with open metal sites, named MOF-505, with high sorption capacity for H_2.[172,173] Moreover, most of the guest are physisorbed facilitating the sensor regeneration by simply subjecting the material to vacuum or, if necessary, slightly increasing the temperature. In addition, with a close control on the film thickness and maintaining small size dimensions of the MOFs, the diffusion times can be minimized to increase the sensor response time.

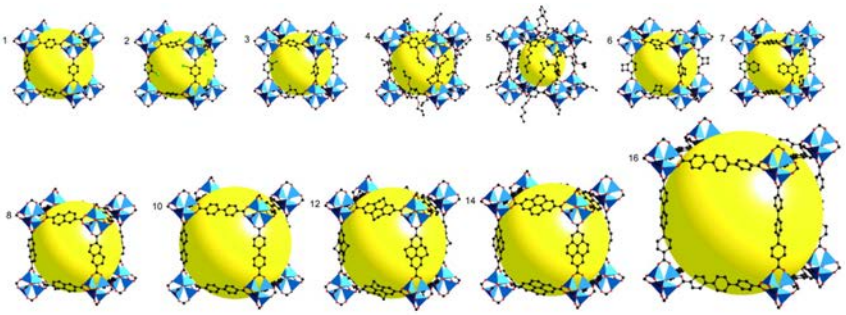

Figure 5.3. Schematic representation showing the isoreticular synthesis of the IRMOFs family with different functionalization of pore walls (top) and the enlargement of the pore size and surface area (down).[170]

One approach for developing MOF-based sensors is the use of luminescent MOFs, in which they are both the receptor and the transducer.[174] However, most of the MOFs used for sensing require a

transducer to convert a chemical response into an electronic signal. The first approach was using MOFs as receptors for developing mechanical sensors. These sensors, which are based in a mass-sensitive response upon analyte uptake included QCMs,[175–177] microcantilevers[178] and SAWs.[179] The reported examples addressed the problems related with selectivity in chemical sensors when using other receptors such as polymers. However, even though these MOF-based sensors showed good sensitivities, they did not achieve the levels reported for other transduction schemes. Another approach has been employing electrical or electrochemical sensors to directly transduce a chemical response into an electronic signal.[180–183] The drawback is that it requires conductive MOFs considerably narrowing the applicability to few reported examples.[184] Photonic transducers, on the other hand, are based on light modulation. Most of them take advantage of refractive index changes but require a fine mesoscopic organization of the MOFs. One of the first approaches was the fabrication of a Fabry-Pérot device with a ZIF-8 film for the detection of vapors.[185] Other examples included the construction of Bragg stacks by alternating high RI metal layers with MOFs layers to behave like 1D photonic crystals.[186] More recently, 2D photonic crystals were fabricated by nanopatterning colloidal ZIF-8 in the form of nanogratings or depositing the ZIF-8 colloids on top of TiO_2 nanogratings to generate a ZIF-8/TiO_2 nanocomposite for the detection of styrene.[187] Other fabricated schemes are 3D photonic crystals by growing MOFs in 3D colloidal structures or by self-assembling polyhedral MOFs for vapor sensing.[188–190] These developed photonic crystals, although are precisely shaped and processed MOFs, present low sensitivities with LODs of 10^{-3} - 10^{-5} RIU.[191] Such low sensitivities only allow detecting vapors instead of gases since the latter produce much smaller RI shifts.

There are few reported MOF-based sensors for the detection for gases. Eddaoudi *et al.* successfully developed a capacitive IDE sensor for H_2S detection,[192] whereas Mirica *et al.* reported the fabrication of an electric sensor for NO detection.[193] For CO_2, Van Duyne *et al.* fabricated a LSPR sensor with an HKUST-1 film that was able to detect CO_2 levels down to 10 %.[194] More recently, Wang *et al.* designed a near-IR fiber-optic coated with HKUST-1 that showed a

LOD of 20 ppm for CO_2.[195] However, practical use of these MOF-based sensors for CO_2 detection is limited by the low hydrolytic stability of HKUST-1 and/or by scattering and water interferences.

5.1.2.2. MOF films

A common characteristic of most of the MOF-sensor schemes is that the fabrication of MOFs as films is required. In fact, the surface growth of MOFs or fine position on different surfaces (e.g. silicon, glass, metals or metal-oxides) is critical to many research fields, such as electronics, sequestration and separation and optics, among many others.[196,197] To date, the fabrication of MOF films has been achieved following different strategies including:

- *In-situ crystallization*: is the direct assembly and growth of MOFs on surfaces immersed in a solution containing the precursors. However, as the bare substrates usually inhibit the growth of the MOFs, this approach requires to first functionalize the substrate or seed the growth with small MOFs crystals.[198,199] Then, the functional groups anchor either the metals or the organic linkers for the nucleation and growth of the surface-attached MOFs, also known as SURMOFs (Figure 5.4a-f). A first example was the selective growth of MOF-5 onto a patterned gold substrate with COOH- terminated SAMs.[200] Also, Fischer and co-workers demonstrated selective and preferential crystal orientation of HKUST-1 and $Zn_2(BDC)_2(DABCO)$ (where DABCO is 1,4-Diazabicyclo[2.2.2]octane) films on alumina and silica modified with COOH-terminated SAMs.[201] Simultaneously, Bein and co-workers demonstrated the preferred and highly oriented crystal growth of HKUST-1 along the [100] direction for COOH-terminated SAMs and the completely different orientation along the [111] direction for the OH-terminated SAMs.[202]

- *Liquid-phase epitaxy (LPE)*: in this approach, a previously functionalized substrate is sequentially immersed in a solution containing the metal precursors and, in a solution, containing the organic ligands precursors with washing steps in between (Figure 5.4g-l). This synthetic method is based in the layer-by-layer (LbL)

technique, and the thickness of the MOF film can be controlled by the number of immersion cycles.[203] This technique allows the fabrication of ultrathin and smooth SURMOFs. More recently, alternative techniques for a large-scale fabrication and/or closer control in the MOF film characteristics have been developed such as high-throughput spray,[204] spin-coating[205] and a dipping robot.[206]

- *Powder MOF-based deposition*: this method requires to first synthesize the MOF powder and subsequently deposit it onto the surface. The simplest approach is to first obtain the MOF nanoparticles from a standard solvothermal synthesis followed by a drop-casting deposition.[181] For a closer control on the film thickness and density, the spin-coating technique has also been employed allowing a fast, simple, low cost and large surface area processing at industry level.[207–209] Another approach for the controlled thickness of the MOF film is the dip-coating method; as demonstrated, for example, for MIL-100 (Al,Cr,Fe)[210] and Cr-MIL-101.[211] For the long-term and permanent attachment of the MOF, the MOF powder can be first mixed with a polymeric binder to obtain a mixed matrix membrane (MMM).[212,213]

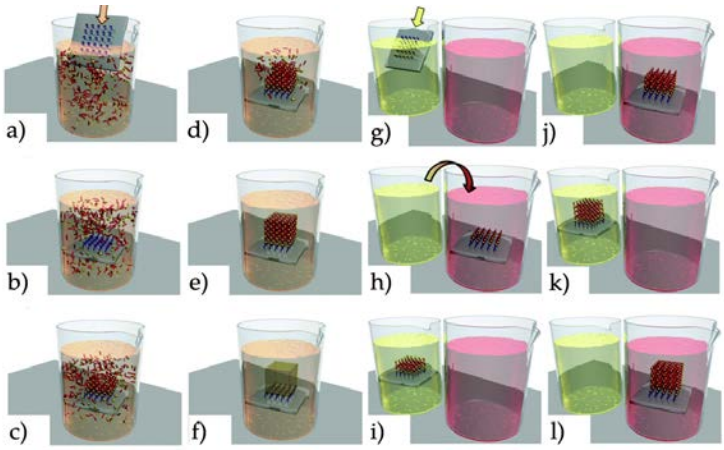

Figure 5.4. (a–f) Schematic of the growth of the *in-situ crystallization* of MOFs on a patterned SAM surface. The patterned SAM substrate is placed in a solution containing both metal precursor and organic linker, resulting in the controlled formation of MOF crystals on the SAM pattern. (g–l) Schematic of the LbL growth of MOFs on a patterned SAM surface.[196]

There are other well studied methods for the fabrication of MOF films. The Langmuir-Blodgett (LB) method is the formation of MOFs monolayers that are sequentially transferred onto a substrate. The first example was the synthesis of 2D layered NAFS-1 sheets formed on the solution surface, and then compressed by the container walls from the air-water interface. 3D MOFs films can be obtained via sequential LbL growth process and the weak interactions (π stacking and van der Waals interactions) between the monolayers.[214] Other methods include electrochemically deposited MOF thin films[215] and chemical vapor deposition (CVD).[216]

In this Thesis, both the choice of the appropriate MOF and the preparation of the MOF film, were crucial for the development of our MOF-BiMW sensor.

5.2. Materials and methods

5.2.1. Reagents and materials

All chemical reagents and solvents were purchased from Sigma Aldrich and used as received without further purification. Milli-Q water from Millipore (USA) was always employed.

5.2.2. Synthesis of nanoZIF-8 (size = 32 ± 5 nm)

The synthesis of the colloidal solution followed a slightly modified protocol previously reported by Cravillon *et al.*[217] $Zn(NO_3)_2{\cdot}6H_2O$ (1.47 g, 4.94 mmol) dissolved in 100 mL of methanol was added into 2-methylimidazole (3.24 g, 39.46 mmol) dissolved in 100 mL of methanol. The resulting mixture was then gently stirred for a few seconds at RT. Note that this mixture turned turbid after some seconds. After 7 min, the nanoparticles were separated from the dispersion by centrifugation at 11000 rpm for 10 min in 50 mL Falcon tubes. The pellets were then re-dispersed in 5 mL of methanol and centrifuged in 4 Eppendorf tubes at 18000 rpm for 15 min. The nanoZIF-8 particles were washed again with 2 mL of methanol and centrifuged in 2 Eppendorf tubes at 18000 rpm for 15 min. The collected wet pellets were finally resuspended at a concentration of

100 mg mL^{-1} in Milli-Q water with cetyl trimethylammonium bromide (CTAB) dissolved. Note that the particles should be dispersed while they are still wet to prevent aggregation.

5.2.3. Synthesis of ZIF-8 (size = 53 ± 8 nm)

$Zn(NO_3)_2 \cdot 6H_2O$ (2.00 g, 6.72 mmol) dissolved in 100 mL of methanol was added into 2-methylimidazole (3.24 g, 39.46 mmol) dissolved in 100 mL of methanol. The resulting mixture was gentle stirred for a few seconds at RT. Note that the mixture turned turbid after several seconds. After 2 h, the nanoparticles were separated from the dispersion by centrifugation at 11000 rpm for 10 min in 50 mL Falcon tubes. The pellets were then redispersed in 5 mL of methanol and centrifuged in 4 Eppendorf tubes at 18000 rpm for 15 min. The ZIF-8 particles were washed again with 2 mL of methanol and centrifuged in 2 Eppendorf tubes at 18000 rpm for 15 min. The collected wet pellets were finally resuspended at a concentration of 100 mg mL^{-1} in Milli-Q water with CTAB dissolved. Note that the particles should be dispersed while they are still wet to prevent aggregation.

5.2.4. Synthesis of ZIF-8 (size = 70 ± 12 nm)

$Zn(NO_3)_2 \cdot 6H_2O$ (3.00 g, 10.08 mmol) dissolved in 100 mL of methanol was added into 2-methylimidazole (6.00 g, 73.08 mmol) dissolved in 100 mL of methanol. The resulting mixture was gentle stirred for a few seconds at RT. Note that this mixture turned turbid after several seconds. After 2 h, the nanoparticles were separated from the dispersion by centrifugation at 11000 rpm for 10 min in 50 mL Falcon tubes. The pellets were then redispersed in 5 mL of methanol and centrifuged in 4 Eppendorf tubes at 18000 rpm for 15 min. The ZIF-8 particles were washed again with 2 mL of methanol and centrifuged in 2 Eppendorf tubes at 18000 rpm for 15 min. The collected wet pellets were finally resuspended at a concentration of 100 mg mL^{-1} in Milli-Q water with CTAB dissolved. Note that the particles should be dispersed while they are still wet to prevent aggregation.

5.2.5. NanoZIF-8 film formation and optimization

First, the sensor chips were cleaned/recycled as previously explained. Then, a high optical quality nanoZIF-8 film was prepared using the spin-coating technique with a Laurell WS-650-23 spin coater (Laurell Technologies, PA, USA). To this end, the colloidal solution of nanoZIF-8 was spin-coated with an acceleration of 250 revolutions per minute (rpm) s^{-1} and 1 min at RT under ambient atmospheric conditions. For the optimal film thickness, different concentrations and spinning speeds were evaluated. First, 200 µL from 10 mg mL^{-1} to 120 mg mL^{-1} of the nanoZIF-8 were deposited in each sensor chip and then rotated at a spinning speed of 2000 rpm. The optimal film thickness was evaluated measuring the sensor response of 100 % CO_2 for each sensor chip. The highest signal response was achieved for 60 mg mL^{-1}. With that concentration, films were prepared at different spinning speeds from 2000 rpm to 6000 rpm. The highest signal response was achieved for 2000 rpm, which corresponds a film thickness of 1.15 µm ± 0.05 µm (evaluated with transversal cross-section of FE-SEM images).

5.2.6. PDMS film formation

PDMS pre-polymer and curing agent (SYLGARD 184 Silicone Elastomer Kit, Dow Corning, USA) were thoroughly mixed in a 10:1 weight ratio. A stock solution of 20 % (w/w) PDMS was prepared by dissolving the elastomer in toluene and stirred for 12 h. 200 µL of PDMS solution was deposited on top of the nanoZIF-8 film or directly onto the BiMW sensor area, and then rotated at a spinning speed of 5000 rpm and an acceleration of 250 rpm s^{-1} for 1 min. The coated films were subsequently cured in a hot-plate at 110 ˚C for 12 h.

5.2.7. Mixed matrix membrane of nanoZIF-8/PDMS film

PDMS pre-polymer and curing agent (SYLGARD 184 Silicone Elastomer Kit, Dow Corning, USA) were thoroughly mixed in a 10:1 weight ratio. A stock solution of 20 % (w/w) PDMS was prepared by dissolving the elastomer in THF and stirred for 12 h. NanoZIF-8 dispersed in THF is added to a solution ending with a 20% (w/w)

concentration following the procedure reported by Fang et.al.[218] 200 μL of ZIF-8/PDMS solution was deposited on top of the BiMW sensor and then rotated at a spinning speed of 5000 rpm and an acceleration of 250 rpm s^{-1} for 1 min. The coated films were subsequently cured in a hot-plate at 80 ˚C for 12 h.

5.2.8. Characterization

X-ray powder diffraction (XRPD) patterns of ZIF-8 samples were collected on an X'Pert PRO MPDP analytical diffractometer (Panalytical) at 45 kV, 40 mA using Cu Kα radiation (λ = 1.5419 Å), whereas XRD patterns of the ZIF-8 films were collected on an X'Pert PRO MRD analytical diffractometer (Panalytical) equipped with a parabolic mirror at 45 kV, 40 mA using Cu Kα radiation (λ = 1.5419 Å). FE-SEM images were collected on a FEI Magellan 400L scanning electron microscope at an acceleration voltage of 2.0 kV and FEI Quanta 650F scanning electron microscope with EDX Inca 250 SSD XMax20, using aluminum as support. The size of nanoZIF-8 particles was calculated from FE-SEM images by averaging the size of 200 particles measured using ImageJ software from images of different areas of the same samples. Ellipsometry measurements were made on a GES5E rotating polarizer ellipsometer (SOPRALAB). Volumetric N_2 and CO_2 sorption isotherm was collected at 77 K, 278 K and 293 K respectively using an AutosorbIQ-AG analyzer (Quantachrome Instruments) after outgassing the powder at 85 °C under primary vacuum. Vis absorption spectra were recorded on a Cary 4000 UV-Vis spectrophotometer (Agilent Technologies, Santa Clara, CA, USA) using the ZIF-8 nanoparticles films deposited on glass substrates. The thicknesses of the different films were characterized with the transversal cross-section of FE-SEM images.

5.3. Fabrication and optical characterization of MOF films

The main objectives for this second application of the Thesis were the integration, for the first time, of MOFs onto interferometric transducers and the detection of CO_2 gas. In this section, we

summarize some of the preliminary work done in order to select the most appropriate MOF as receptor for integration with the BiMW sensor.

The ideal MOF needed-to-meet the following conditions: (i) specificity for the target analyte; (ii) transparency in the visible spectrum; (iii) permanent attachment of the MOF film allowing consecutive measurements and without affecting the sensor response; and (iv) a thickness close to the EW penetration depth to enhance the sensitivity. Preliminary studies showed that the main challenge when working with MOFs in waveguide based sensor devices is the strong optical scattering of the MOF film, consequently inhibiting light propagation through the sensor waveguide.[195]

In order to investigate the possibility to integrate MOFs onto the BiMW transducers, we studied the optical characteristics of the well-known zeolitic imidazole framework-8 (ZIF-8).[219] The structure of ZIF-8 is a porous sodalite-type MOF made of Zn(II) ions and 2-methylimidazolate linkers (Figure 5.5). It exhibits a good thermal stability and a large surface area (≈ 1200 m^2 g^{-1} to 1500 m^2 g^{-1}) with pore diameters of 11 Å connected via hexagonal apertures of 3.4 Å. It was selected because is transparent in the visible spectrum, stable under high relative-humidity conditions and is suitable for gas separation, since it is selective for CO_2 and H_2 over N_2, O_2 or CH_4.[219,220] To study the MOF film transparency, different ZIF-8 nanoparticles below 100 nm size were synthesized (see Figure 5.6).

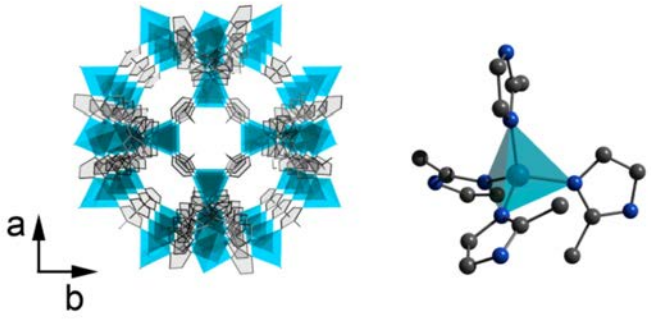

Figure 5.5. Representation of the structure of ZIF-8.

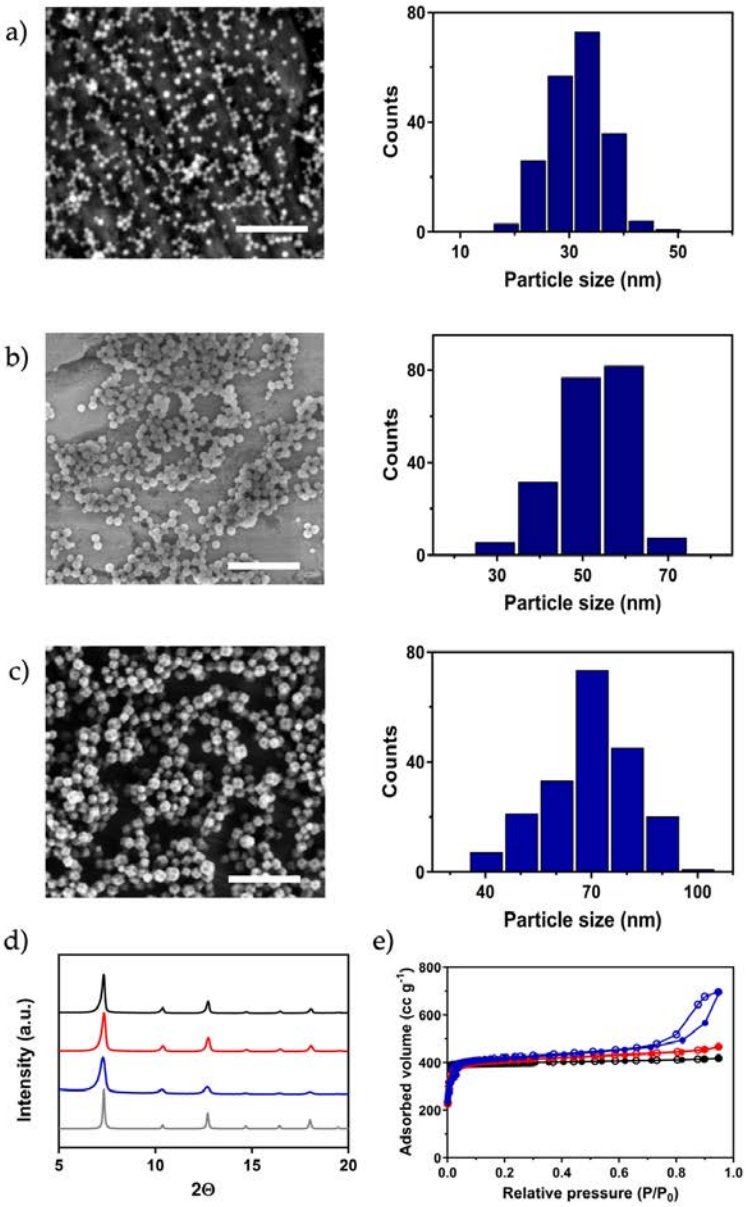

Figure 5.6. (a) Representative FE-SEM image of nanoZIF-8 (size = 32 ± 5 nm) and corresponding size-distribution histogram. (b) Representative FE-SEM image of ZIF-8 (size = 53 ± 8 nm) and corresponding size-distribution histogram. (c) Representative FE-SEM image of ZIF-8 (size = 70 ± 12 nm) and corresponding size-distribution histogram. (d) Simulated (grey) and experimental XRPD patterns of ZIF-8 nanoparticles with a size of 32 ± 5 nm (blue), 53 ± 8 nm (red) and 70 ± 12 nm (black). (e) N_2 sorption isotherm at 77 K of CTAB-coated ZIF-8 nanoparticles with a size of 32 ± 5 nm (blue), 53 ± 8 nm (red) and 70 ± 12 nm (black). Respective BET surface areas: 1488, 1480 and 1471 $m^2 g^{-1}$ (theo-expected = 1300-1500 $m^2 g^{-1}$). Scale bars: 500 nm.

The highly packed films were constructed via self-assembly of the ZIF-8 nanoparticles using the surfactant cetyl trimethylammonium bromide (CTAB).[189] To construct the MOF films, we used the spin-coater to deposit the aqueous colloidal solutions of CTAB-coated ZIF-8 nanoparticles (spinning speed: 5000 rpm; time: 1 min; acceleration: 250 rpm s^{-1}). This approach is not only fast, simple and cheap but also allows a fine control of the film thickness in large surface areas processing at industry level.[207–209] The resulting CTAB-coated ZIF-8 films show different visible transmission spectra depending on the particle size (see Figure 5.7).

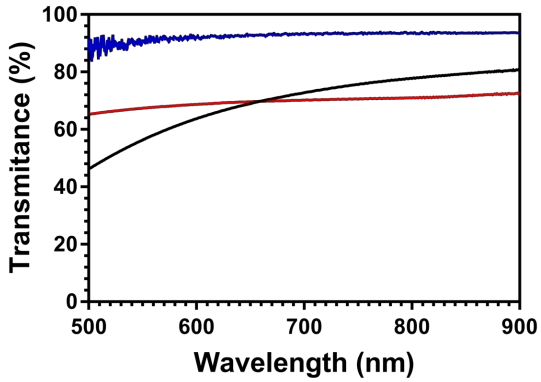

Figure 5.7. Visible transmission spectra of the films made of the self-assembly of CTAB-coated ZIF-8 particles with a size of 32 ± 5 nm (blue), 53 ± 8 nm (red) and 70 ± 12 nm (black).

The film fabricated by the self-assembly of CTAB-coated nanoZIF-8 particles with a size of 32 ± 5 nm, hereafter named nanoZIF-8, showed a transmittance greater than 90 % at the BiMW operating wavelength (660 nm, Figure 5.7). Note that the small nanoparticle size was crucial for the film transparency; indeed, use of larger particles (size: 53 nm ± 8 nm, or 70 nm ± 12 nm) produced translucent films with a transmittance at 660 nm of 70 % (Figure 5.7). In these films, the scattering of the light through the waveguide inhibited any sensing. With the transparent nanoZIF-8 films (Figure 5.8) light efficiently transmitted through the waveguide. Moreover,

the refractive index (n ≈ 1.1 – 1.2) of the nanoZIF-8 film, as determined by ellipsometry, allows the light propagation through the waveguide and the generation of only the fundamental and the first order mode. Thus, the chosen MOF for integration onto the BiMW was the transparent nanoZIF-8 film.

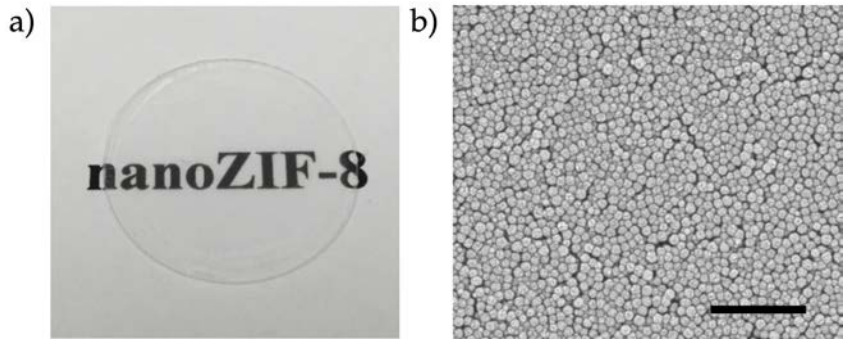

Figure 5.8. (a) Photo of the transparent film of self-assembled ZIF-8 nanoparticles. (b) SEM image of a self-assembled nanoZIF-8 film. Scale bar: 500 nm.

5.4. Design of the experimental gas sensor set-up

As it has been stated, the BiMW sensor is a device exhibiting an unprecedent sensitivity for label-free detection. However, this device had only been applied for fluid media sensing. Therefore, we had to design a gas sensor set-up for handling gases (Figure 5.9).

As a first step, we designed a gas handling system able to be adapted to the BiMW experimental set-up. In this gas handling system, all the tubing lines were made of ¼'' stainless-steel or flexible Teflon tubing that are impermeable to gases. A crucial step was the design of a gas cell to house the sample in contact with the sensing window of the BiMW sensor chip. The chamber was designed in stainless-steel. This new gas cell included an O-ring interfaced with the BiMW sensor surface to inject the gas to the sensing window during experiments isolated from the air. Different flow rates were delivered using 3 different Mass Flow Controllers (MFCs) (10 mLn or

0.7 mLn EL-FLOW Bronkhorst®) to control the flow rate for each gas (N_2, CO_2 and CH_4) and, therefore, the concentration of the gases employed for the analysis. The MFCs were also needed to control the pressure inside the gas chamber. Gases are highly compressible and this is critical because the RI of a material is proportional to its density. High flow rates lead to pressures above the atmospheric pressure (> 1 atm) increasing the RI and, therefore, the sensor will measure higher signal shifts than the real value due to the gas sample. In light of this, a Back-Pressure Controller (BKP, 0.2 – 1100 mbar, Bronkhorst®) was added at the exit to control the pressure of the gas cell and connected to a Pfeiffer DUO vacuum pump to assure that the evaluations were always carried at atmospheric pressure. Additional instrumentations in the handling system included a static mixer installed upstream of the gas cell for the homogeneous injection of CO_2 and/or CH_4 gases in dry N_2 flowed. Finally, a direct-acting solenoid valves were installed downstream to exit the gases from a buildup of pressure. For the gas dosing, ultra-high purity grade N_2, CO_2 and CH_4 (Praxiar Premium) were used for all experiments. All measurements were performed in triplicate and prior to each triplicate the gas cell was left under vacuum and/or then purged with N_2 flux.

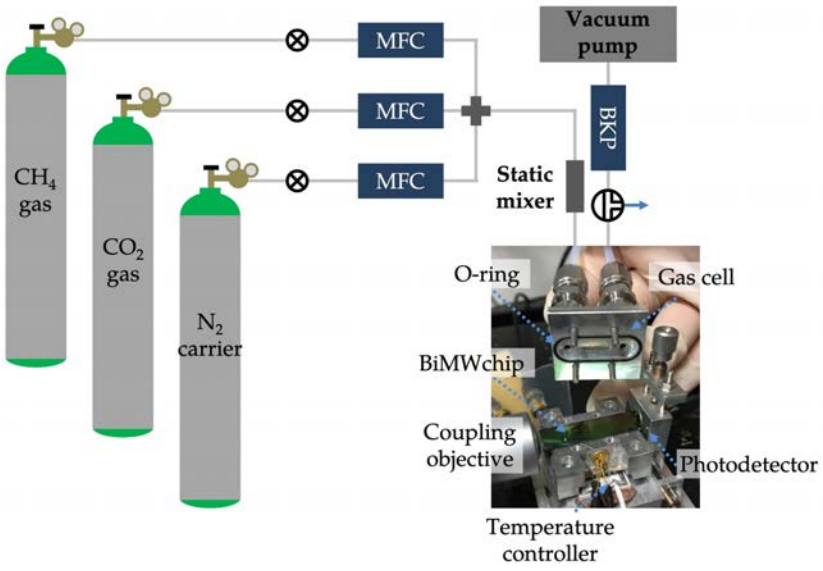

Figure 5.9. Gas system for the controlled mixture of different gases. Photograph of the gas sensing cell with the O-ring on top of the sensor chip and the Peltier element behind.

5.5. Integration of the nanoZIF-8 films onto the transducer

In EW-based sensors the receptor layer thickness is essential to maximize the sensitivity. As previously explained, the evanescent field of the transmitted light decays exponentially as it penetrates the outer medium, so closer to the sensor surface the receptor is, more sensitive the sensor. Therefore, an optimum thickness for the nanoZIF-8 film onto the BiMW surface was sought (Figure 5.10a).

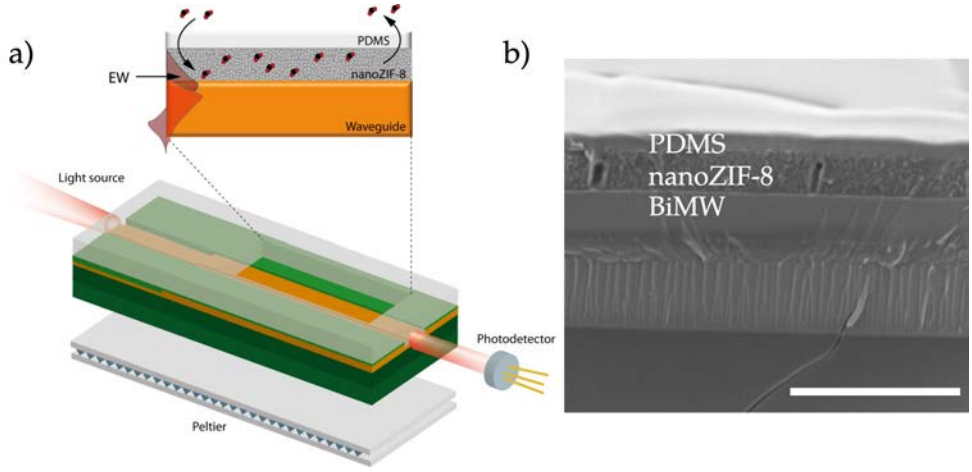

Figure 5.10. (a) Schematic of the nanoZIF-8-based BiMW sensor. (b) FE-SEM image (side view) of the nanoZIF-8-based BiMW sensor, showing the layers of nanoZIF-8 and PDMS built on top of the sensor waveguide. Scale bar: 5 μm.

The spin-coating technique allows a fine control of the film thickness. To experimentally determine the optimum receptor layer thickness, we compared the sensor signal response with different nanoZIF-8 thicknesses under different spin-coating conditions. Considering that most of the waveguide systems have a penetration depth of 0.1 - 1 μm, we evaluated nanoZIF-8 films within this range. We prepared the MOF film varying the initial concentration of nanoZIF-8 (Figure 5.11a). At first, increasing the film thickness enhanced the sensitivity. This was probably caused because the EW

penetration depth is larger. But above 1,15 ± 0,05 μm film thickness the sensor response decreased. Receptor layers thicker than the EW affects the diffusivity of the gas molecules to the sensor surface and therefore decreases the sensitivity (Figure 5.11a). On the other hand, parameters such as time or the spin-coater speed did not significantly affect the sensor sensitivity (Figure 5.11b). The most sensitive nanoZIF-8 film was 1.15 ± 0.05 μm thick (Figure 5.10b), as prepared by spin-coating (concentration: 60 mg nanoZIF-8 mL^{-1}; spinning speed: 2000 rpm; time: 1 min; acceleration: 250 rpm s^{-1}). This optimized value fits well into the EW penetration depth, thus enabling the maximum amount of nanoZIF-8 to sense CO_2.

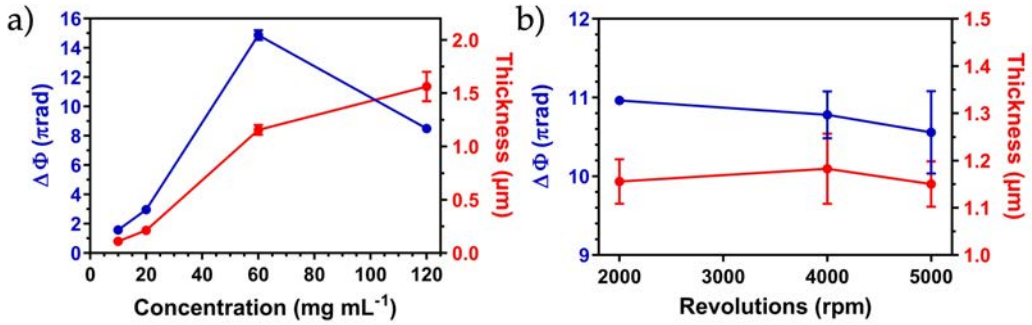

Figure 5.11. (a) Responses to 100 % CO_2 (blue) of nanoZIF-8-based BiMW sensors made of different nanoZIF-8 films, which thickness (red) has been tuned by spin-coating (spinning speed: 2000 rpm; time: 1 min; acceleration: 250 rpm s^{-1}) nanoZIF-8 colloids of different concentrations. (b) Responses to 100 % CO_2 (blue) of nanoZIF-8-based BiMW sensors made of different nanoZIF-8 films, which thickness (red) has been tuned by spin-coating a nanoZIF-8 colloid (concentration: 60 mg mL^{-1}; time: 1 min; acceleration: 250 rpm s^{-1}) at different spinning speeds from 2000 rpm to 6000 rpm.

Then, we deposited a PDMS layer on top of the nanoZIF-8 film via spin-coating. The layer of PDMS had different aims: (i) protect the optimized nanoZIF-8 film from the environment; (ii) permanent attachment of the nanoZIF-8 film onto the sensor waveguide; and (iii) prevent cracking of the film upon its activation (i.e. upon removal of the guest molecules in its pores). Earlier experiments showed that this crack-prevention step was crucial (Figure 5.12). For the activation of the nanoZIF-8, the film was led at 60 ˚C under vacuum overnight. This

exposure cracked the nanoZIF-8 film causing a complete loss of light transmission through the sensor waveguide. Note that the deposition of PDMS later did not recover the light transmission. The rubbery polymer PDMS was chosen because is highly permeable to CO_2, enabling diffusion of CO_2 towards the nanoZIF-8 film.[221] We also tested other polymers, including the highest reported polymer permeable to CO_2, poly(1-trimethylsilyl-1-propyne) (PTMSP).[222] In this last case, the resulting polymer film did not prevented the cracking of the underlying nanoZIF-8 film. A plausible reason is the glassy character of PTMSP.

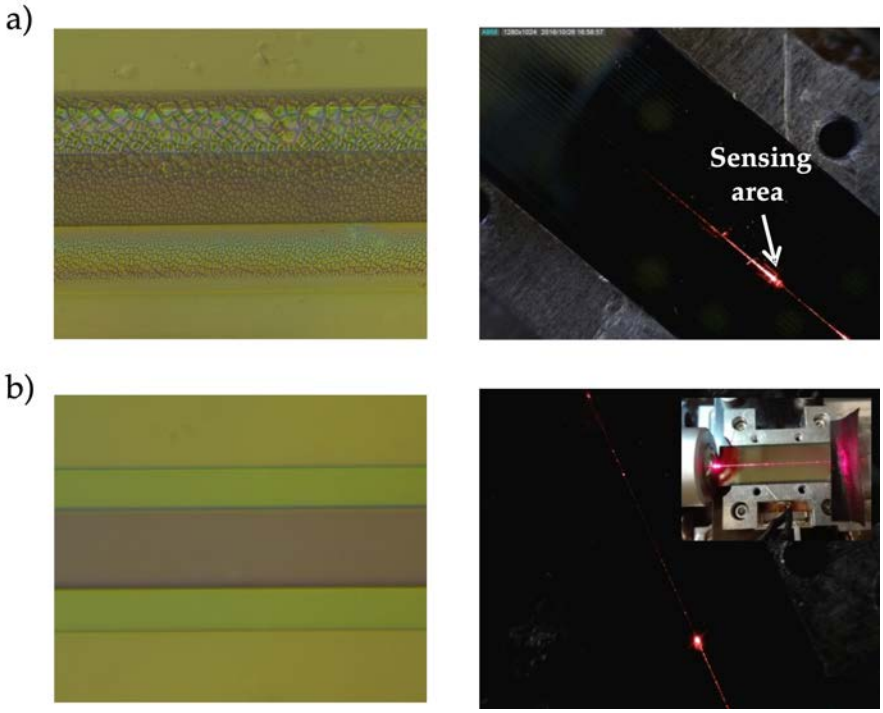

Figure 5.12. (a) Optical image of a bimodal waveguide sensor showing the cracking of the CTAB-coated nanoZIF-8 film after nanoZIF-8 is activated (left). Optical scattering image of a sensor chip when the light from a 660 nm red laser source is coupled in a bimodal waveguide, showing the complete loss of light transmission through the waveguide (right). (b) Optical image of a bimodal waveguide sensor with a first layer of activated CTAB-coated nanoZIF-8 and a second layer on top of PDMS, showing the absence of cracking once nanoZIF-8 is activated (left). Optical scattering image of a sensor chip when the light from a 660 nm laser source is coupled in a bimodal waveguide, showing the light transmission through the waveguide (right).

The PDMS layer had to be as thin as possible to enhance the diffusivity of CO_2. Therefore, PDMS pre-polymer and curing agent were first dissolved in toluene to decrease the viscosity of the mixture. Different spinning-speeds and dilution factors of the elastomer and toluene were evaluated (Table 5.1). A homogeneous PDMS layer could be minimized down to 0.66 ± 0.17 µm by spin-coating (spinning speed: 5000 rpm; time: 1 min; acceleration: 250 rpm s^{-1}) a solution of PDMS in toluene at a concentration of 20 % w/w (Figure 5.10b). After, the coated film was subsequently cured in a hot-plate at 110 ˚C for 12 h. At higher spinning speeds and increased toluene dilution factors, the PDMS layer did not deposit.

Table 5.1. PDMS film thicknesses tuned by spin-coating (time: 1 min; acceleration: 250 rpm s^{-1}) at different spinning speeds and toluene dilutions.

Spinning speed (rpm)	Toluene dilution (1:x)	Thickness (μm)
10000	10	--
1000	10	--
1000	5	--
10000	4	--
5000	4	0,69 ± 0,17
10000	2	1,5 ± 0,1
5000	2	4,1 ± 2,9
10000	--	7,4 ± 0,2
5000	--	8.4 ± 1.8

We finally activated the nanoZIF-8 on the BiMW sensor *in-situ* (directly in the gas sensor set-up) by heating it at 60 ˚C under vacuum overnight. As explained earlier, the sensor set-up has a Peltier element at the bottom of the platform for temperature control and is equipped with a vacuum pump at the exit of the gas delivery system (Figure 5.9 and Figure 5.10a).

5.6. Analytical performance of the MOF-BiMW gas sensor

Since this was the first time that the BiMW transducer was employed for sensing, we first evaluated the capability of the BiMW sensor to detect gases with the bare chip. The result is represented in Figure 5.13. Initially, the bare chip was exposed to the carrier gas N_2 alone until the sensor signal response when CO_2 reaches the sensing area. After, we observed the same sensor response when we switched back to the flow of N_2. The RI of N_2 and CO_2 are n = 1.0002984 and n = 1.0004489, respectively. We could confirm that a RI change of $1.5 \cdot 10^{-4}$ RIU was easily detected with the BiMW sensor alone.

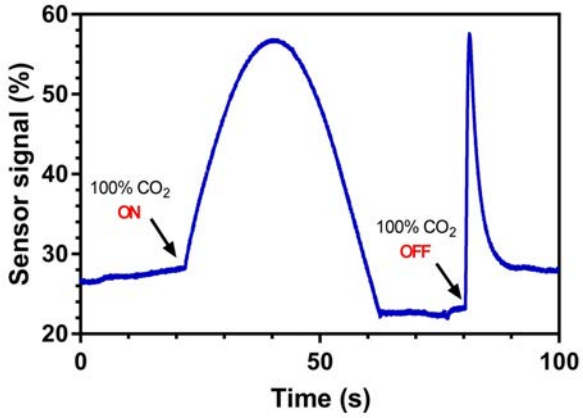

Figure 5.13. Real-time response signal to the change from pure N_2 flow to pure CO_2 flow at RT of the bare BiMW sensor.

Then, we wanted to confirm the enhanced sensitivity when using a MOF film as receptor with the BiMW sensor. For that, we compared the absolute signal ($\Delta\phi$) for CO_2 detection of the nanoZIF-8 based BiMW sensor with the respective responses obtained for: (i) a bare BiMW sensor in the absence of nanoZIF-8 and PDMS; (ii) a BiMW sensor containing only the PDMS film; and (iii) a BiMW sensor coated with a MMM of nanoZIF-8 embedded into the PDMS (Figure 5.14).

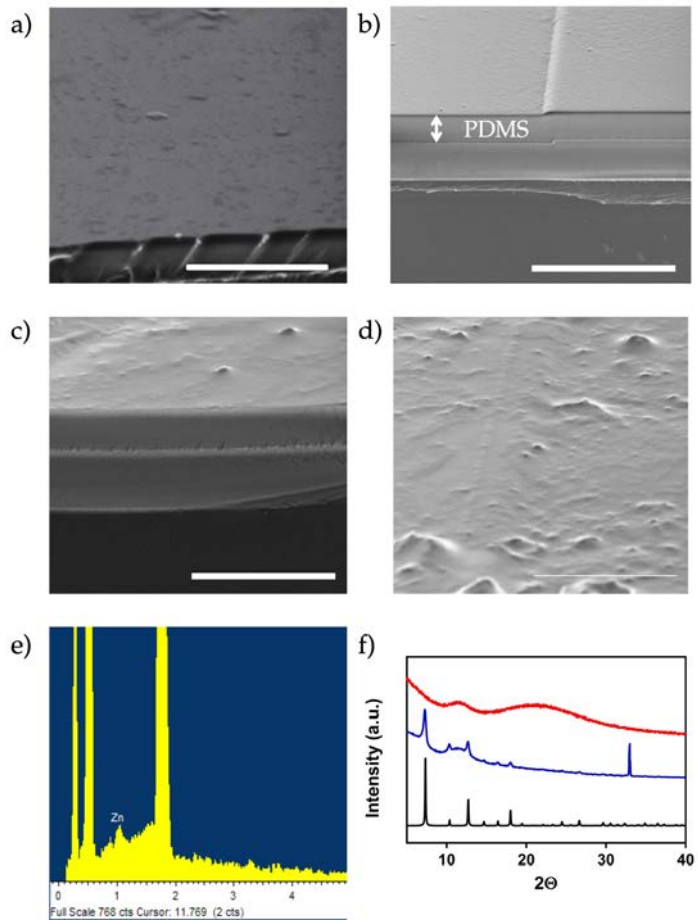

Figure 5.14. (a) FE-SEM image of a bare chip. (b) FE-SEM image of a BiMW sensor containing only the PDMS film. (c and d) FE-SEM image (left) and SEM image (right) of a BiMW coated with nanoZIF-8 embedded in PDMS. (e) EDX analysis of the nanoZIF-8 embedded in PDMS. (f) XRD pattern of the nanoZIF-8 embedded in PDMS (blue), as compared to the ZIF-8 powder pattern (black) and PDMS (red). Scale bar: 5 μm.

The response for each sensor was the change from the flow of the carrier gas N_2 to the flow of pure CO_2 at RT (293 K) (Figure 5.15a). We could confirm that the highest sensor response in terms of absolute signal was for the nanoZIF-8-based BiMW sensor ($\Delta\phi$ = 14,87 ± 0,34 πrad) (Figure 5.15b). This absolute signal was ~ 24-fold amplified when pre-concentrating the CO_2 within the pores of the nanoZIF-8 compared to the bare sensor chip. When coating the film with a PDMS layer or a MMM film of PDMS/nanoZIF-8, the absolute

signal was ~ 4-fold amplified. This last result confirms the need to work with the layer of nanoZIF-8 underneath the PDMS. When mixing the nanoZIF-8 with the PDMS, we decreased the number of available receptors in close contact with the sensor surface and, therefore, the sensitivity.

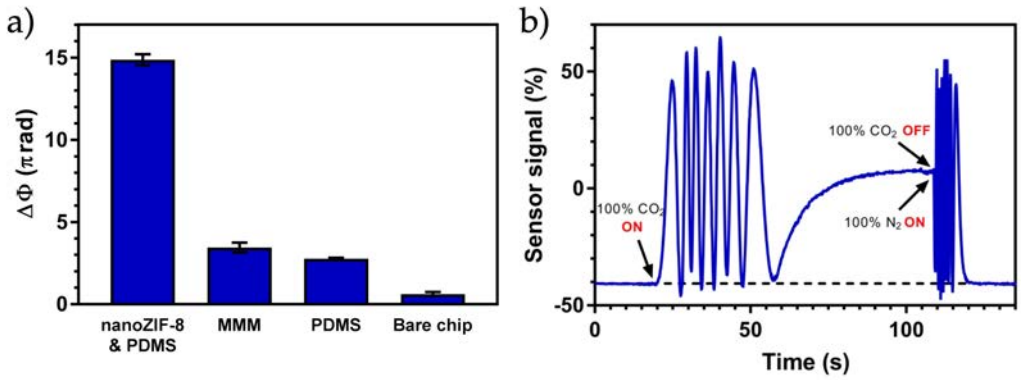

Figure 5.15. (a) Responses to 100 % CO_2 of the nanoZIF-8-based BiMW sensor, the BiMW sensor coated with a MMM of PDMS/ZIF-8, the BiMW sensor containing only the PDMS film and the bare BiMW sensor. (b) Real-time response signal to the change from pure N_2 flow to pure CO_2 flow at RT of the nanoZIF-8-based BiMW sensor.

Using the optimized conditions established before for our nanoZIF-8-based BiMW sensor, the sensor response was evaluated for different concentrations of CO_2 established by variably mixing the CO_2 flow with the carrier N_2 flow at RT (Figure 5.16). The calibration curve with triplicate measurements for each CO_2 concentration is shown in Figure 5.17. From here, we deduce a linear response in the range of 1 % to 100 % CO_2. The LOD was 3130 ppm of CO_2 calculated as the concentration corresponding to the blank signal plus three times its SD.

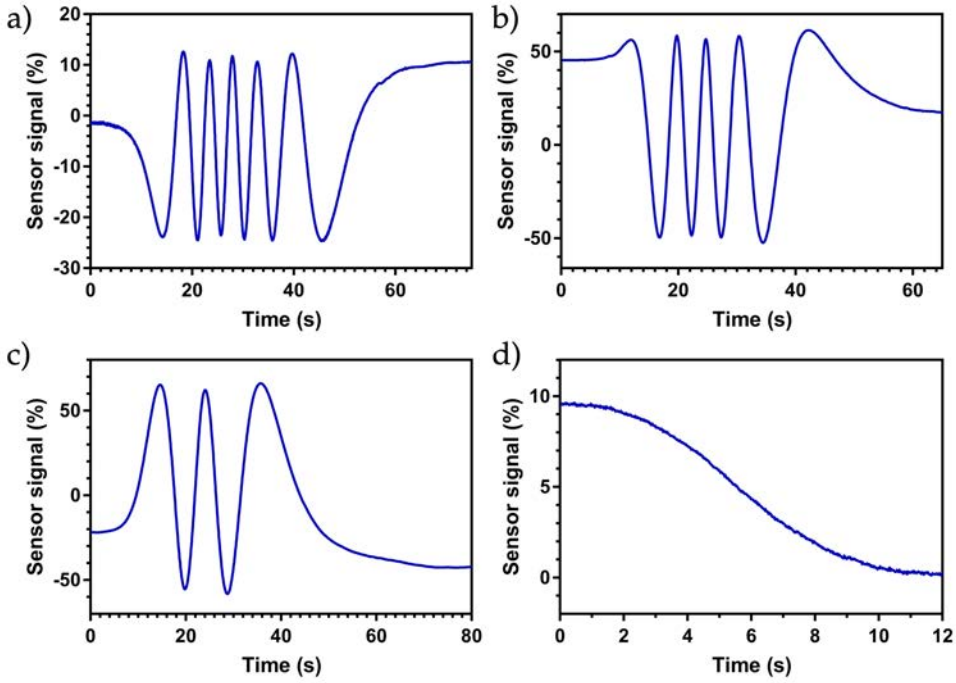

Figure 5.16. Real-time signals for the detection of (a) 80 % CO_2, (b) 60 % CO_2, (c) 40 % CO_2 and (d) 1 % CO_2 at RT.

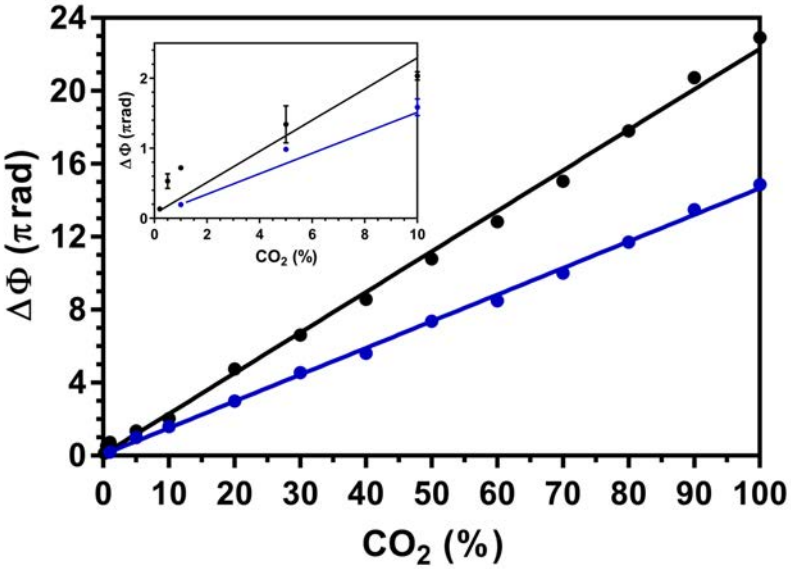

Figure 5.17. Calibration curves at 293 K (blue) and 278 K (black) for CO_2.

The extent to which a gas can adsorb to a MOF surface depends on the temperature and pressure of the gas. To study the temperature dependence of the nanoZIF-8, we measured the absolute signal to a change from pure N_2 flow to pure CO_2 flow as the temperature decreased from RT to 278 K (Figure 5.18a). These results confirm previous reports that showed greater CO_2 uptake and CO_2 selectivity (over N_2) of ZIF-8 at lower temperatures (Figure 5.18b).[223] We then repeated the calibration curve experiment but decreasing the temperature down to 278 K using the Peltier element (Figure 5.17). Results show a ~ 1.5-fold amplification of the CO_2 signal response at 100 % CO_2 relative to that measured at RT and a linear response in the range of 0.2 % to 100 % CO_2. By simply decreasing the working temperature to 278 K, the LOD could be lowered down to 774 ppm.

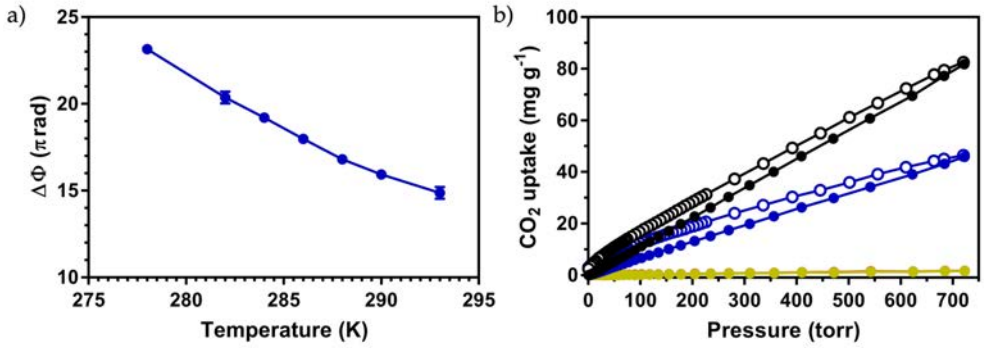

Figure 5.18. (a) Responses to 100 % CO_2 of the nanoZIF-8-based BiMW sensor at different temperatures, from RT to 278 K. (b) Adsorption isotherms of nanoZIF-8 by using CO_2 at 278 K (black), CO_2 at 293 K (blue), N_2 at 278 K (yellow), and N_2 at 293 K (red).

Next, we needed to address the analytical features of the nanoZIF-8-based BiMW sensor in terms of selectivity, reusability, reproducibility and repeatability. When using MOFs as receptors, we do not only seek enhanced sensitivity but also selectivity for the target analyte. Most of the literature does not report the selectivity when using MOF as receptors in chemical sensors. Here, we evaluated the ZIF-8 selectivity for CO_2 over N_2 or CH_4. For that, we measured the sensor response from vacuum up to 1 bar of pressure for these three

gases at RT. The selectivity reached up to 8:1 for CO_2 over N_2, and up to 3:1 for CO_2 over CH_4 (Figure 5.19a). The preferred selectivity for CO_2 over CH_4 was confirmed by measuring CO_2 in the presence of 1 % CH_4. These methane concentration is well above the 0.1 % concentration recommended by NIOSH as the maximum concentration for an 8-hour work.[224] Under these conditions, the signal response was identical than in the absence of CH_4 (Figure 5.19b). The sensitivity of the sensor to CH_4 was also tested measuring in triplicate different CH_4 concentrations ranging from 5 % up to 100 % in N_2 and demonstrating a low sensitivity for this gas with a LOD of 1.5 % (Figure 5.20).

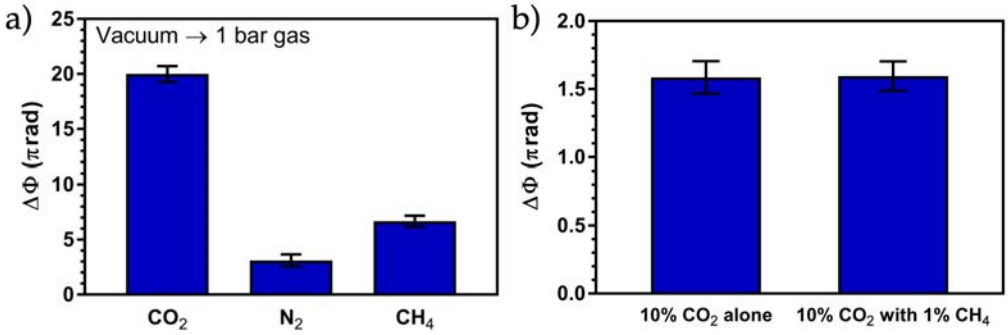

Figure 5.19. (a) Sensor response for 1 bar of N_2, CO_2 and CH_4. (b) Sensor response to 10 % CO_2 in the presence and absence of 1 % CH_4.

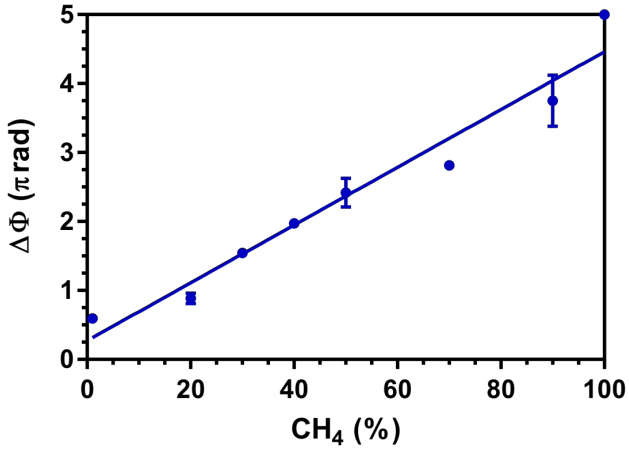

Figure 5.20. Calibration curves for CH_4 at RT.

To evaluate the reusability of the nanoZIF-8-based BiMW sensor chip we evaluated two different strategies with identical results. Both a simple N_2 purge at RT or with the vacuum pump were found to be sufficient to refresh the sensor for subsequent reuse (Figure 5.21a). Reusing the same nanoZIF-8-based BiMW sensor, the repeatability of the sensor was assessed over more than 50 measurements followed by regeneration cycles, with a relative standard deviation (RSD) of less than 2 % (Figure 5.21b). It is also important to highlight here that XRD of the sensor after finalizing all the CO_2 measurements showed that the nanoZIF-8 film retains its crystallinity (Figure 5.22).

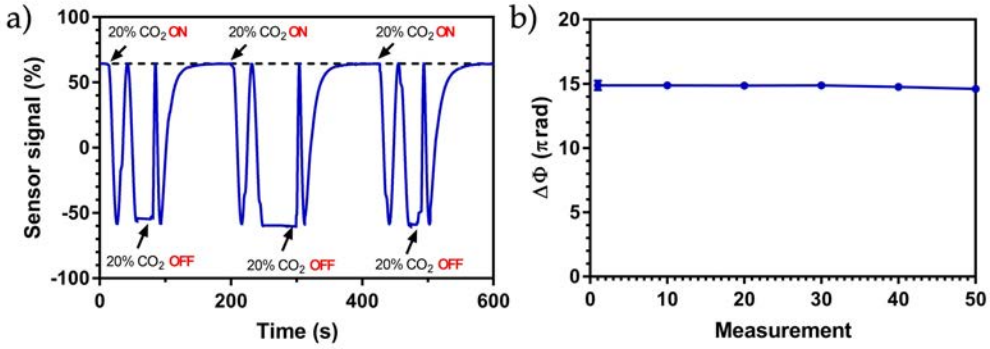

Figure 5.21. (a) Real-time detection cycles of three consecutive measurements of 20 % CO_2. (b) 50 consecutive measurements at 100 % CO_2.

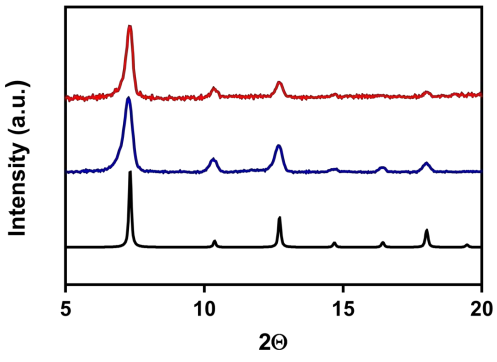

Figure 5.22. XRD patterns of the simulated ZIF-8 (black), freshly prepared nanoZIF-8-based BiMW sensor (blue) and after using it for the CO_2 detection experiments (red).

To evaluate the reproducibility of the MOF-BiMW sensors we fabricated distinct sensors using different BiMW chips and different batches of nanoZIF-8 (Figure 5.23). A high reproducibility was observed when comparing the different nanoZIF-8-based BiMW sensor with a signal reduction of less than 2 %. This low variability observed among the sensor chips and the nanoZIF-8 batches, and the high repeatability, are all vital indicators for future technology transfer endeavors with these sensors.

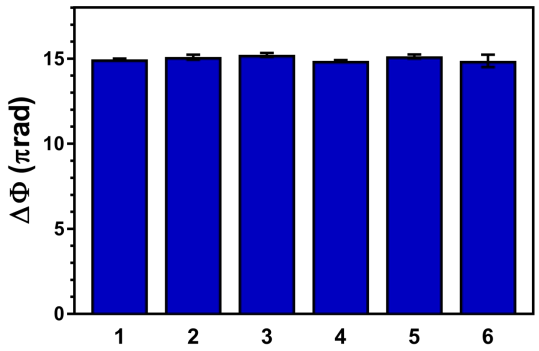

Figure 5.23. (a) Response of six different sensors (1 to 3: different chips and same nanoZIF-8 batch; 4 to 6: same chip and different nanoZIF-8 batches) to 100 % CO_2.

As it was explained earlier, one of the main disadvantages of the commercial non-dispersive IR absorption CO_2 sensors was the water interferences. Because of that, we analyzed the performance of our MOF-sensor device to selectively detect CO_2 under humid conditions. Thus, the sensor was tested at a CO_2 concentration of 50 % and relative humidity of 25 % and 50 % (Figure 5.24a) and also a CO_2 concentration of 25 % and a RH of 25 %, 50 %, 60 % and 75 % (Figure 5.24b). Remarkably, the sensor response was unaffected by the humidity. These results confirm that water does not interfere with the CO_2 detection and an additional desiccation process is not required.

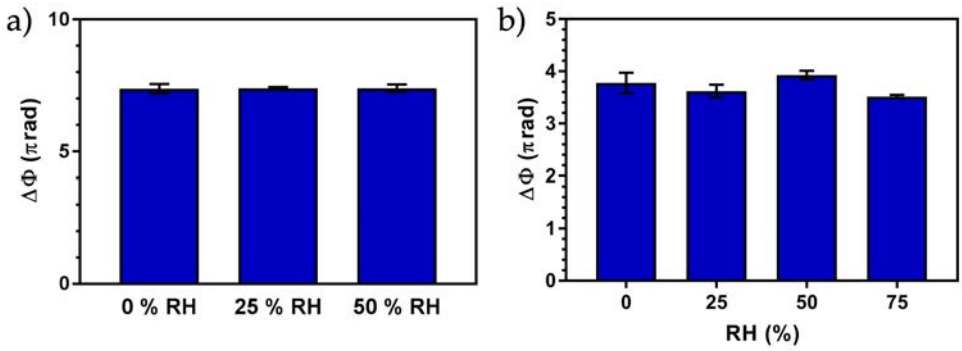

Figure 5.24. (a) Sensor response to 50 % CO_2 at RH levels of 0 %, 25 % and (b) sensor response to 25 % CO_2 at RH levels of 0 %, 25 %, 50 % and 75 %.

Another fundamental feature during sensor development is the stability of the sensor device. We tested our MOF-BiMW sensor chips by storing them under high RH levels (80 %) for 1 day, or in air for 1 month. Later, we evaluated the absolute signal ($\Delta\phi$) to a change from pure N_2 flow to pure CO_2 flow at RT. For both, the sensor stored under high RH levels and for one month, the responses were identical to those of freshly prepared ones (Figure 5.25). The high stability of the nanoZIF-8-based BiMW sensor may be due not only to the hydrolytic stability of ZIF-8 but also to the PDMS layer. The polymer film on top of the nanoZIF-8 film not only permanently attached and prevented cracking of the MOF film but also protected it from the environment.

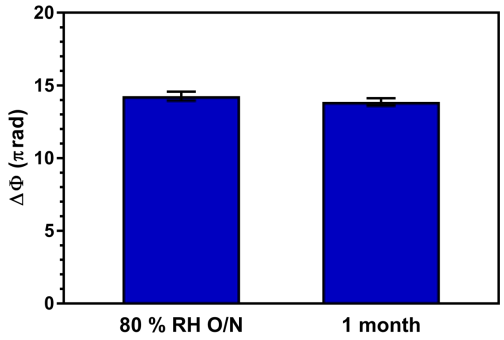

Figure 5.25. Sensor response to 100 % CO_2 after storage under RH of 80 % for 1 day or in the air for 1 month.

5.7. Conclusions

We have presented the integration, for the first time, of MOFs as receptors onto a BiMW transducer. For the development of this novel device different MOFs and integration strategies in thin films were evaluated. The optimized sensor was fabricated with the self-assembly of a transparent film of ZIF-8 nanoparticles on the surface of the BiMW waveguides. With this innovative design we applied the BiMW device for the detection of CO_2. To evaluate the proposed MOF-BiMW sensor a calibration curve was carried out with different CO_2 concentrations. The sensor showed a broad linear response, with LODs of 3130 ppm at room temperature and 774 ppm at 278 K. These values are below the threshold for CO_2 monitoring in human safety indoors and for food packaging. The film of ZIF-8 nanoparticles not only confers the ability to detect CO_2 with high sensitivity but also selectivity in a fast way. The selectivity of the sensor was confirmed in the presence of water vapor and CH_4. The unaffected sensor response by water interferences avoid any additional desiccation process. We also analytically characterized our sensor in terms of repeatability, stability and reproducibility. The MOF-BiMW sensor was efficient over 50 measurements-regeneration cycles with a RSD < 2 % and a response time of only a few seconds. Moreover, the sensor was stable after storage either for a month in air or for 1 day at 80 % RH. In addition, the sensor fabrication was highly reproducible when different chips and nanoZIF-8 batches were used. These promising properties pave the way for using MOFs to develop robust, cheap, selective and sensitive sensors for CO_2 detection. Furthermore, the BiMW technology can potentially be adapted to conform portable and fully integrated MOF-based sensors for *in-situ* gas sensing.

General conclusions

General conclusions

This PhD Thesis demonstrates the potential applicability and versatility of the BiMW interferometer sensor in environmental monitoring. This works follows two different strategies: 1) the multidisciplinary combination of surface chemistry, immunology and optical sensors in the development of an immunosensor for the detection of the pesticide Irgarol 1051 in seawater; and 2) the combination, for the first time, of the BiMW tranducer with porous crystalline materials MOFs as receptors for the development of a specific CO_2 gas sensor.

The main general conclusions related to the biosensor development are the following:

- Different functionalization strategies for silicon nitride surfaces, including APTES, CTES and a silane-PEG were evaluated to carefully control the density of (bio)receptors immobilized onto the sensor surface. The optimization of the biosensor (bio)functionalization directly affects the analytical performance and avoids the non-specific interaction of other analytes in a complex matrix such as seawater. The optimal results obtained were based on a label-free competitive inhibition immunoassay, both in terms of sensor response and sensitivity, when employing the direct covalent immobilization of Irgarol 1051 derivative *4e* onto an APTES-modified sensor surface. This is attributed to the physical proximity of the receptor to the surface were the evanescent field is maximum, enhancing the response.

- The biosensor was applied, for the first time, in the monitoring of water pollution. After a careful optimization of the methodology, the optimized immunoassay was applied to the detection of Irgarol 1051 in seawater showing a limit of detection of only 3 ng L^{-1}, clearly lower than the 16 ng L^{-1} set by the EU as the maximum allowable concentration in seawater. The LOD value is an excellent one, similar to the value detected by some

chromatographic techniques. To our knowledge, this is the most sensitive sensor for the detection of Irgarol 1051 that has been published.

- The biosensor allows the detection of the pollutant Irgarol 1051 directly in seawater. It can properly operate during 30 assay-regeneration cycles using the same sensor surface and with a time-to-result of only 20 min for each cycle. Moreover, the interferometric nanosensor is able to directly detect low concentrations of Irgarol 1051 in seawater without the need of clean-up and pre-concentration steps, which are mandatory in the chromatographic methods and without showing any background signal due to sea matrix effect.

This study was part of the European project BRAAVOO (Biosensors, Reporters and Algal Autonomous Vessels for Ocean Operation) for the development of biosensors for real time monitoring of biohazard and man-made chemical contaminants in the marine environment. As part of the project, the developed immunosensor can be further miniaturized and integrated in unmanned marine vessels or buoys for the autonomous monitoring of Irgarol 1051 in seawater. Other future improvements may include a multiplexed functionalization of each of the waveguide sensors within the same chip for the multiple evaluation of different chemical pollutants present in the same sample of seawater.

In the second application, the high sensitivity of the BiMW interferometer suggests that, besides their archetypical use for biosensing applications, BiMW sensors show potential to be adapted for sensing small molecules such as gases. The difficulty to sense these molecules using interferometric waveguide devices arises from the fact that should involve much lower RI shifts than those taking place in biological interactions. The main conclusions related to the gas sensor development are:

- The successful combination, for the first time, of MOFs as receptors with the BiMW transducer, results in a gas sensor with

improved sensitivity and selectivity. Overall, this work presents the unique combination of highly porous crystalline materials with the exceptionally high sensitivity of the BiMW interferometer. The integration of MOFs not only brings the desired selectivity but also enhanced sensitivity for gas sensing.

- The BiMW transducer is successfully applied, for the first time, for the evaluation of gas samples, in this case for air pollution monitoring. First, a gas sensor set-up was designed and evaluated. Then the sensor was constructed via self-assembly of a transparent film of ZIF-8 nanoparticles (size: 32 ± 5 nm) on the waveguides. Finally, the integration of MOFs onto the BiMW transducer surface is applied for the detection of the well-known gas CO_2. The nanoZIF-8-based sensor exhibits a broad linear response, with a limit of detection of 3130 ppm at room temperature and 774 ppm at 278 K, respectively. Furthermore, it is robust, selective, fast and reusable, and can be stored under humid conditions with no loss in performance, potentially overcoming the problems found nowadays in the sensor market.

Future perspectives may be focused towards implementing the analytical methodologies developed in this work in innovative MOF-sensor platforms for rapid and multiplexed detection and also miniaturization in integrated portable devices. On-going advances in photonic technology and the available MOFs materials are further facilitating the achievement of truly portable and multiplexed sensors with enormous potential for highly efficient and decentralized on-line monitoring in the near future.

This PhD Thesis represents a significant contribution in the integration of photonic sensors with MOFs materials opening the path of a new research line for the real implementation of advanced environmental monitoring sensing tools.

Annex

The work described in this annex was carried out during a PhD stay at the Ozcan Research Group from the Henry Samueli School of Engineering and Applied Science at the University of California, Los Angeles (UCLA). The main motivation of this stay and collaboration was the integration of MOFs as receptors on low-cost and portable optical sensor devices for water pollution control. Three different platforms were evaluated: on-chip Vis holographic imaging, on-chip UV holographic imaging and a mobile plasmonic sensor. These photonic sensing technologies are exclusive of the UCLA group and are very competitive solutions as compared to the state-of-the-art at international level.

Annex

A.1. Introduction

Water pollution is a major concern worldwide but specially in developing countries where is estimated that at least 844 million people lack access to basic drinking water and sanitation services.[225] One significant consequence of the current stage of industrialization is the exposure to heavy metals. Although heavy metals are naturally occurring elements, anthropogenic activities has introduced them in large quantities in different water bodies such as lakes or rivers.[226]

Two of the priority metals that are of public health significance are arsenic and mercury. Arsenic is highly toxic in its inorganic form and long-term exposure can lead to chronic arsenic poisoning. Typical effects include skin lesions and skin cancer. Major threats originate from contaminated groundwater in developing countries and the World Health Organization (WHO) has classified arsenic as one of WHO's 10 chemicals of major public health concern.[227] The current maximum contaminant level set by the United States Environmental Protection Agency (EPA) in drinking water is 10 ppb but in many developing countries remains 50 ppb the maximum allotment.[228]

There are three forms of mercury: elemental mercury, inorganic mercury compounds and organic mercury compounds. Health effects related to inorganic mercury compounds are mainly related to kidney damage and an acute exposure can cause burning chest pain, severe gastrointestinal symptoms and can even be fatal.[228] Mercury is also considered by WHO as one of the top 10 chemicals of major public health concern.[229] Currently, the maximum contaminant level set by EPA in drinking water is 2 ppb.[228]

The introduction of low-cost and portable sensor devices in developing countries for water pollution control is an unmet urgent need. The Ozcan Research Group at UCLA are pioneers in the development of low-cost and portable optical devices. In our previous work of the MOF-BiMW gas sensor, we have demonstrated that MOFs not only bring the desired selectivity, but also enhanced

sensitivity. Therefore, combining MOFs materials with the advanced portable optical technologies from UCLA, may overcome the current constraints in the detection of priority metals in water.

There are some reported hydro-stable MOFs with a high sorption capacity for heavy metals. Relevant examples include Zr-DMBD that has exposed free-standing thiol groups in the pores of the MOFs for an effective Hg(II) uptake (Figure A.1),[171] or UiO-66 and ZIF-8 for arsenic sorption.[230,231]

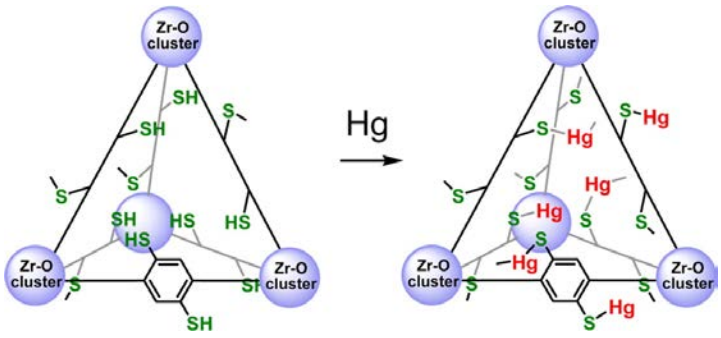

Figure A.1. Synthetic scheme of the Zr-DMBD network before and after loading mercury. The topology is shown in a simplified form as a tetrahedral cage.[171]

A.2. On-chip Vis holographic imaging

The lens-free on-chip holographic imaging refers to using a digital optoelectronic sensor array, such as a complementary metal-oxide semiconductor (CMOS) or a charge-coupled device (CCD), to sample the light directly through a specimen without any lenses in between.[232] An hologram is a photographic recording of a light field, instead of an image formed by a lens. The on-chip holographic imaging is a low-cost, portable and robust lens-free holographic microscopy. Previous proof-of-concepts in lab-on-a-chip biomedical applications of this technology include malaria parasites (*Plasmodium falciparum*) detection in smears of human red blood cells or automatically recognition of different cell types from a sample.[233,234] This new technology is a cost-effective option for microscopy tasks

without the need for imaging lenses or other bulky optical components (see Figure A.2).

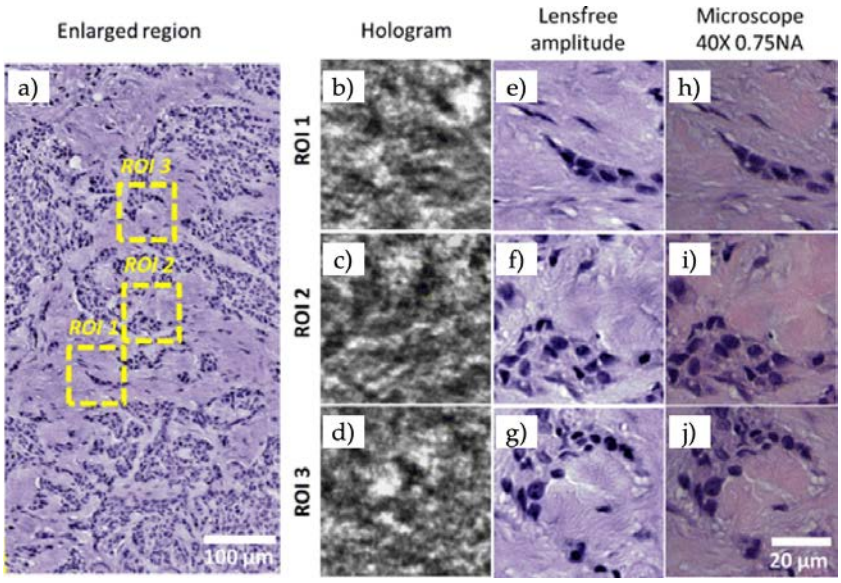

Figure A.2. (a) A digitally enlarged region of a breast tissue with carcinoma. (b-d) The zoomed-in holograms are used for the reconstruction of the lens-free images (e-g). (h-j) Microscope comparison images using ×40 objective lens.[235]

Since lenses are not incorporated in the device, the image of the sample is not recorded directly. Instead, the recorded image is a hologram that is created by the interference of the scattered light from the sample with the unperturbed light that is emitted from the light source.[235] The optical phase is required to digitally focus the sample after image acquisition. Therefore, the measured phase could potentially be used for sensing RI changes of a sample over time. For that, three different MOFs with high sorption capacity for As(V) were selected: UiO-66, MIL-88B and ZIF-8.[230,231,236] In summary, we evaluated the sensor performance for a broad range of As(V) concentrations from 0 ppm up to 1000 ppb and evaluated the MOF size effect. The MOFs sizes were critical since they were directly related to the resolution of the constructed images so larger MOFs particles were sought. Preliminary experiments did not show any general tendency when increasing the As(v) concentration. These

results may be related to many possible reasons such us the loading capacity of these MOFs under these experimental conditions or the sensitivity of the transducer itself to detect small molecules. Future experiments need to first address the bulk sensitivity of the on-chip Vis holographic imaging.

A.3. On-chip UV holographic imaging

The on-chip holographic imaging with deep UV light-emitting diodes (LEDs) (240 nm-360 nm) expanded the scope of applicability of these low-cost and portable devices. This platform is composed of a Raspberry Pi single-board computer connected to a de-capped CMOS image sensor and a UV-LED operating at 280 nm peak wavelength light source (Figure A.3). With this new platform we studied also the integration of UiO-66 and ZIF-8 for As(V) detection.

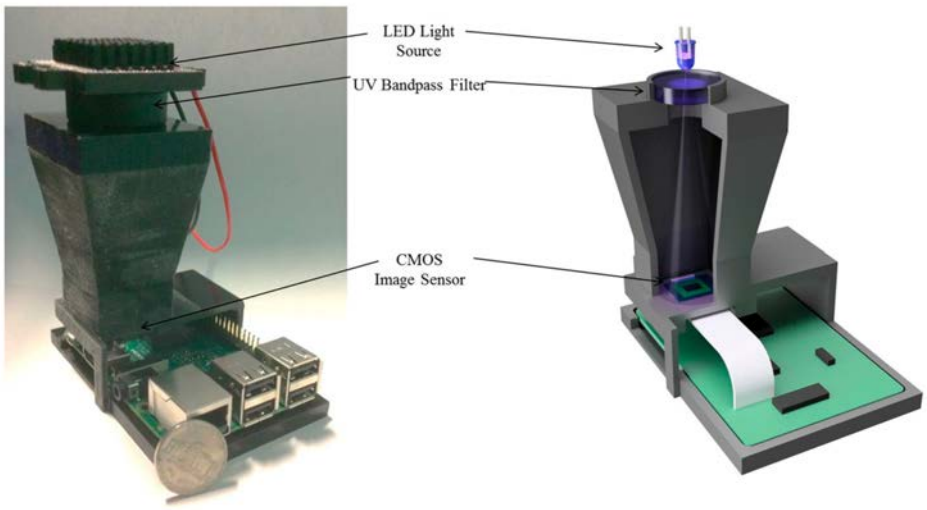

Figure A.3. Scheme and photograph of a 3D-printed prototype of an on-chip UV holographic imaging platform.[237]

The results, as before, were inconclusive so the platform was used, instead, for protein crystallography. The on-chip UV holographic imaging platform was applied for imaging protein crystals and distinguish them from salt crystals (Figure A.4). The

standard imaging technique is based in dual-mode microscopes that are sensitive, but relatively bulky and expensive. Most protein crystals absorb UV light and emit fluorescence through tryptophan residues, unlike salt crystals, making them easily distinguishable.[237] These results are published under the reference:

M. Ugur Daloglu, A. Ray, M. J. Collazo, C. Brown, D. Tseng, B. Chocarro-Ruiz, L. M. Lechuga, D. Cascio, A. Ozcan. Low-cost and portable UV holographic microscope for high-contrast protein crystal imaging. *APL Photonics* **4,** 30804 (2019).

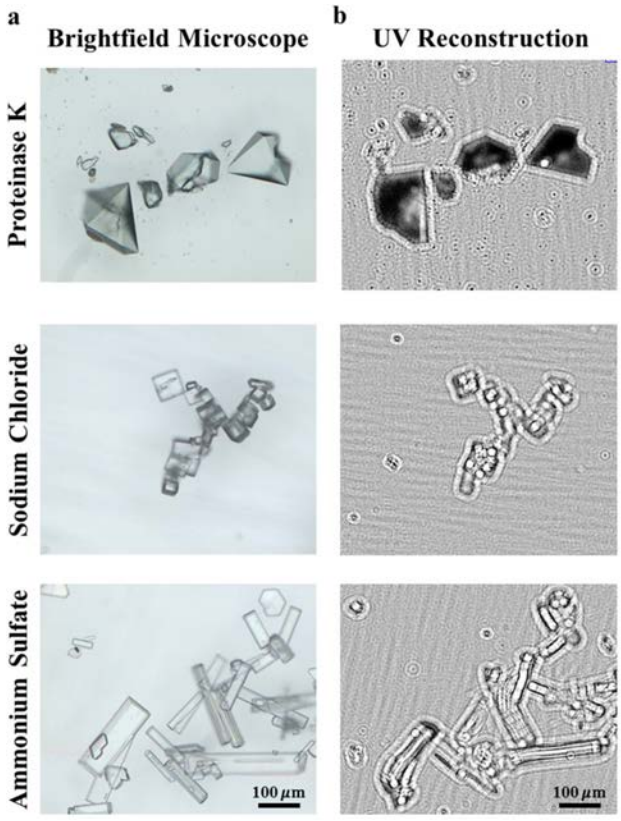

Figure A.4. (a) Brightfield microscope images of proteinase K, sodium chloride, and ammonium sulfate crystals. (b) Amplitude reconstructions of the same field-of-views in (a), proteinase K crystals appearing significantly darker.[237]

A.4. Mobile plasmonic sensor

As explained in the introduction, LSPR are EW-based sensors where the plasmon resonance occur when light interacts with subwavelength metal nanostructures. Only one previous work reports the integration of HKUST-1 as receptors in a LSPR sensor for CO_2 detection.[194] At the Prof. Ozcan Lab, they have designed a low-cost and portable plasmonic sensor for on-site monitoring (Figure A.5).[237] The plasmonic nanostructures employed are square periodicity gold nanohole arrays with a relief depth and hole diameter of 300 nm and 380 nm. We studied the integration of Zr-DMBD, UiO-66 and ZIF-8 nanoparticles (below the nanohole diameter). The experiments were performed both in static conditions and with a microfluidic delivery system. The sensor response in static conditions was too slow. The last methodology was expected to enhance the sensitivity of the sensor by flowing larger quantities of heavy metals diluted in water. The problem was that even at very low flow rates the smallest nanoparticles were flown away. Future experiments need to address the grow of MOF films onto the gold sensor surface and also evaluate larger types of water pollutants.

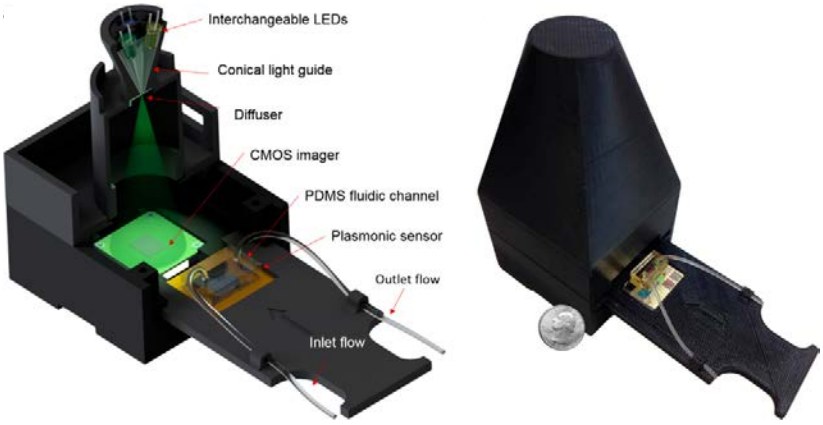

Figure A.5. Schematic illustration and photograph of a 3D-printed prototype of the mobile plasmonic sensor.[237]

List of publications

PUBLICATIONS

Interferometric nanoimmunosensor for label-free and real-time monitoring of Irgarol 1051 in seawater
B. Chocarro-Ruiz, S. Herranz, J. Sanchís, M. Farré, M.P. Marco, L.M. Lechuga
2018 *Biosensors and Bioelectronics,* 117: 47-52

A CO_2 Optical Sensor based on Self-Assembled Metal-Organic Framework Nanoparticles
B. Chocarro-Ruiz, J. Pérez-Carvajal, C. Avci, O. Calvo-Lozano, M.I. Alonso, D. Maspoch, L.M. Lechuga
2018 *Journal of Materials Chemistry A*, 6(27): 13171-13177

Low-cost and portable UV holographic microscope for high-contrast protein crystal imaging
M. Ugur Daloglu, A. Ray, M. J. Collazo, C. Brown, D. Tseng, B. Chocarro-Ruiz, L. M. Lechuga, D. Cascio, A. Ozcan
2019 *APL Photonics*, 4(3): 030804

Full integration of photonic nanoimmunosensors in portable platforms for on-line monitoring of ocean pollutants
A. Fernández Gavela, S. Herranz, B. Chocarro-Ruiz, F. Falke, E. Schreuder, H. Leeuwis, R. G. Heideman, L.M. Lechuga
2019 *Sensors and Actuators B: Chemical* (In press)

Nanophotonic label-free biosensors for environmental monitoring applications
B. Chocarro-Ruiz, A. Fernández Gavela, S. Herranz, L.M. Lechuga
2017 *Current Opinion in Biotechnology*, 45: 175-183

Nanophotonic interferometric immunosensor for label-free and real-time monitoring of chemical contaminants in marine environment
B. Chocarro-Ruiz, S. Herranz, A. Fernández Gavela, L. M. Lechuga
2017 *SPIE Proceedings, SPIE Defence and Commercial Sensing*, 10215: 1021503-1021506

CONFERENCES

Integrating Metal-Organic Frameworks in a nanophotonic sensor for environmental monitoring
B. Chocarro-Ruiz, J. Pérez, D. Maspoch, L. M. Lechuga
EUROPT(R)ODE XIV - Conference on Optical Chemical Sensors and Biosensors, Naples (Italy). March 25th-28th 2018 **Poster presentation**

Novel photonic nanosensor integrating MOFs as specific receptors for gas sensing
B. Chocarro-Ruiz, J. Pérez, C. Avci, D. Maspoch, L. M. Lechuga
2nd European Conference on Metal-Organic Frameworks and Porous Polymers (EuroMOF), Delf (Netherlands). October 29th-November 1st 2017 **Poster presentation – 1st PRIZE POSTERS AWARDS**

Novel interferometric nanosensor for CO_2 detection using nanoZIF-8 Metal-Organic Frameworks as specific receptors
B. Chocarro-Ruiz, J. Pérez, D. Maspoch, L. M. Lechuga
VIII International Congress on Analytical Nanoscience and Nanotechnology (NyNA), Barcelona (Spain). July 3rd-5th 2017 **Oral presentation**

Nanophotonic interferometric immunosensor for label-free and real-time monitoring of chemical contaminants in marine environment
B. Chocarro-Ruiz, S. Herranz, A. Fernández, M.P. Marco, J. Sanchís, M. Farre, L.M. Lechuga
SPIE Defense + Commercial Sensing, Anaheim (USA). April 9th-13th 2017 **Oral presentation**

Nanophotonic interferometric immunosensor for label-free and real-time monitoring of Irgarol 1051 in sea water
B. Chocarro, S. Herranz, A. Fernández, M.P. Marco, J. Sanchís, M. Farre, L.M. Lechuga
BRAAVOO workshop on Marine Biosensors, Villars-sur-Ollon (Switzerland). October 24th-25th 2016 **Oral presentation**

Photonic nanobiosensors for real time monitoring of chemical contaminants in marine environment
S. Herranz, B. Chocarro, J. Sanchís, M. Farré, M.P. Marco, L.M. Lechuga
SETAC Europe, Barcelona (Spain). May 3rd-7th 2015 **Poster presentation**

Abbreviations and acronyms

4e	Hapten, 4-[N-4-(cyclopropylamino)-6-(methylthio)[1,3,5]triazin-2-yl]aminobutyric acid
4e-cona	*4e*-Conalbumin conjugate
Ab	Antibody
AB	Acetate buffer
ACGIH	Association Advancing Occupational and Environmental Health
Ag	Antigen
APTES	3-Aminopropyltriethoxy silane
As87	Anti-Irgarol Antibody
BDC	Benzene-1,4-dicarboxylic acid
BET	Brunauer-Emmett-Teller
BHF	Buffer hydrofluoric acid
BiMW	Bimodal Waveguide
BKP	Back-Pressure Controller
BPY	Bypiridine
CCD	Charge-Coupled Device
CLIA	Chemiluminescence Immunoassays
CM-dextran	Carboxymethyl-dextran sodium salt
CMOS	Metal-Oxide Semiconductor
CTAB	Cetyl trimethylammonium bromide
CTES	Carboxyethylsilanetriol sodium salt
CVD	Chemical Vapor Deposition
DABCO	1,4-Diazabicyclo[2.2.2]octane
DIPEA	N,N-diisopropylethylamine
DMBD	2,5-Dimercapto-1,4-benzenedicarboxylate
DMF	Dimethylformamide
DNA	Deoxyribonucleic acid
DR	Dynamic Range
e-nose	Electronic Nose
EDC	N-(3-dimethylaminopropyl)-N□-ethylcarbodiimide hydrochloride
EDX	Energy-Dispersive X-Ray Spectroscopy
EQS	Environmental Quality Standard
EIA	Enzyme Immunoassay
ELISA	Enzyme-Linked Immunosorbent Assay

EPA	United States Environmental Protection Agency
EW	Evanescent Wave
Fab	Fragment Antigen-Binding
Fc	Fragment Crystallizable
FIA	Fluorescent Immunoassay
FID	Flame Ionization Detector
GC	Gas Chromatography
GOPTS	Glycidyloxypropyltrimethoxysilane
HKUST	Hong Kong University of Science and Technology
HPLC	High-Performance Liquid Chromatography
IC_{50}	Half Inhibitory Concentration
ICPTS	Isocyanatepropyltriethoxysilane
Ig	Immunoglobulin
IR	Infrared
IRMOF	Isoreticular Metal-Organic Frameworks
IUPAC	International Union of Pure and Applied Chemistry
LB	Langmuir-Blodgett
LbL	Layer-by-Layer
LC	Liquid Chromatography
LED	Light-Emitting Diode
LoL	Limit of Linearity
LLE	Liquid-Liquid Extraction
LOD	Limit of Detection
LPCVD	Low Pressure Chemical Vapor Deposition
LPE	Liquid-Phase Epitaxy
LSPR	Localized Surface Plasmon Resonance
Mab	Monoclonal Antibody
MeOH	Methanol
MES	2-(N-morpholino)ethanesulfonic acid
MFC	Mass Flow Controller
MIL	Material from Institute Lavoisier
MIP	Molecular Imprinted Polymer
MMM	Mixed Matrix Membrane
MOF	Metal-Organic Framework
MPTMS	(3-Mercaptopropyl)trimethoxysilane
MS	Mass Spectrometer
MS/MS	Tandem Mass Spectrometer
MW	Molecular Weight

MZI	Mach–Zehnder Interferometer
n	Refractive Index
N	Effective Refractive Index
NIOSH	National Institute for Occupational Safety and Health
OSHA	Occupational Safety and Health Administration
OWLS	Optical Waveguide Light-Mode Spectroscopy
PAb	Polyclonal Antibody
PBS	Phosphate-Buffered Saline
PDA	Photodiode Array
PDITC	*p*-Phenylene diisothiocyanate
PDMS	Polydimethylsiloxane
PECVD	Plasma Enhanced Chemical Vapor Deposition
PEG	Polyethylene glycol
PFIA	Fluorescence Polarization Immunoassay
PhC	Photonic Crystal
PM	Particulate Matter
PMMA	Poly(methyl methacrylate)
PTFE	PolyTetraFluoroEthylene
PTMSP	Poly(1-trimethylsilyl-1-propyne)
Q	Quality factor
QCM	Quartz Crystal Microbalance
RH	Relative Humidity
RI	Refractive Index
RIA	Radioimmunoassay
RIU	Refractive Index Units
RNA	Ribonucleic acid
rpm	Revolutions per minute
RR	Microcavity Resonator
RSD	Relative Standard Deviation
RT	Room Temperature
SAM	Self-Assembled Monolayer
SAW	Surface Acoustic Wave
S_{BET}	Brunauer-Emmett-Teller Surface Area
SD	Standard Deviation
SELEX	Systematic Evolution of Ligands by Exponential Enrichment
SEM	Scanning Electron Microscopy
SPE	Solid-Phase Extraction

SPME	Solid-Phase Microextraction
SPR	Surface Plasmon Resonance
sulfo-NHS	N-hydroxysulfosuccinimide sodium salt
TCD	Thermal Conductivity Detector
TE	Transverse Electric
THF	Tetrahydrofuran
TIR	Total Internal Reflection
TLC	Thin-Layer Chromatography
TM	Transverse Magnetic
UiO	Universitetet i Oslo
UV	Ultraviolet
UV-Vis	Ultraviolet-Visible
VOC	Volatile Organic Compounds
WFD	European Water Framework Directive
XRD	X-Ray Diffraction
XRPD	X-Ray Powder Diffraction
YI	Young Interferometer
ZIF	Zeolitic Imidazolate Framework

List of figures

Chapter 1. Introduction

Figure 1.1. Scheme of different routes of pollutant transportation. (source: NOAA) 2

Figure 1.2. Total anthropogenic greenhouse gas (GHG) emissions (gigaton of CO_2 - equivalent per year, $GtCO_2$ - equivalents/year) from economic sectors in 2010.[13] 3

Figure 1.3. Overview of the main health effects on humans related to pollution. (Source: Häggström, Mikael (2014)) 5

Figure 1.4. Photo of a high-performance liquid chromatography. (Source: Controltecnica Instrumentación Científica, S.L.) 8

Figure 1.5. Main formats of labeled immunoassays: (a) competitive direct detection, (b) competitive indirect detection and (c) non-competitive detection. 10

Figure 1.6. Photographs of different types of electrochemical gas sensors commercialized by Honeywell and infrared sensors commercialized by Senseair. 12

Figure 1.7. Schematic representation of a chemical sensor (left) and a biosensor (right). Chemical sensors and biosensors share the same transducer schemes but are clearly differentiable in the recognition element. 13

Figure 1.8. Scheme to illustrate the principle of the evanescent wave sensing. 18

Figure 1.9. Scheme of an asymmetric slab waveguide configuration. 19

Figure 1.10. Propagation of polarized electromagnetic radiation: (a) TE and (b) TM polarizations. 20

Figure 1.11. Photograph of the OWLS sensor device commercialized by Microvacuum Ltd. 21

Figure 1.12. (a) Scheme of the working principle of a microring resonator sensor, (b) the resonant mode shifts in response to local RI

changes induced by the binding event of the analytes with the receptors, and (c) signal obtained by monitoring the spectral shift in real time. 22

Figure 1.13. Schematic illustration of the basic steps in the color imagery analysis to monitor color changes in the PhC Bragg stacks array.[80] 25

Figure 1.14. Scheme of an interferometer based on a Mach-Zehnder configuration and its interferometric output..... 26

Figure 1.15. (a) Overview of the aMZI sensor chip layout and flow paths over the different sensors, designed by LioniX International. The three Mach-Zehnders sensors are encircled. (b) Photo of the aMZI chip assembled into a 4-channel microfluidic cell. 28

Chapter 3. Bimodal waveguide interferometer sensor

Figure 3.1. Scheme of the sensing principle of a BiMW sensor. Light is coupled in the single mode waveguide and after a modal splitter, two modes are excited, propagating until the sensor output. 38

Figure 3.2. Example of the evaluation with a BiMW interferometric sensor of a change in the bulk refractive index. The S_R corresponds to the detection of a refractive index change $\Delta n = 7{,}2 \cdot 10^{-4}$ RIU. 39

Figure 3.3. Scheme of the different steps for the fabrication of the BiMW sensors at Clean Room facilities..... 41

Figure 3.4. (a) Photograph of the BiMW chip containing 20 sensors. (b) BiMW wafer mask layout with 12 chips containing 240 sensors in total..... 42

Figure 3.5. Photograph of the experimental BiMW sensor set-up.... 44

Figure 3.6. Lapping machine with the rotating plate, the micrometric positioner with the sensor chip vertically aligned and the water flow. 45

Figure 3.7. Calibration curve of a BiMW sensor. The phase change was evaluated as a function of the refractive index variation due to the injection of HCl concentrations. Inset: output signals for different HCl

concentrations. The evaluated concentrations of HCl were: 0.025 M, 0.05 M, 0.075 M, 0.1 M and 0.25 M. 46

Chapter 4. Analysis of Irgarol 1051 in seawater with a bimodal waveguide interferometer immunosensor

Figure 4.1. General structure of the triazine herbicides. 51

Figure 4.2. Chemical structure of Irgarol 1051. 52

Figure 4.3. Irgarol 1051 inhibits the Hill reaction of the photosystem II at the thylakoid membrane (Source: Somepics).....53

Figure 4.4. Basic structure of an antibody. 56

Figure 4.5. Scheme of the basic steps involved in the production of polyclonal antibodies against low molecular weight pollutants. This example represents the production of the anti-Irgarol antibodies synthesized at the Nanobiotechnology for Diagnostics Group (Nb4D), IQAC-CSIC (Spain).....57

Figure 4.6. Main formats of immunoassays in label-free biosensors: (a) non-competitive immunoassay, (b) sandwich immunoassay and (c) competitive immunoassay. 59

Figure 4.7. Steps of a competitive immunoassay format for label-free detection. 60

Figure 4.8. Representation of a dose-response inhibition fitting curve. 61

Figure 4.9. Main procedures for surface biofunctionalization: (a) physical adsorption, (b) biochemical affinity, (c) physical entrapment, and (d) covalent immobilization. 63

Figure 4.10. Scheme of the reaction of organosilanes with the silicon surface.....65

Figure 4.11. Evaluated sensor surfaces: (I) Covalent immobilization of *4e*-cona via CTES; (II) covalent immobilization of *4e*-cona via silane-PEG-COOH; (III) covalent immobilization of *4e*-cona via APTES and the cross-linker PDITC; (IV) covalently cross-linked *4e*-cona via CM-

dextran; (V) covalently cross-linked hapten *4e* via amine-dextran; and (VI) covalent immobilization of hapten *4e* via APTES..... 69

Figure 4.12. Comparison of the different sensor surfaces responses in terms of absolute signal ($\Delta\phi$) and sensitivity (B/B_0 ratio). For sensor surface details, see Figure 4.11. The employed anti-Irgarol 1051 serum for all the sensor surfaces was 1:1000 (v/v) except for sensor surface V, which has a dilution factor of 1:1500 (v/v) and surface VI that has a dilution 1:2000 (v/v)..... 71

Figure 4.13. Comparison of different anti-Irgarol 1051 serum (As87) dilutions responses in terms of absolute signal ($\Delta\phi$)..... 77

Figure 4.14. Competitive calibration curve obtained in Irgarol 1051 standard solutions in PBS pH 7.4 and in spiked seawater. 79

Figure 4.15. (a) Real-time detection of measurement-regeneration cycles 1, 2 and 30 of antisera dilution 1:2000 (v/v) regenerated with 50 mM NaOH. (b) Comparison of day 1 and 5 responses using the same BiMW chip in terms of absolute signal ($\Delta\phi$)..... 79

Figure 4.16. Sensor signal response to the flow of seawater. 80

Figure 4.17. Sensor response for 30 consecutive measurement-regeneration cycles with seawater samples of antisera dilution 1:2000 (v/v) regenerated with 50 mM NaOH..... 81

Chapter 5. Carbon dioxide detection combining metal-organic frameworks as receptors with a bimodal waveguide interferometer sensor

Figure 5.1. Scheme of a Metal-Organic Framework (MOF). 88

Figure 5.2. DUT-60 framework: (a) Structure of DUT-60 and the metal cluster and organic ligands. (b) The mesopore system of DUT-60 illustrated by orange and blue polygons.[168] 89

Figure 5.3. Schematic representation showing the isoreticular synthesis of the IRMOFs family with different functionalization of

pore walls (top) and the enlargement of the pore size and surface area (down).[169] 90

Figure 5.4. (a–f) Schematic of the growth of the *in-situ crystallization* of MOFs on a patterned SAM surface. The patterned SAM substrate is placed in a solution containing both metal precursor and organic linker, resulting in the controlled formation of MOF crystals on the SAM pattern. (g–l) Schematic of the LbL growth of MOFs on a patterned SAM surface.[195] 93

Figure 5.5. Representation of the structure of ZIF-8. 98

Figure 5.6. (a) Representative FE-SEM image of nanoZIF-8 (size = 32 ± 5 nm) and corresponding size-distribution histogram. (b) Representative FE-SEM image of ZIF-8 (size = 53 ± 8 nm) and corresponding size-distribution histogram. (c) Representative FE-SEM image of ZIF-8 (size = 70 ± 12 nm) and corresponding size-distribution histogram. (d) Simulated (grey) and experimental XRPD patterns of ZIF-8 nanoparticles with a size of 32 ± 5 nm (blue), 53 ± 8 nm (red) and 70 ± 12 nm (black). (e) N_2 sorption isotherm at 77 K of CTAB-coated ZIF-8 nanoparticles with a size of 32 ± 5 nm (blue), 53 ± 8 nm (red) and 70 ± 12 nm (black). Respective BET surface areas: 1488, 1480 and 1471 $m^2 g^{-1}$ (theo-expected = 1300-1500 $m^2 g^{-1}$). Scale bars: 500 nm. 99

Figure 5.7. Visible transmission spectra of the films made of the self-assembly of CTAB-coated ZIF-8 particles with a size of 32 ± 5 nm (blue), 53 ± 8 nm (red) and 70 ± 12 nm (black).....100

Figure 5.8. (a) Photo of the transparent film of self-assembled ZIF-8 nanoparticles. (b) SEM image of a self-assembled nanoZIF-8 film. Scale bar: 500 nm. 101

Figure 5.9. Gas system for the controlled mixture of different gases. Photograph of the gas sensing cell with the O-ring on top of the sensor chip and the Peltier element behind. 102

Figure 5.10. (a) Schematic of the nanoZIF-8-based BiMW sensor. (b) FE-SEM image (side view) of the nanoZIF-8-based BiMW sensor, showing the layers of nanoZIF-8 and PDMS built on top of the sensor waveguide. Scale bar: 5 μm. 103

Figure 5.11. (a) Responses to 100 % CO_2 (blue) of nanoZIF-8-based BiMW sensors made of different nanoZIF-8 films, which thickness (red) has been tuned by spin-coating (spinning speed: 2000 rpm; time: 1 min; acceleration: 250 rpm s^{-1}) nanoZIF-8 colloids of different concentrations. (b) Responses to 100 % CO_2 (blue) of nanoZIF-8-based BiMW sensors made of different nanoZIF-8 films, which thickness (red) has been tuned by spin-coating a nanoZIF-8 colloid (concentration: 60 mg mL^{-1}; time: 1 min; acceleration: 250 rpm s^{-1}) at different spinning speeds from 2000 rpm to 6000 rpm..... 104

Figure 5.12. (a) Optical image of a bimodal waveguide sensor showing the cracking of the CTAB-coated nanoZIF-8 film after nanoZIF-8 is activated (left). Optical scattering image of a sensor chip when the light from a 660 nm red laser source is coupled in a bimodal waveguide, showing the complete loss of light transmission through the waveguide (right). (b) Optical image of a bimodal waveguide sensor with a first layer of activated CTAB-coated nanoZIF-8 and a second layer on top of PDMS, showing the absence of cracking once nanoZIF-8 is activated (left). Optical scattering image of a sensor chip when the light from a 660 nm laser source is coupled in a bimodal waveguide, showing the light transmission through the waveguide (right). 105

Figure 5.13. Real-time response signal to the change from pure N_2 flow to pure CO_2 flow at RT of the bare BiMW sensor..... 107

Figure 5.14. (a) FE-SEM image of a bare chip. (b) FE-SEM image of a BiMW sensor containing only the PDMS film. (c and d) FE-SEM image (left) and SEM image (right) of a BiMW coated with nanoZIF-8 embedded in PDMS. (e) EDX analysis of the nanoZIF-8 embedded in PDMS. (f) XRD pattern of the nanoZIF-8 embedded in PDMS (blue), as compared to the ZIF-8 powder pattern (black) and PDMS (red). Scale bar: 5 μm..... 108

Figure 5.15. (a) Responses to 100 % CO_2 of the nanoZIF-8-based BiMW sensor, the BiMW sensor coated with a MMM of PDMS/ZIF-8, the BiMW sensor containing only the PDMS film and the bare BiMW sensor. (b) Real-time response signal to the change from pure N_2 flow to pure CO_2 flow at RT of the nanoZIF-8-based BiMW sensor..... 109

Figure 5.16. Real-time signals for the detection of (a) 80 % CO_2, (b) 60 % CO_2, (c) 40 % CO_2 and (d) 1 % CO_2 at RT. 110

Figure 5.17. Calibration curves at 293 K (blue) and 278 K (black) for CO_2. 110

Figure 5.18. (a) Responses to 100 % CO_2 of the nanoZIF-8-based BiMW sensor at different temperatures, from RT to 278 K. (b) Adsorption isotherms of nanoZIF-8 by using CO_2 at 278 K (black), CO_2 at 293 K (blue), N_2 at 278 K (yellow), and N_2 at 293 K (red). 111

Figure 5.19. (a) Sensor response for 1 bar of N_2, CO_2 and CH_4. (b) Sensor response to 10 % CO_2 in the presence and absence of 1 % CH_4. 112

Figure 5.20. Calibration curves for CH_4 at RT. 112

Figure 5.21. (a) Real-time detection cycles of three consecutive measurements of 20 % CO_2. (b) 50 consecutive measurements at 100 % CO_2. 113

Figure 5.22. XRD patterns of the simulated ZIF-8 (black), freshly prepared nanoZIF-8-based BiMW sensor (blue) and after using it for the CO_2 detection experiments (red). 113

Figure 5.23. (a) Response of six different sensors (1 to 3: different chips and same nanoZIF-8 batch; 4 to 6: same chip and different nanoZIF-8 batches) to 100 % CO_2. 114

Figure 5.24. (a) Sensor response to 50 % CO_2 at RH levels of 0 %, 25 % and (b) sensor response to 25 % CO_2 at RH levels of 0 %, 25 %, 50 % and 75 %.. 115

Figure 5.25. Sensor response to 100 % CO_2 after storage under RH of 80 % for 1 day or in the air for 1 month. 115

Annex

Figure A.1. Synthetic scheme of the Zr-DMBD network before and after loading mercury. The topology is shown in a simplified form as a tetrahedral cage.[170] 126

Figure A.2. (a) A digitally enlarged region of a breast tissue with carcinoma. (b-d) The zoomed-in holograms are used for the reconstruction of the lens-free images (e-g). (h-j) Microscope comparison images using ×40 objective lens.[234] 127

Figure A.3. Scheme and photograph of a 3D-printed prototype of an on-chip UV holographic imaging platform.[236] 128

Figure A.4. (a) Brightfield microscope images of proteinase K, sodium chloride, and ammonium sulfate crystals. (b) Amplitude reconstructions of the same field-of-views in (a), proteinase K crystals appearing significantly darker.[236] 129

Figure A.5. Schematic illustration and photograph of a 3D-printed prototype of the mobile plasmonic sensor.[236] 130

List of tables

Chapter 1. Introduction

Table 1.1. Comparison of the limit of detection of the different EW-based sensors. 29

Chapter 3. Bimodal waveguide interferometer sensor

Table 3.1. Refractive index change induced by a set of HCl solutions and corresponding phase changes evaluated on a BiMW sensor. 46

Chapter 4. Analysis of Irgarol 1051 in seawater with a bimodal waveguide interferometer immunosensor

Table 4.1. Chromatographic techniques reported for the measurement of Irgarol 1051 in seawater.....53

Table 4.2. Summary of the optimized parameters during APTES silanization and immobilization of hapten 4e. AB: 50 mM Acetate buffer 74

Table 4.3. Optimized immunoassay conditions.....76

Table 4.4. Analyses of spiked seawater samples.....83

Chapter 5. Carbon dioxide detection combining metal-organic frameworks as receptors with a bimodal waveguide interferometer sensor

Table 5.1. PDMS film thicknesses tuned by spin-coating (time: 1 min; acceleration: 250 rpm s^{-1}) at different spinning speeds and toluene dilutions.....106

Bibliography

1. Johnson, D. L. *et al.* Meanings of environmental terms. *J. Environ. Qual.* **26**, 581–589 (1997).
2. Stern, A. C. *Air pollutants, their transformation and transport*. (Academic Press, 1976).
3. Edenhofer, O. *Climate change 2014: mitigation of climate change*. **3**, (Cambridge University Press, 2015).
4. Myhre, G. *et al.* Anthropogenic and natural radiative forcing. *Clim. Chang.* **423**, 658–740 (2013).
5. Sahara dust, sea spray and fires contribute to bad air quality — European Environment Agency. Available at: https://www.eea.europa.eu/highlights/sahara-dust-sea-spray-and/. (Accessed: 25th October 2018)
6. Spiro, T. G. & Stigliani, W. M. *Quimica medioambiental.* (Pearson Prentice Hall, 2004).
7. American Public Health Association, A. *Standard methods for the examination of water and wastewater*. (American public health association, 1989).
8. Albaladejo, C. *et al.* Wireless sensor networks for oceanographic monitoring: A systematic review. *Sensors* **10**, 6948–6968 (2010).
9. Abel, P. D. *Water pollution biology*. (CRC Press, 2014).
10. Novotny, V. *Water quality: prevention, identification and management of diffuse pollution*. (Van Nostrand-Reinhold Publishers, 1994).
11. Calvert, J. G. Glossary of atmospheric chemistry terms (Recommendations 1990). *Pure Appl. Chem.* **62**, 2167–2219 (1990).
12. Lelieveld, J., Evans, J. S., Fnais, M., Giannadaki, D. & Pozzer, A. The contribution of outdoor air pollution sources to premature mortality on a global scale. *Nature* **525**, 367–371 (2015).
13. Pachauri, R. K. *et al. Climate change 2014: synthesis report. Contribution of Working Groups I, II and III to the fifth assessment report of the Intergovernmental Panel on Climate Change*. (IPCC, 2014).
14. Krishna, I. V. M., Manickam, V., Shah, A. & Davergave, N.

Environmental management: science and engineering for industry. (Butterworth-Heinemann, 2017).

15. Stansfeld, S. A. & Matheson, M. P. Noise pollution: non-auditory effects on health. *Br. Med. Bull.* **68**, 243–257 (2003).
16. Kampa, M. & Castanas, E. Human health effects of air pollution. *Environ. Pollut.* **151**, 362–367 (2008).
17. Schwarzenbach, R. P., Egli, T., Hofstetter, T. B., von Gunten, U. & Wehrli, B. Global water pollution and human health. *Annu. Rev. Environ. Resour.* **35**, 109–136 (2010).
18. Solomon, S. Stratospheric ozone depletion: A review of concepts and history. *Rev. Geophys.* **37**, 275–316 (1999).
19. Ainsworth, E. A., Yendrek, C. R., Sitch, S., Collins, W. J. & Emberson, L. D. The effects of tropospheric ozone on net primary productivity and implications for climate change. *Annu. Rev. Plant Biol.* **63**, 637–661 (2012).
20. Rodriguez-Mozaz, S., Lopez de Alda, M. J. & Barceló, D. Advantages and limitations of on-line solid phase extraction coupled to liquid chromatography-mass spectrometry technologies versus biosensors for monitoring of emerging contaminants in water. *Journal of Chromatography A* **1152**, 97–115 (2007).
21. Long, F., Zhu, A., Gu, C. & Shi, H. Recent progress in optical biosensors for environmental applications. in *State of the Art in Biosensors-Environmental and Medical Applications* (IntechOpen, 2013).
22. Bakker, K. Water security: research challenges and opportunities. *Science* **337**, 914–915 (2012).
23. Ragazzi, M. *Air quality: monitoring, measuring, and modeling environmental hazards*. (CRC Press, 2016).
24. Matthias, A. D. Monitoring near-surface air quality. in *Environmental Monitoring and Characterization* 163–181 (Academic Press, 2004).
25. Dey, A. Semiconductor metal oxide gas sensors: A review. *Mater. Sci. Eng. B* **229**, 206–217 (2018).
26. Spinelle, L., Gerboles, M., Kok, G., Persijn, S. & Sauerwald, T. Review of portable and low-cost sensors for the ambient air monitoring of benzene and other volatile organic compounds.

Sensors **17**, 1520 (2017).

27. Snyder, E. G. *et al.* The changing paradigm of air pollution monitoring. *Environ. Sci. Technol.* **47**, 11369–11377 (2013).
28. Gardner, J. W. & Bartlett, P. N. A brief history of electronic noses. *Sensors Actuators B Chem.* **18**, 210–211 (1994).
29. Arshak, K., Moore, E., Lyons, G. M., Harris, J. & Clifford, S. A review of gas sensors employed in electronic nose applications. *Sens. Rev.* **24**, 181–198 (2004).
30. Pearce, T. C., Schiffman, S. S., Nagle, H. T. & Gardner, J. W. Handbook of machine olfaction. *Willy-VCH, Weinheim* (2003).
31. Dickinson, T. A., White, J., Kauer, J. S. & Walt, D. R. Current trends inartificial-nose'technology. *Trends Biotechnol.* **16**, 250–258 (1998).
32. Albert, K. J. *et al.* Cross-reactive chemical sensor arrays. *Chem. Rev.* **100**, 2595–2626 (2000).
33. Shurmer, H. V & Gardner, J. W. Odour discrimination with an electronic nose. *Sensors Actuators B Chem.* **8**, 1–11 (1992).
34. Nagle, H. T., Gutierrez-Osuna, R. & Schiffman, S. S. The how and why of electronic noses. *IEEE Spectr.* **35**, 22–31 (1998).
35. Schaller, E., Bosset, J. O. & Escher, F. 'Electronic noses' and their application to food. *LWT-Food Sci. Technol.* **31**, 305–316 (1998).
36. McNaught, A. D. & Wilkinson, A. *Compendium of chemical terminology: IUPAC recommendations*. (Blackwell Science, 1997).
37. Bhalla, N., Jolly, P., Formisano, N. & Estrela, P. Introduction to biosensors. *Essays in biochemistry* **60**, 1–8 (2016).
38. Wang, J. Glucose biosensors: 40 years of advances and challenges. *Electroanalysis* **13**, 983–988 (2001).
39. Ronkainen, N. J., Halsall, H. B. & Heineman, W. R. Electrochemical biosensors. *Chem. Soc. Rev.* **39**, 1747–1763 (2010).
40. Grieshaber, D., Mackenzie, R., Vörös, J. & Reimhult, E. Electrochemical biosensors-sensor principles and architectures. *Sensors* **8**, 1400–1458 (2008).
41. Kassal, P., Steinberg, M. D. & Steinberg, I. M. Wireless chemical sensors and biosensors: A review. *Sensors Actuators B Chem.* **266**, 228–245 (2018).

42. Gründler, P. *Chemical sensors: an introduction for scientists and engineers*. (Springer Berlin Heidelberg, 2007).

43. Hulanicki, A., Glab, S. & Ingman, F. Chemical sensors: definitions and classification. *Pure and Applied Chemistry* **63**, 1247–1250 (1991).

44. Wang, C., Yin, L., Zhang, L., Xiang, D. & Gao, R. Metal oxide gas sensors: sensitivity and influencing factors. *Sensors* **10**, 2088–2106 (2010).

45. Gründler, P. Mass-sensitive sensors. in *Chemical Sensors: An Introduction for Scientists and Engineers* 119–122 (Springer Berlin Heidelberg, 2007).

46. Tamayo, J., Kosaka, P. M., Ruz, J. J., San Paulo, Á. & Calleja, M. Biosensors based on nanomechanical systems. *Chem. Soc. Rev.* **42**, 1287–1311 (2013).

47. Ligler, F. S. & Taitt, C. A. R. *Optical biosensors: present and future*. (Elsevier, 2002).

48. Narayanaswamy, R. & Wolfbeis, O. S. *Optical sensors: industrial environmental and diagnostic applications*. (Springer Berlin Heidelberg, 2004).

49. Estevez, M. C., Alvarez, M. & Lechuga, L. M. Integrated optical devices for lab-on-a-chip biosensing applications. *Laser Photon. Rev.* **6**, 463–487 (2012).

50. Nguyen, H. H., Park, J., Kang, S. & Kim, M. Surface plasmon resonance: A versatile technique for biosensor applications. *Sensors* **15**, 10481–10510 (2015).

51. Homola, J. Surface plasmon resonance sensors for detection of chemical and biological species. *Chem. Rev.* **108**, 462–493 (2008).

52. Mayer, K. M. & Hafner, J. H. Localized surface plasmon resonance sensors. *Chem. Rev.* **111**, 3828–3857 (2011).

53. Estevez, M. C., Otte, M. A., Sepulveda, B. & Lechuga, L. M. Trends and challenges of refractometric nanoplasmonic biosensors: A review. *Analytica Chimica Acta* **806**, 55–73 (2014).

54. Label-free biosensors – Optical grating coupler sensor and biomolecular analyses instrumentation. Available at: http://www.owls-sensors.com/. (Accessed: 11th January 2019)

55. Székács, A., Trummer, N., Adányi, N., Váradi, M. & Szendro, I.

Development of a non-labeled immunosensor for the herbicide trifluralin via optical waveguide lightmode spectroscopic detection. *Anal. Chim. Acta* **487**, 31–42 (2003).

56. Adányi, N. *et al.* Development of immunosensor based on OWLS technique for determining aflatoxin B1 and ochratoxin A. *Biosens. Bioelectron.* **22**, 797–802 (2007).

57. Székács, A., Adányi, N., Székács, I., Majer-Baranyi, K. & Szendro, I. Optical waveguide light-mode spectroscopy immunosensors for environmental monitoring. *Appl. Opt.* **48**, B151–B158 (2009).

58. Kim, N., Park, I. S. & Kim, W. Y. Salmonella detection with a direct-binding optical grating coupler immunosensor. *Sensors Actuators, B Chem.* **121**, 606–615 (2007).

59. Cooper, I. R., Meikle, S. T., Standen, G., Hanlon, G. W. & Santin, M. The rapid and specific real-time detection of Legionella pneumophila in water samples using Optical Waveguide Lightmode Spectroscopy. *J. Microbiol. Methods* **78**, 40–44 (2009).

60. Avella-Oliver, M., Ferrando, V., Monsoriu, J. A., Puchades, R. & Maquieira, A. A label-free diffraction-based sensing displacement immunosensor to quantify low molecular weight organic compounds. *Anal. Chim. Acta* **1033**, 173–179 (2018).

61. Wade, J. H. & Bailey, R. C. Applications of optical microcavity resonators in analytical chemistry. *Annu. Rev. Anal. Chem.* **9**, 1–25 (2016).

62. Foreman, M. R., Swaim, J. D. & Vollmer, F. Whispering gallery mode sensors. *Adv. Opt. Photonics* **7**, 168–240 (2015).

63. He, L., Özdemir, S. K., Zhu, J., Kim, W. & Yang, L. Detecting single viruses and nanoparticles using whispering gallery microlasers. *Nat. Nanotechnol.* **6**, 428–432 (2011).

64. Baaske, M. D., Foreman, M. R. & Vollmer, F. Single-molecule nucleic acid interactions monitored on a label-free microcavity biosensor platform. *Nat. Nanotechnol.* **9**, 933–939 (2014).

65. Wu, F., Wu, Y., Niu, Z. & Vollmer, F. Integrating a DNA strand displacement reaction with a whispering gallery mode sensor for label-free mercury (II) ion detection. *Sensors* **16**, 1197 (2016).

66. Panich, S. *et al.* Label-free Pb(II) whispering gallery mode sensing using self-assembled glutathione-modified gold nanoparticles on an optical microcavity. *Anal. Chem.* **86**, 6299–

6306 (2014).

67. Bog, U. *et al.* Large-scale parallel surface functionalization of goblet-type whispering gallery mode microcavity arrays for biosensing applications. *Small* **10**, 3863–3868 (2014).

68. Yang, G., White, I. M. & Fan, X. An opto-fluidic ring resonator biosensor for the detection of organophosphorus pesticides. *Sensors Actuators, B Chem.* **133**, 105–112 (2008).

69. Ghali, H., Chibli, H., Nadeau, J. L., Bianucci, P. & Peter, Y. A. Real-time detection of staphylococcus aureus using whispering gallery mode optical microdisks. *Biosensors* **6**, 20 (2016).

70. McClellan, M. S., Domier, L. L. & Bailey, R. C. Label-free virus detection using silicon photonic microring resonators. *Biosens. Bioelectron.* **31**, 388–392 (2012).

71. Zhu, H., White, I. M., Suter, J. D., Zourob, M. & Fan, X. Opto-fluidic micro-ring resonator for sensitive label-free viral detection. *Analyst* **133**, 356–360 (2008).

72. The Maverick Detection System. Available at: https://www.genalyte.com/about-us/our-technology/. (Accessed: 10th April 2019)

73. Yebo, N. A., Lommens, P., Hens, Z. & Baets, R. An integrated optic ethanol vapor sensor based on a silicon-on-insulator microring resonator coated with a porous ZnO film. *Opt. Express* **18**, 11859–11866 (2010).

74. Pang, F. *et al.* Sensitivity to alcohols of a planar waveguide ring resonator fabricated by a sol–gel method. *Sensors Actuators B Chem.* **120**, 610–614 (2007).

75. Bhola, B., Nosovitskiy, P., Mahalingam, H. & Steier, W. H. Sol-gel-based integrated optical microring resonator humidity sensor. *IEEE Sens. J.* **9**, 788–790 (2009).

76. Sun, Y., Shopova, S. I., Frye-Mason, G. & Fan, X. Rapid chemical-vapor sensing using optofluidic ring resonators. *Opt. Lett.* **33**, 788–790 (2008).

77. Nair, R. V. & Vijaya, R. Photonic crystal sensors: An overview. *Prog. Quantum Electron.* **34**, 89–134 (2010).

78. Xu, H., Wu, P., Zhu, C., Elbaz, A. & Gu, Z. Z. Photonic crystal for gas sensing. *J. Mater. Chem. C* **1**, 6087–6098 (2013).

79. Tian, E. *et al.* Colorful humidity sensitive photonic crystal

hydrogel. *J. Mater. Chem.* **18**, 1116–1122 (2008).

80. Zhang, Y. *et al.* A visual and organic vapor sensitive photonic crystal sensor consisting of polymer-infiltrated SiO2 inverse opal. *Phys. Chem. Chem. Phys.* **17**, 9651–9658 (2015).

81. Bonifacio, L. D. *et al.* Towards the photonic nose: a novel platform for molecule and bacteria identification. *Adv. Mater.* **22**, 1351–1354 (2010).

82. Lifson, M. A. & Miller, B. L. Photonic crystals as robust label-free biosensors. in *Photonic Materials for Sensing, Biosensing and Display Devices* 189–207 (Springer, Cham, 2016).

83. Walker, J. P. & Asher, S. A. Acetylcholinesterase-based organophosphate nerve agent sensing photonic crystal. *Anal. Chem.* **77**, 1596–1600 (2005).

84. Kozma, P., Kehl, F., Ehrentreich-Förster, E., Stamm, C. & Bier, F. F. Integrated planar optical waveguide interferometer biosensors: A comparative review. *Biosensors and Bioelectronics* **58**, 287–307 (2014).

85. Tou, Z. Q., Koh, T. W. & Chan, C. C. Poly(vinyl alcohol) hydrogel based fiber interferometer sensor for heavy metal cations. *Sensors Actuators B Chem.* **202**, 185–193 (2014).

86. Fabricius, N., Gauglitz, G. & Ingenhoff, J. A gas sensor based on an integrated optical Mach-Zehnder interferometer. *Sensors Actuators B Chem.* **7**, 672–676 (1992).

87. Kim, Y. H. *et al.* Hydrogen sensor based on a palladium-coated long-period fiber grating pair. *J. Opt. Soc. Korea* **12**, 221–225 (2008).

88. Yao, B. *et al.* All-optical Mach–Zehnder interferometric NH3 gas sensor based on graphene/microfiber hybrid waveguide. *Sensors Actuators B Chem.* **194**, 142–148 (2014).

89. Huang, X. *et al.* An in-line Mach-Zehnder interferometer using thin-core fiber for ammonia gas sensing with high sensitivity. *Sci. Rep.* **7**, 44994 (2017).

90. Drapp, B. *et al.* Integrated optical Mach-Zehnder interferometers as simazine immunoprobes. *Sensors Actuators B Chem.* **39**, 277–282 (1997).

91. Schipper, E. F., Bergevoet, A. J. H., Kooyman, R. P. H. & Greve,

J. New detection method for atrazine pesticides with the optical waveguide Mach-Zehnder immunosensor. *Anal. Chim. Acta* **341**, 171–176 (1997).

92. Sarkar, D., Gunda, N. S. K., Jamal, I. & Mitra, S. K. Optical biosensors with an integrated Mach-Zehnder Interferometer for detection of Listeria monocytogenes. *Biomed. Microdevices* **16**, 509–520 (2014).

93. Pagkali, V. *et al.* Detection of ochratoxin A in beer samples with a label-free monolithically integrated optoelectronic biosensor. *J. Hazard. Mater.* **323**, 75–83 (2017).

94. LioniX International - global provider of customized microsystem solutions. Available at: https://www.lionix-international.com/. (Accessed: 17th January 2019)

95. Chalyan, T. *et al.* Asymmetric Mach-Zehnder interferometer based biosensors for Aflatoxin M1 detection. *Biosensors* **6**, 1 (2016).

96. Optiqua Home - Realtime early warning system for safe drinking water by smart grid quality monitoring with unique 'Lab-on-Chip' technology. Available at: http://www.optiqua.com/. (Accessed: 17th January 2019)

97. Ma, K. *et al.* Contaminant detection in treated water using Optiqua's MiniLab™ biosensing system: a case study for bisphenol A. *Int. J. Environ. Anal. Chem.* **95**, 366–378 (2015).

98. Zinoviev, K. E., González-Guerrero, A. B., Domínguez, C. & Lechuga, L. M. Integrated bimodal waveguide interferometric biosensor for label-free analysis. *J. Light. Technol.* **29**, 1926–1930 (2011).

99. Maldonado, J., González-Guerrero, A. B., Domínguez, C. & Lechuga, L. M. Label-free bimodal waveguide immunosensor for rapid diagnosis of bacterial infections in cirrhotic patients. *Biosens. Bioelectron.* **85**, 310–316 (2016).

100. Vogt, M. & Hauptmann, R. Plasma-deposited passivation layers for moisture and water protection. *Surf. Coatings Technol.* **74–75**, 676–681 (1995).

101. Smolin, E. M. & Rapoport, L. *s-Triazines and derivatives*. **26**, (John Wiley & Sons, 2009).

102. Comber, S. D. W. Abiotic persistence of atrazine and simazine in water. *Pestic. Sci.* **55**, 696–702 (1999).

103. Thomas, K. V. & Brooks, S. The environmental fate and effects of antifouling paint biocides. *Biofouling* **26**, 73–88 (2010).

104. Buma, A. G. J., Sjollema, S. B., van de Poll, W. H., Klamer, H. J. C. & Bakker, J. F. Impact of the antifouling agent Irgarol 1051 on marine phytoplankton species. *J. Sea Res.* **61**, 133–139 (2009).

105. Konstantinou, I. K. & Albanis, T. A. Worldwide occurrence and effects of antifouling paint booster biocides in the aquatic environment: A review. *Environment International* **30**, 235–248 (2004).

106. Okamura, H. *et al.* Fate and ecotoxicity of the new antifouling compound Irgarol 1051 in the aquatic environment. *Water Res.* **34**, 3523–3530 (2000).

107. Tolosa, I. *et al.* Contamination of Mediterranean (Côte d'Azur) coastal waters by organotins and Irgarol 1051 used in antifouling paints. *Mar. Pollut. Bull.* **32**, 335–341 (1996).

108. Dahl, B. & Blanck, H. Toxic effects of the antifouling agent Irgarol 1051 on periphyton communities in coastal water microcosms. *Mar. Pollut. Bull.* **32**, 342–350 (1996).

109. The European Parlament and the Council of the European Union. Directives of 12 August 2013 amending Directives 2000/60/EC and 2008/105/EC as regards priority substances in the field of water policy. *Off. J. Eur. Union* **226**, 1–17 (2013).

110. Sanchez-Ferandin, S., Leroy, F., Bouget, F. Y. & Joux, F. A new, sensitive marine microalgal recombinant biosensor using luminescence monitoring for toxicity testing of antifouling biocides. *Appl. Environ. Microbiol.* **79**, 631–638 (2013).

111. Salvador, J. P. & Marco, M. P. Amperometric biosensor for continuous monitoring Irgarol 1051 in sea water. *Electroanalysis* **28**, 1833–1838 (2016).

112. Biselli, S., Bester, K., Hühnerfuss, H. & Fent, K. Concentrations of the antifouling compound Irgarol 1051 and of organotins in water and sediments of German North and Baltic Sea marinas. *Mar. Pollut. Bull.* **40**, 233–243 (2000).

113. Gimeno, R. A., Aguilar, C., Marcé, R. M. & Borrull, F. Monitoring of antifouling agents in water samples by on-line solid-phase extraction–liquid chromatography–atmospheric pressure chemical ionization mass spectrometry. *J. Chromatogr. A* **915**, 139–147 (2001).

114. Sánchez-Rodríguez, Á., Sosa-Ferrera, Z., Santana-del Pino, Á. & Santana-Rodríguez, J. J. Probabilistic risk assessment of common booster biocides in surface waters of the harbours of Gran Canaria (Spain). *Mar. Pollut. Bull.* **62**, 985–991 (2011).

115. Vorkamp, K., Bossi, R., Bester, K., Bollmann, U. E. & Boutrup, S. New priority substances of the European Water Framework Directive: Biocides, pesticides and brominated flame retardants in the aquatic environment of Denmark. *Sci. Total Environ.* **470–471**, 459–468 (2014).

116. Van Dorst, B. *et al.* Recent advances in recognition elements of food and environmental biosensors: A review. *Biosensors and Bioelectronics* **26**, 1178–1194 (2010).

117. Hunt, H. K. & Armani, A. M. Label-free biological and chemical sensors. *Nanoscale* **2**, 1544–1559 (2010).

118. Vial, L. & Dumy, P. Artificial enzyme-based biosensors. *New J. Chem.* **33**, 939–946 (2009).

119. Choi, M. M. Progress in enzyme-based biosensors using optical transducers. *Microchimica Acta* **148**, 107–132 (2004).

120. Long, F., Zhu, A. & Shi, H. Recent advances in optical biosensors for environmental monitoring and early warning. *Sensors* **13**, 13928–13948 (2013).

121. Jayasena, S. D. Aptamers: An emerging class of molecules that rival antibodies in diagnostics. *Clin. Chem.* **45**, 1628–1650 (1999).

122. Connelly, J. T. & Baeumner, A. J. Biosensors for the detection of waterborne pathogens. *Anal. Bioanal. Chem.* **402**, 117–127 (2012).

123. Ellington, A. D. & Szostak, J. W. In vitro selection of RNA molecules that bind specific ligands. *Nature* **346**, 818–22 (1990).

124. Tuerk, C. & Gold, L. Systematic evolution of ligands by exponential enrichment: RNA ligands to bacteriophage T4 DNA polymerase. *Science* **249**, 505–510 (1990).

125. Algieri, C., Drioli, E., Guzzo, L. & Donato, L. Bio-mimetic sensors based on molecularly imprinted membranes. *Sensors* **14**, 13863–13912 (2014).

126. Uzun, L. & Turner, A. P. F. Molecularly-imprinted polymer sensors: Realising their potential. *Biosens. Bioelectron.* **76**, 131–144 (2016).

127. Saphire, E. O. *et al.* Contrasting IgG structures reveal extreme

asymmetry and flexibility. *J. Mol. Biol.* **319**, 9–18 (2002).

128. Sanvicens, N., Varela, B., Ballesteros, B. & Marco, M. P. Development of an immunoassay for terbutryn: Study of the influence of the immunization protocol. *Talanta* **89**, 310–316 (2012).

129. Ballesteros, B., Barceló, D., Sanchez-Baeza, F., Camps, F. & Marco, M. P. Influence of the hapten design on the development of a competitive ELISA for the determination of the antifouling agent Irgarol 1051 at trace levels. *Anal. Chem.* **70**, 4004–4014 (1998).

130. Rabe, M., Verdes, D. & Seeger, S. Understanding protein adsorption phenomena at solid surfaces. *Adv. Colloid Interface Sci.* **162**, 87–106 (2011).

131. Trilling, A. K., Beekwilder, J. & Zuilhof, H. Antibody orientation on biosensor surfaces: a minireview. *Analyst* **138**, 1619–1627 (2013).

132. Jung, Y., Jeong, J. Y. & Chung, B. H. Recent advances in immobilization methods of antibodies on solid supports. *Analyst* **133**, 697–701 (2008).

133. Cosnier, S. & Holzinger, M. Electrosynthesized polymers for biosensing. *Chem. Soc. Rev.* **40**, 2146–2156 (2011).

134. Samanta, D. & Sarkar, A. Immobilization of bio-macromolecules on self-assembled monolayers: methods and sensor applications. *Chem. Soc. Rev.* **40**, 2567–2592 (2011).

135. Wong, L. S., Khan, F. & Micklefield, J. Selective covalent protein immobilization: strategies and applications. *Chem. Rev.* **109**, 4025–4053 (2009).

136. Vashist, S. K., Lam, E., Hrapovic, S., Male, K. B. & Luong, J. H. T. Immobilization of antibodies and enzymes on 3-aminopropyltriethoxysilane-functionalized bioanalytical platforms for biosensors and diagnostics. *Chem. Rev.* **114**, 11083–11130 (2014).

137. Diao, J., Ren, D., Engstrom, J. R. & Lee, K. H. A surface modification strategy on silicon nitride for developing biosensors. *Anal. Biochem.* **343**, 322–328 (2005).

138. Fernandez, R. E., Bhattacharya, E. & Chadha, A. Covalent immobilization of pseudomonas cepacia lipase on semiconducting materials. *Appl. Surf. Sci.* **254**, 4512–4519 (2008).

139. González-Guerrero, A. B., Alvarez, M., Castaño, A. G., Domínguez, C. & Lechuga, L. M. A comparative study of in-flow and micro-patterning biofunctionalization protocols for nanophotonic silicon-based biosensors. *J. Colloid Interface Sci.* **393**, 402–410 (2013).

140. Schneider, B. H., Dickinson, E. L., Vach, M. D., Hoijer, J. V & Howard, L. V. Highly sensitive optical chip immunoassays in human serum. *Biosens. Bioelectron.* **15**, 13–22 (2000).

141. De Vos, K. *et al.* SOI optical microring resonator with poly (ethylene glycol) polymer brush for label-free biosensor applications. *Biosens. Bioelectron.* **24**, 2528–2533 (2009).

142. García-Rupérez, J. *et al.* Label-free antibody detection using band edge fringes in SOI planar photonic crystal waveguides in the slow-light regime. *Opt. Express* **18**, 24276–24286 (2010).

143. Escorihuela, J. *et al.* Chemical silicon surface modification and bioreceptor attachment to develop competitive integrated photonic biosensors. *Anal. Bioanal. Chem.* **404**, 2831–2840 (2012).

144. Sepúlveda, B. *et al.* Optical biosensor microsystems based on the integration of highly sensitive Mach-Zehnder interferometer devices. *J. Opt. A Pure Appl. Opt.* **8**, S561 (2006).

145. Sharma, S., Johnson, R. W. & Desai, T. A. XPS and AFM analysis of antifouling PEG interfaces for microfabricated silicon biosensors. *Biosens. Bioelectron.* **20**, 227–239 (2004).

146. Gandhiraman, R. P. *et al.* Deposition of chemically reactive and repellent sites on biosensor chips for reduced non-specific binding. *Colloids Surfaces B Biointerfaces* **79**, 270–275 (2010).

147. Huertas, C. S., Domínguez-Zotes, S. & Lechuga, L. M. Analysis of alternative splicing events for cancer diagnosis using a multiplexing nanophotonic biosensor. *Sci. Rep.* **7**, 41368 (2017).

148. Zdunek, J. *et al.* Surface-imprinted nanofilaments for europium-amplified luminescent detection of fluoroquinolone antibiotics. *Chem. - A Eur. J.* **19**, 10209–10216 (2013).

149. Hennion, M.-C. & Barcelo, D. Strengths and limitations of immunoassays for effective and efficient use for pesticide analysis in water samples: A review. *Anal. Chim. Acta* **362**, 3–34 (1998).

150. Chester, R. & Jickells, T. *Marine Geochemistry*. (John Wiley &

Sons, 2006).

151. Readman, J. W. *et al.* Coastal water contamination from a triazine herbicide used in antifouling paints. *Environ. Sci. Technol.* **27**, 1940–1942 (1993).

152. Gros, M., Petrovic, M. & Barceló, D. Development of a multi-residue analytical methodology based on liquid chromatography-tandem mass spectrometry (LC-MS/MS) for screening and trace level determination of pharmaceuticals in surface and wastewaters. *Talanta* **70**, 678–690 (2006).

153. Cincinelli, A. & Martellini, T. Indoor air quality and health. *Int. J. Environ. Res. Public Health* **14**, 1286 (2017).

154. Satish, U. *et al.* Is CO2 an indoor pollutant? direct effects of low-to-moderate CO2 concentrations on human decision-making performance. *Environ. Health Perspect.* **120**, 1671–1677 (2012).

155. Chemical Sampling Information | Carbon Dioxide | Occupational Safety and Health Administration. Available at: https://www.osha.gov/dts/chemicalsampling/data/CH_225400.html. (Accessed: 15th January 2018)

156. Piedrahita, R. *et al.* The next generation of low-cost personal air quality sensors for quantitative exposure monitoring. *Atmos. Meas. Tech* **7**, 3325–3336 (2014).

157. Lehn, J. M. Toward complex matter: supramolecular chemistry and self-organization. *Proc. Natl. Acad. Sci. U. S. A.* **99**, 4763–4768 (2002).

158. Kaskel, S. *The Chemistry of Metal-Organic Frameworks, 2 Volume Set: Synthesis, Characterization, and Applications*. **1**, (John Wiley & Sons, 2016).

159. Zhou, H. C., Long, J. R. & Yaghi, O. M. Introduction to metal–organic frameworks. *Chem. Rev.* **112**, 673–674 (2012).

160. Furukawa, H. *et al.* Ultrahigh porosity in metal-organic frameworks. *Science* **329**, 424–428 (2010).

161. Mason, J. A. *et al.* Methane storage in flexible metal–organic frameworks with intrinsic thermal management. *Nature* **527**, 357–361 (2015).

162. Gascon, J., Corma, A., Kapteijn, F. & Llabrés I Xamena, F. X. Metal organic framework catalysis: Quo vadis? *ACS Catalysis* **4**, 361–378 (2014).

163. McDonald, T. M. *et al.* Cooperative insertion of CO2 in diamine-appended metal-organic frameworks. *Nature* **519**, 303–308 (2015).

164. Drisdell, W. S. *et al.* Probing adsorption interactions in metal–organic frameworks using X-ray spectroscopy. *J. Am. Chem. Soc.* **135**, 18183–18190 (2013).

165. Kreno, L. E. *et al.* Metal-organic framework materials as chemical sensors. *Chemical Reviews* **112**, 1105–1125 (2012).

166. Yaghi, O. M. & Li, H. Hydrothermal synthesis of a metal-organic framework containing large rectangular channels. *J. Am. Chem. Soc.* **117**, 10401–10402 (1995).

167. Li, H., Eddaoudi, M., O'Keeffe, M. & Yaghi, O. M. Design and synthesis of an exceptionally stable and highly porous metal-organic framework. *Nature* **402**, 276–279 (1999).

168. Brunauer, S., Emmett, P. H. & Teller, E. Adsorption of gases in multimolecular layers. *J. Am. Chem. Soc.* **60**, 309–319 (1938).

169. Hönicke, I. M. *et al.* Balancing mechanical stability and ultrahigh porosity in crystalline framework materials. *Angew. Chemie Int. Ed.* **57**, 13780–13783 (2018).

170. Eddaoudi, M. *et al.* Systematic design of pore size and functionality in isoreticular MOFs and their application in methane storage. *Science* **295**, 469–472 (2002).

171. Yee, K. K. *et al.* Effective mercury sorption by thiol-laced metal–organic frameworks: in strong acid and the vapor phase. *J. Am. Chem. Soc.* **135**, 7795–7798 (2013).

172. Yang, Q. & Zhong, C. Understanding hydrogen adsorption in metal- organic frameworks with open metal sites: a computational study. *J. Phys. Chem. B* **110**, 655–658 (2006).

173. Chen, B., Ockwig, N. W., Millward, A. R., Contreras, D. S. & Yaghi, O. M. High H2 adsorption in a microporous metal–organic framework with open metal sites. *Angew. Chemie Int. Ed.* **44**, 4745–4749 (2005).

174. Allendorf, M. D., Bauer, C. A., Bhakta, R. K. & Houk, R. J. T. Luminescent metal–organic frameworks. *Chem. Soc. Rev.* **38**, 1330–1352 (2009).

175. Ameloot, R. *et al.* Patterned growth of metal-organic framework

coatings by electrochemical synthesis. *Chem. Mater.* **21**, 2580–2582 (2009).

176. Liu, B. *et al.* Enantiopure metal–organic framework thin films: oriented SURMOF growth and enantioselective adsorption. *Angew. Chemie Int. Ed.* **51**, 807–810 (2012).
177. Huang, C.-Y., Song, M., Gu, Z.-Y., Wang, H.-F. & Yan, X.-P. Probing the adsorption characteristic of metal–organic framework MIL-101 for volatile organic compounds by quartz crystal microbalance. *Environ. Sci. Technol.* **45**, 4490–4496 (2011).
178. Allendorf, M. D. *et al.* Stress-induced chemical detection using flexible metal-organic frameworks. *J. Am. Chem. Soc.* **130**, 14404–14405 (2008).
179. Robinson, A. L. *et al.* Ultrasensitive humidity detection using metal-organic framework-coated microsensors. *Anal. Chem.* **84**, 7043–7051 (2012).
180. Campbell, M. G. & Dincă, M. Metal–organic frameworks as active materials in electronic sensor devices. *Sensors* **17**, 1108 (2017).
181. Campbell, M. G., Sheberla, D., Liu, S. F., Swager, T. M. & Dincă, M. Cu3 (hexaiminotriphenylene) 2: an electrically conductive 2D metal–organic framework for chemiresistive sensing. *Angew. Chemie Int. Ed.* **54**, 4349–4352 (2015).
182. Campbell, M. G., Liu, S. F., Swager, T. M. & Dincă, M. Chemiresistive sensor arrays from conductive 2D metal–organic frameworks. *J. Am. Chem. Soc.* **137**, 13780–13783 (2015).
183. Yao, M.-S. *et al.* Layer-by-layer assembled conductive metal–organic framework nanofilms for room-temperature chemiresistive sensing. *Angew. Chemie Int. Ed.* **56**, 16510–16514 (2017).
184. Sun, L., Campbell, M. G. & Dincă, M. Electrically conductive porous metal–organic frameworks. *Angew. Chemie Int. Ed.* **55**, 3566–3579 (2016).
185. Lu, G. & Hupp, J. T. Metal-organic frameworks as sensors: a ZIF-8 based Fabry-Pérot device as a selective sensor for chemical vapors and gases. *J. Am. Chem. Soc.* **132**, 7832–7833 (2010).
186. Lu, G., Farha, O. K., Zhang, W., Huo, F. & Hupp, J. T.

Engineering ZIF-8 thin films for hybrid MOF-based devices. *Adv. Mater.* **24**, 3970–3974 (2012).

187. Dalstein, O. *et al.* Nanoimprinted, submicrometric, MOF-based 2D photonic structures: toward easy selective vapors sensing by a smartphone camera. *Adv. Funct. Mater.* **26**, 81–90 (2016).

188. Wu, Y. *et al.* Metal–organic frameworks with a three-dimensional ordered macroporous structure: dynamic photonic materials. *Angew. Chemie Int. Ed.* **50**, 12518–12522 (2011).

189. Avci, C. *et al.* Self-assembly of polyhedral metal–organic framework particles into three-dimensional ordered superstructures. *Nat. Chem.* **10**, 78–84 (2018).

190. Cui, C. *et al.* Self-assembled metal-organic frameworks crystals for chemical vapor sensing. *Small* **10**, 3672–3676 (2014).

191. Fenzl, C., Hirsch, T. & Wolfbeis, O. S. Photonic crystals for chemical sensing and biosensing. *Angew. Chemie Int. Ed.* **53**, 3318–3335 (2014).

192. Yassine, O. *et al.* H2S sensors: fumarate-based fcu-MOF thin film grown on a capacitive interdigitated electrode. *Angew. Chemie Int. Ed.* **55**, 15879–15883 (2016).

193. Smith, M. K., Jensen, K. E., Pivak, P. A. & Mirica, K. A. Direct self-assembly of conductive nanorods of metal–organic frameworks into chemiresistive devices on shrinkable polymer films. *Chem. Mater.* **28**, 5264–5268 (2016).

194. Kreno, L. E., Hupp, J. T. & Van Duyne, R. P. Metal□organic framework thin film for enhanced localized surface plasmon resonance gas sensing. *Anal. Chem.* **82**, 8042–8046 (2010).

195. Chong, X. *et al.* Near-infrared absorption gas sensing with metal-organic framework on optical fibers. *Sensors Actuators B Chem.* **232**, 43–51 (2016).

196. Falcaro, P. *et al.* MOF positioning technology and device fabrication. *Chem. Soc. Rev.* **43**, 5513–5560 (2014).

197. Stassen, I. *et al.* An updated roadmap for the integration of metal-organic frameworks with electronic devices and chemical sensors. *Chem. Soc. Rev.* **46**, 3185–3241 (2017).

198. Yoo, Y., Lai, Z. & Jeong, H. K. Fabrication of MOF-5 membranes

using microwave-induced rapid seeding and solvothermal secondary growth. *Microporous mesoporous Mater.* **123**, 100–106 (2009).

199. Gascon, J., Aguado, S. & Kapteijn, F. Manufacture of dense coatings of Cu3 (BTC) 2 (HKUST-1) on alfa-alumina. *Microporous Mesoporous Mater.* **113**, 132–138 (2008).

200. Hermes, S., Schröder, F., Chelmowski, R., Wöll, C. & Fischer, R. A. Selective nucleation and growth of metal-organic open framework thin films on patterned COOH/CF3-terminated self-assembled monolayers on Au (111). *J. Am. Chem. Soc.* **127**, 13744–13745 (2005).

201. Zacher, D., Baunemann, A., Hermes, S. & Fischer, R. A. Deposition of microcrystalline [Cu3(btc)2] and [Zn2(bdc)2(dabco)] at alumina and silica surfaces modified with patterned self assembled organic monolayers: evidence of surface selective and oriented growth. *J. Mater. Chem.* **17**, 2785–2792 (2007).

202. Biemmi, E., Scherb, C. & Bein, T. Oriented growth of the metal organic framework Cu3(BTC)2(H2O)3·xH2O tunable with functionalized self-assembled monolayers. *J. Am. Chem. Soc.* **129**, 8054–8055 (2007).

203. Shekhah, O. *et al.* Step-by-step route for the synthesis of metal-organic frameworks. *J. Am. Chem. Soc.* **129**, 15118–15119 (2007).

204. Arslan, H. K. *et al.* High-throughput fabrication of uniform and homogenous MOF coatings. *Adv. Funct. Mater.* **21**, 4228–4231 (2011).

205. Chernikova, V., Shekhah, O. & Eddaoudi, M. Advanced fabrication method for the preparation of MOF thin films: liquid-phase epitaxy approach meets spin coating method. *ACS Appl. Mater. Interfaces* **8**, 20459–20464 (2016).

206. Gu, Z. G. *et al.* Transparent films of metal-organic frameworks for optical applications. *Microporous Mesoporous Mater.* **211**, 82–87 (2015).

207. Hall, D. B., Underhill, P. & Torkelson, J. M. Spin coating of thin and ultrathin polymer films. *Polym. Eng. Sci.* **38**, 2039–2045 (1998).

208. Hinterholzinger, F. M. *et al.* One-dimensional metal-organic framework photonic crystals used as platforms for vapor

sorption. *J. Mater. Chem.* **22**, 10356–10362 (2012).

209. Guo, H., Zhu, Y., Qiu, S., Lercher, J. A. & Zhang, H. Coordination modulation induced synthesis of nanoscale Eu1-xTbx-metal-organic frameworks for luminescent thin films. *Adv. Mater.* **22**, 4190–4192 (2010).

210. García Márquez, A. *et al.* Green microwave synthesis of MIL-100 (Al, Cr, Fe) nanoparticles for thin-film elaboration. *Eur. J. Inorg. Chem.* **2012**, 5165–5174 (2012).

211. Demessence, A. *et al.* Elaboration and properties of hierarchically structured optical thin films of MIL-101 (Cr). *Chem. Commun.* 7149–7151 (2009).

212. Denny Jr, M. S. & Cohen, S. M. In situ modification of metal-organic frameworks in mixed-matrix membranes. *Angew. Chemie Int. Ed.* **54**, 9029–9032 (2015).

213. Campbell, J., Székely, G., Davies, R. P., Braddock, D. C. & Livingston, A. G. Fabrication of hybrid polymer/metal organic framework membranes: mixed matrix membranes versus in situ growth. *J. Mater. Chem. A* **2**, 9260–9271 (2014).

214. Makiura, R. *et al.* Surface nano-architecture of a metal-organic framework. *Nat. Mater.* **9**, 565–571 (2010).

215. Stassen, I. *et al.* Electrochemical film deposition of the zirconium metal-organic frmework UiO-66 and application in a miniaturized sorbent trap. *Chem. Mater.* **27**, 1801–1807 (2015).

216. Stassen, I. *et al.* Chemical vapour deposition of zeolitic imidazolate framework thin films. *Nat. Mater.* **15**, 304–310 (2016).

217. Cravillon, J. *et al.* Rapid room-temperature synthesis and characterization of nanocrystals of a prototypical zeolitic imidazolate framework. *Chem. Mater.* **21**, 1410–1412 (2009).

218. Fang, M. *et al.* ZIF-8/PDMS mixed matrix membranes for propane/nitrogen mixture separation: Experimental result and permeation model validation. *J. Memb. Sci.* **474**, 103–113 (2015).

219. Park, K. S. *et al.* Exceptional chemical and thermal stability of zeolitic imidazolate frameworks. *Proc. Natl. Acad. Sci. U. S. A.* **103**, 10186–10191 (2006).

220. Kaur, H., Mohanta, G. C., Gupta, V., Kukkar, D. & Tyagi, S.

Synthesis and characterization of ZIF-8 nanoparticles for controlled release of 6-mercaptopurine drug. *J. Drug Deliv. Sci. Technol.* **41**, 106–112 (2017).

221. Robb, W. L. Thin silicone membranes-their permeation properties and some applications. *Ann. N. Y. Acad. Sci.* **146**, 119–137 (1968).
222. Srinivasan, R., Auvil, S. R. & Burban, P. M. Elucidating the mechanism(s) of gas transport in poly[1-(trimethylsilyl)-1-propyne] (PTMSP) membranes. *J. Memb. Sci.* **86**, 67–86 (1994).
223. Huang, H. *et al.* Effect of temperature on gas adsorption and separation in ZIF-8: A combined experimental and molecular simulation study. *Chem. Eng. Sci.* **66**, 6297–6305 (2011).
224. CDC - METHANE - International Chemical Safety Cards - NIOSH. Available at: https://www.cdc.gov/niosh/ipcsneng/neng0291.html. (Accessed: 11th April 2018)
225. Drinking-water. Available at: https://www.who.int/news-room/fact-sheets/detail/drinking-water. (Accessed: 6th May 2019)
226. Tchounwou, P. B., Yedjou, C. G., Patlolla, A. K. & Sutton, D. J. Heavy metal toxicity and the environment. in *Molecular, clinical and environmental toxicology* 133–164 (Springer, 2012).
227. National Research Council (U.S.). Subcommittee on Arsenic in Drinking Water. *Arsenic in drinking water*. (National Academy Press, 1999).
228. US EPA, O. National Primary Drinking Water Regulations.
229. Mercury and health. Available at: https://www.who.int/news-room/fact-sheets/detail/mercury-and-health. (Accessed: 6th May 2019)
230. Wang, C., Liu, X., Chen, J. P. & Li, K. Superior removal of arsenic from water with zirconium metal-organic framework UiO-66. *Sci. Rep.* **5**, 16613 (2015).
231. Jian, M., Liu, B., Zhang, G., Liu, R. & Zhang, X. Adsorptive removal of arsenic from aqueous solution by zeolitic imidazolate framework-8 (ZIF-8) nanoparticles. *Colloids Surfaces A Physicochem. Eng. Asp.* **465**, 67–76 (2015).
232. Greenbaum, A. *et al.* Imaging without lenses: achievements and

remaining challenges of wide-field on-chip microscopy. *Nat. Methods* **9**, 889 (2012).

233. Bishara, W. *et al.* Holographic pixel super-resolution in portable lensless on-chip microscopy using a fiber-optic array. *Lab Chip* **11**, 1276–1279 (2011).

234. Wei, Q. *et al.* On-chip cytometry using plasmonic nanoparticle enhanced lensfree holography. *Sci. Rep.* **3**, 1699 (2013).

235. Zhang, Y., Greenbaum, A., Luo, W. & Ozcan, A. Wide-field pathology imaging using on-chip microscopy. *Virchows Arch.* **467**, 3–7 (2015).

236. Hou, S. *et al.* Green synthesis and evaluation of an iron-based metal-organic framework MIL-88B for efficient decontamination of arsenate from water. *Dalt. Trans.* **47**, 2222–2231 (2018).

237. Daloglu, M. U. *et al.* Low-cost and portable UV holographic microscope for high-contrast protein crystal imaging. *APL Photonics* **4**, 30804 (2019).